STRUCTURES AND DYNAMICS OF NGC 3359
OBSERVATIONAL AND THEORETICAL STUDIES
OF A BARRED SPIRAL GALAXY

By

VEERA BOONYASAIT

A DISSERTATION PRESENTED TO THE GRADUATE SCHOOL
OF THE UNIVERSITY OF FLORIDA IN PARTIAL FULFILLMENT
OF THE REQUIREMENTS FOR THE DEGREE OF
DOCTOR OF PHILOSOPHY

UNIVERSITY OF FLORIDA

2003

Copyright 2003

by

Veera Boonyasait

For God and my parents

ACKNOWLEDGMENTS

I am truly grateful for all the support, guidance, and encouragement I have received throughout this dissertation project. The list of people whom I wish to thank is much too long to be printed here. Several exceptional persons, however, require acknowledgments for helping me complete my academic goals.

The first person I wish to thank is my supervisory committee chair, Dr. Stephen Gottesman. His gentle guidance and enlightening comments always provided me further impetus to continue with the project. I am also grateful for the freedom he has given me to do my own independent research. I have also enjoyed Dr. Gottesman's weekly movie review. His in-depth knowledge of general things led us to many interesting non science-related discussions. I could not have asked for a better advisor than Dr. G.

I am also indebted to the other members of my committee. Dr. James Hunter, Jr. always provided me with useful insight on the theoretical and mathematical sections of my thesis. His vast knowledge of gasdynamics provided answers to the many questions that arose throughout the research. It has also been enjoyable to discuss the topics of football and classical music with him. I wish to also thank Dr. Henry Kandrup for his helpful comments. His elucidating galactic dynamics course solidified my interest in the field. I offer my gratitude to Dr. James Dufty who showed immediate interest in my dissertation. I am grateful that he was able to make my defense date so soon, despite the possible jet lag he may have after an extended stay in Europe. I also thank Dr. James Ipser for accepting my request to take Dr. Kandrup's position in the committee. His quick response certainly allayed my worry about filling in the vacancy left by the departure of Dr. Kandrup.

Although my Greek collaborator could not serve on my committee, I owe enormous thanks to the ever-patient Dr. Panos Patsis. Without his SPH code and its operating instructions, this dissertation would not exist. His continual assistance with the code and [illegible] have been immensely helpful. My trip to Athens was one of the highlights of my academic career.

The other collaborators to whom I am also indebted are Dr. Clayton Heller, Dr. Claude Mollenhoff and Drs. John Beckman, Ahmdena Zurita, and their IAC group. The help and the data I received from the group have been inestimable. Their support and hospitality while I was in Spain are hereby noted.

I have come to know many fantastic graduate students (past and present) and wish to thank them all, as they are friends of mine. To enumerate or list any of them would unintentionally show bias and favoritism. All I can truly say is that I am extremely grateful for their friendship, especially those who have known me for many years. Their support helped to keep me sane.

My love and thanks go out to my brother and his family, and to my sisters who have always been there for me.

Last but most importantly I wish to thank my mother, father, and step-father. They are the main inspirations from which I draw strength, love, and support. In a vain effort to offer my eternal gratitude for their love and care, I dedicate this dissertation to them. More, all that is good in me comes from you.

I am overwhelmed to be acquainted with such terrific people. Truly, the God I love shines all radiance upon me.

TABLE OF CONTENTS

page

ACKNOWLEDGMENTS iv

ABSTRACT ix

CHAPTER

1 INTRODUCTION 1

- 1.1 Observational Aspects of Barred Galaxies 2
  - 1.1.1 Bar Properties 3
  - 1.1.2 Bar Effects 7
- 1.2 Theoretical Considerations 8
  - 1.2.1 Stellar Orbits in Barred Galaxies 9
  - 1.2.2 Gas Dynamics and Simulations 10
  - 1.2.3 Previous Observations of NGC 3359 11

2 OBSERVATIONS OF ATOMIC NEUTRAL HYDROGEN 17

- 2.1 Introduction 17
- 2.2 The Data 18
- 2.3 H I Distribution and Continuum Emission 29
  - 2.3.1 Global H I Properties 29
  - 2.3.2 H I Surface Density Distribution 31
  - 2.3.3 Radial H I Profile 34
  - 2.3.4 Continuum Map 35
- 2.4 H I Kinematics 36
  - 2.4.1 Velocity Field 36
  - 2.4.2 Global Kinematical Properties 39
  - 2.4.3 Rotation Curve 43
  - 2.4.4 Velocity Dispersion Map 47
  - 2.4.5 Position Velocity Diagrams 48
- 2.5 Satellite Galaxy of NGC 3359 52
- 2.6 Summary 54

3 OBSERVATIONS OF IONIZED NEUTRAL HYDROGEN 56

- 3.1 Introduction 56
- 3.2 The Broadband Data 57
  - 3.2.1 Stellar Images 58
  - 3.2.2 H II Observations 66
- 3.3 Color Index Maps 67

3.4 Photometric Properties 73
3.4.1 Position Angle and Ellipticity of the Disk 73
3.4.2 Surface Photometry 77
3.5 Fabry-Perot Observations 78
3.5.1 Hα Data Cube 78
3.5.2 Moment Maps 81
3.5.3 Rotation Curve and Position Velocity Diagrams 84
3.5.4 Residual Map 88
3.6 The Bar Region 91
3.7 Comparison of H I and H II Kinematics 92
3.7.1 Rotation Curves 92
3.7.2 Velocity Fields 93
3.8 Summary 95
4 STELLAR DYNAMICS 98
4.1 Introduction 98
4.2 Fundamental Concepts 99
4.2.1 Derivation of the Gravitational Potential of NGC 3359 103
4.3 Periodic Orbits and their Stability 108
4.3.1 Axisymmetric Case 108
4.3.2 Non-axisymmetric Case 109
4.4 Conclusion 114
5 GASDYNAMICAL MODELS 116
5.1 Introduction 116
5.2 Overview 118
5.3 Gas Models and Morphologies 120
5.3.1 Model A 121
5.3.2 Model B 123
5.3.3 Model C 125
5.3.4 Model D 127
5.3.5 Surface Density Radial Profiles 128
5.3.6 Gas Flow Pattern 132
5.4 Kinematics 133
5.4.1 Model A 133
5.4.2 Model B 135
5.4.3 Models C and D 137
5.5 Discussion 140
5.5.1 Argument for Two Pattern Speeds 141
5.5.2 Searches for Multi-pattern Speed Systems 145
5.5.3 Comparison between the SPH and Beam Scheme Results 147
5.6 Conclusion 150
6 CONCLUSIONS 153
6.1 Summary of Previous Chapters 153
6.1.1 21 cm Data Observations 153
6.1.2 Optical and NIR observations 154

6.1.3 Stellar Orbits and SPH Simulations 155
6.2 Examination of the Central Region of NGC 3359 155
6.3 Physical Conditions of the Bar and the Surrounding Zone 156
6.3.1 Dust and Star Formation in the Bar 156
6.3.2 Kinematics of the Bar Region 158
6.4 Environment and Structures of the Spiral Arms and Disk 159
6.5 Final Words 161

7 SUGGESTIONS FOR FUTURE RESEARCH 162
7.0.1 Observations 162
7.0.2 Numerical Simulations 163

APPENDICES 163

A 21 CM ATOMIC HYDROGEN EMISSION 163

B FUNDAMENTAL CONCEPTS OF THE RADIO INTERFEROMETER 168

C FUNDAMENTAL CONCEPTS OF THE FABRY-PEROT INTERFEROMETER 180

D DERIVATION OF STABLE AND PERIODIC ORBITS 186

E SMOOTH PARTICLE HYDRODYNAMICS 190

E.1 Smoothing Length and Interpolating Kernel 192
E.2 Hydrodynamical Equations and Properties 193

REFERENCES 195

BIOGRAPHICAL SKETCH 205

Abstract of Dissertation Presented to the Graduate School
of the University of Florida in Partial Fulfillment of the
Requirements for the Degree of Doctor of Philosophy

STRUCTURES AND DYNAMICS OF NGC 3359
OBSERVATIONAL AND THEORETICAL STUDIES
OF A BARRED SPIRAL GALAXY

By

Veera Boonyasait

December 2003

Chair: Stephen T. Gottesman
Major Department: Astronomy

This research is a synthesis of observational and theoretical studies of the barred spiral galaxy NGC 3359. Analysis of the observational data was combined with numerical simulations to gain a deeper understanding of the system. The galaxy is gas-rich, with the mass of H I making up about 6% of the total dynamical mass. The distribution of the material is globally symmetric about the center. Atomic hydrogen gas can be detected out as far as 24 kpc from the center (or approximately twice the length of the photometric disk scale length). The galaxy has a grand design appearance with two spiral arms of similar pitch angles extending from the ends of the stellar bar. Along these structures reside most of the bright, giant H II regions of the galaxy. Two additional purely H I gas arms also exist outside the optical disk. The nucleus of the galaxy is strongly covered in dust and contains little CO or Hα emission. Although dust complexes are present within the bar region, they appear as dusty patches rather than the classical dust lanes. Radio continuum emission appears to be centrally concentrated and thermally induced, as it is detected predominantly around the brightest H II regions located within the bar. Analysis of the near-infrared and optical images of the galaxy have shown that as the wavelength of observation increases, the disk scale length also increases, while the bar position angle decreases.

Kinematical study of 21-cm and Hα velocity fields show that the gases are circularly rotating. However, near the bar and spiral arms of the galaxy, strong streaming motions as large as 30 km s^{-1} have been detected. Evidence also exists for out-of-plane motions near the brightest H II regions. Such types of gas flow help to explain the curious double peak feature of the H I rotation curve.

Numerical simulations of stellar orbits and gas flow within the disk of the galaxy have yielded the fascinating and rare result that the system has two pattern speeds. To reproduce the proper stellar orbits that build and support the observed bar structure, a pattern speed of 39.17 km s^{-1} kpc^{-1} is required. To match the pitch angles of the spiral arms with the SPH simulations, *slower* pattern speeds (between 10.00 and 15.52 km s^{-1} kpc^{-1}) were used. The observed density distribution and kinematical results are also best reproduced by the lower pattern speed models.

CHAPTER 1
INTRODUCTION

Bars are common in spiral galaxies. About one-third of the nearby bright spirals unquestionably are barred. Another one-third show signs of having a bar structure within the system. In the last 10 years, observations in the near infrared have shown that the old stellar population of almost all spiral galaxies forms a bar or an oval distortion close to the galactic center. In fact, our own Milky Way galaxy is also believed to barred as well (Skrutskie et al. 2001). Although the bar phenomenon is not easy to understand, bar formation is ubiquitous and important in many areas of galactic structure and evolution. The galaxy group at the University of Florida has made substantial contributions in the study of barred galaxies (Hunter & Gottesman 1996). The purpose of this thesis research was to study the dynamics and distribution of matter in the galaxy NGC 3359.

This is an observationally driven project for which the data were used to constrain the parameters of numerical stellar and gas models. Although statistical studies of the properties of barred spiral galaxies have produced interesting and important correlations among the various physical parameters, high resolution investigations of individual galaxies will reveal the evolutionary processes that shape these systems. This approach is particularly effective when data from various frequency domains are combined to cover a large fraction of the electromagnetic spectrum. Such multi wavelength observations were compiled for NGC 3359 and were interpreted using analytical calculations and numerical simulations. The galaxy was chosen primarily because of its size and brightness: its structures are well resolved and the features have high signal-to-noise ratios. In addition the system is isolated from other galaxies of comparable size. My main interest was in the internal dynamics of the system.

A brief review of recent findings of barred galaxies pertinent to the study is given here. Both observational and theoretical considerations of the subject are discussed

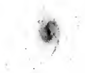

Figure 1.1 The B-band Digital Sky Survey image of NGC 3359. North is up and east is to the left in the image.

First, I discuss the prevalence of bars and some of their properties. Second, the observable phenomena attributable to the bar are addressed. Third, I give a short theoretical discussion of stellar and gas dynamics and associated numerical modeling techniques.

1.1 Observational Aspects of Barred Galaxies

A barred spiral galaxy is typically thought of as a system with a non-axisymmetric feature (i.e., the bar) in the axisymmetric component (i.e., the exponential disk) that could be surrounded by a halo. The bar is a bisymmetric and elongated feature in the central disk (Figure 1-1). It is formed mainly by stars that have periodic and elliptical orbits. At the most basic level, a bar is created by stellar and gaseous responses to the bisymmetric (bar) component of the underlying gravitational potential of the barred galaxy (Chapter 4). The size of the bar is determined by the disk scale length and/or the form of the rotation curve (Combes & Elmegreen 1993; Laine 1996; Sellwood 1981). The general features seen in most bars are the elongated light distribution from which the spiral arms extend, dust lanes that show up in optical broadband images and/or color difference maps, and oftimes isophotal twists (i.e., the major axes of the isophotes of the bar rotate) The existence of bars has been found to be more prevalent than initially thought

A recent study of the distribution of the morphological classification in the *Third reference catalogue of bright galaxies* (de Vaucouleurs et al 1991 hereafter RC3) by Knapen et al (2000) found that 50 to 60% of the disk galaxies listed in the catalogue are barred This number is increased with the addition of near infrared (NIR) observations By peering deeper into longer wavelengths at which stars radiate the effect of dust obscuration is greatly reduced (by about one order of magnitude when compared to the visual band) (Cohen et al 1981) In addition bars are easier to detect at longer wavelengths as they consist mainly of older stars Hence, NIR observations have revealed the existence of bars that were missed by earlier optical observations. There are also smaller and other bar like structures that exist in disk galaxies besides the conventional bars More nuclear bars are now being observed with advances in adaptive optics technology (Elmegreen et al 1998 Erwin & Sparke 2002) These bars can be nested in the main bars or may exist by themselves Future results from large NIR surveys such as the recently completed 2MASS project should provide a better quantitative measure of the actual bar fraction of the disk galaxy population

Barred galaxies have also been observed at cosmological distances Recently van den Bergh et al (1996) and van den Bergh et al (2000) suggested that a significant drop in bar fraction occurred beyond $z = 0.5$ However Sheth et al. (2003) found no clear evidence for such a decline beyond $z > 0.7$ Thus these systems appear to have existed earlier in the Universe than previously believed

1.1.1 Bar Properties

The shape of the bar appears to be related to the morphology of its host galaxy The isophotal contours of early type galaxies tend to twist and be rectangular (Athanassoula 1992a Ohta et al. 1990) while late-type bars have elliptical isophotes that tend not to twist (Elmegreen et al 1996a) Based on the shape of their surface brightness profiles bars can be separated into two different types (Elmegreen 1996c Elmegreen & Elmegreen 1985) The first type consists of bars that have "flat" profiles along their major axes That is their light distribution declines at a slower rate than for the surrounding disk

For the second type, the radial profile falls off exponentially like the disk (i.e., the scale lengths are the same for both features). Elmegreen (1996b) proposed that flat bars are associated with early type galaxies, while late-types tend to have exponential bars. Seigar & James (1998) found a distinction between flat and exponential bar profiles in their study of 24 galaxies in the K band. However, they found no clear correlation between bar profile and Hubble type in their small sample. Thus, the association between bar type and morphology is unclear.

A key property of the bar is its strength. Several methods have been used to quantify bar strength although two methods have been used more than others. The first method, as introduced by Martin (1995), measures the property by equating the minor (b) and major (a) axes of the bar via the equation $\epsilon_b = 10(1 - b/a)$. He found that bars of early type galaxies were stronger and longer than those of later types.

The second and more recent scheme of Buta & Block (2001, hereafter BB1) derives bar strength Q_b by determining the ratio of the tangential force to the mean axisymmetric radial force, as inferred from the gravitational potential. Six bar strength classes were established from their sample that ranged from class 0 ($Q_b < 0.05$) to class 6 (0.55 – 0.649). They determined that the minimum Q_b value that de Vaucouleurs used to classify a disk galaxy as barred (i.e., an "SB" galaxy in RC3 nomenclature) was at least 0.15 (Class 2). Using the BB1 method, Laurikainen & Salo (2002) did not observe the same trend that Martin (1995) found. Nevertheless, the BB1 process is a good and robust method for measuring bar strengths, as it does not depend on visual determinations (and concomitant bias).

Perhaps the most important property of the bar is its pattern speed Ω_p. It is typically assumed that Ω_p is rotating at the same rate as the spiral density pattern and the estimates are made at the corotation radius.[1] Unfortunately, it is also the most difficult bar property to ascertain from observations. Currently, three popular methods have been used to estimate the value of Ω_p (K[illegible] 1998). The most direct method is to correlate observable features with a specific resonance (the definition of the main resonances is given in Chapter 4), and to extrapolate the bar speed from the results. However, these methods are limited to only a few cases, and are subject to observational biases and constraints (such as projection effects, asymmetries, and limited resolutions).

---

[1] The corotation radius is the position where the pattern speed of the bar is equal to the angular speed of circular rotation.

The second method, introduced by Tremaine & Weinberg (1984), uses the continuity equation as a basis for determining Ω_p from long slit spectra information. This method was used to derive the pattern speed of eight barred galaxies (Gerssen 2002 and references therein). Unfortunately, this method requires the use of long-slit spectra that need extensive observation time. The method is not well-suited for late-type galaxies that are rich in gas. Phase changes in the gas (caused by shocks, star formation, etc.) renders the method useless.

The third and most common method to determine the pattern speed of the bar is a combination of observational and numerical techniques. Typically, a set of simulations is made with various Ω_p values. The models are then compared with the observed morphology, to obtain the closest match, and hence the best estimate of the bar speed. This approach has been used extensively here at the University of Florida by Ball (1992), England (1989, 1989), Hunter et al. (1988), and Laine et al. (1998) to compare their gas models with the observed H I data successfully.

Yet another new approach appears promising. In the early 1980s, Hunter & Ball (private communication) discovered that, when viewed in the bar frame of a model galaxy, gaseous vortex pairs are located near the stable $L_{4,5}$ Lagrangian points (Chapter 4). The gas flow follows the general morphology of the corresponding stable periodic orbits (in this case, the banana-like orbits) (Contopoulos & Grosbol 1989). Similar lowbreak vortices were found in optimal models of NGC 1300 (England 1989), NGC 1073 (England et al. 1990), NGC 3359 (Ball 1992), and NGC 3992 (Hunter et al. 1988). Recently, England et al. (2000) published an extended study of vortex pairs found in model disks, by using a wide range of bar strengths and pattern speeds in their simulations. Their models ranged from heuristic, non self consistent to fully self consistent models. All exhibited low pressure, gas vortices at $L_{4,5}$; a few models also displayed [illegible] This behavior [illegible] method of locating corotation in relatively large barred galaxies having strong H I/Hα fluxes. If the well resolved velocity field of such a galaxy would be viewed in a rigidly rotating frame, with its origin at the galactic center, as the frame angular velocity (Ω) increases a vortex pair will appear. When ($\Omega = \Omega_p$) the corotation region should become obvious and the vortex centers would be near $L_{4,5}$ (England et al. 2000). An attempt at this method was made with the available data for NGC 3359 but no prominent vortices were observed owing to the lack of a good estimate of the tangential component of the velocity field.

Lastly, it should be pointed out that the bar and spiral pattern speeds need not be synchronous. Sellwood & Sparke (1988) argued for different pattern speeds between the bar and spiral pattern. The models they produced had the same coherency between the bar and spiral arms (i.e. the former seemingly appears to start from the ends of the bar) as for single-pattern speed. This smooth transition can be explained by the non linear mode coupling between the two structures. The term was introduced by Tagger et al. (1987) who also advocated the possible existence of galaxies with multi pattern speeds. The basic concept is that the resonances of the inner (i.e. the bar) and the outer (the spiral arms) modes overlapping (e.g. corotation of the bar coincides with the inner Lindblad resonance or ILR (Chapter 5). The modal approach stems from Bertin et al. (1989a, 1989b) who used it to explain the morphological types of disk galaxies (Rautiainen 2000). Observational evidence for different pattern speeds have also been published: NGC 1398 by Moore & Gottesman (1995) and NGC 3359 by Rozas & Sempere (2000). Moore & Gottesman (1995) placed the outer Lindblad resonance of the bar at the ILR of the spiral pattern of their galaxy. Meanwhile, Rozas & Sempere (2000) assumed that a nuclear bar exists in NGC 3359 and placed its corotation radius at the ILR of the spiral pattern. Thus, the idea of two pattern speeds is not unique or new but is even more difficult to find given that no definitive method has been found to determine one single pattern speed.

1.4 Bar Effects

The existence of a bar significantly affects the properties of the galaxy. Their presence act as a catalyst to hasten secular and dynamical evolution in the disks (Shlosman 2002). There many effects attributable to the bar. Some of them will be briefly mentioned here although many more will be seen in the following chapters. The first consequence is that the bar exerts gravitation torque on the surrounding gas. Consequently, the latter will lose energy and angular momentum and flow inward from the bar ends. Shocks can occur at regions where the faster moving inflowing gas meets the slower outflowing gas. The observable features that are believe to be signposts for the shocks are the dust lanes seen in many bars (e.g., in NGC 1365, Lindblad et al. 1996). Not surprisingly, the density of interstellar medium in these regions is very high. Simulations made by Athanassoula (1992b) have shown that straight dust lanes are made by strong bars while curved lanes are caused by weaker bars.

Besides inducing inflow of gas, the bar also stirs up the gases outside of its radius as it rotates. As a result, this process creates a shallower radial abundance gradient than non-barred galaxies (Friedli et al. 1994; Roy 1996). The strength of this radial mixing is proportional to the bar type: stronger bars produce flatter gradients (Martin & Roy 1994). Similarly, the bar can also sweep out the interbar area and reduce the amount of gas within that region, as seen in NGC 3359 (Chapter 2).

The star formation process within the galaxy is also affected by the redistribution of interstellar material. The distribution of such regions vary throughout morphological types. Within the bar, star formation can form along its major axis, including the center. Generally, this occurs in late-type galaxies as early types tend to have star formation only along the arms, inner and nuclear rings, and the bar ends (Table 1 of Phillips 1996). The nuclear rings are typically created by the gas inflow that have reached the central region of the galaxy (i.e., near the ILR). The gas in these regions can also be transformed into nuclear disks and/or nested bars (Shlosman 2002) or fuel for active nuclei. Interestingly, simulations (Athanassoula 1992b; Friedli & Benz 1993) have demonstrated that continual build-up of gas in the nucleus can lead to bar destruction (e.g., 1 − 2% of the disk mass within 100 pc; Friedli & Martinet 1994).

streaming motions are induced by the bar. The manifestation of such non circular perturbations can be seen in the [illegible] barred galaxies where the isovelocity contours around the bar region are bent into an S-shape configuration. This is due to the bar being strong enough to force the particles to stream along the bar in highly elliptical orbits (Sellwood & Wilkinson 1993). The deviations from circular motions can be over 100 km s^{-1} in the plane of the galaxy (Regan et al. 1997). Another effect created by the bar is to cause the major and minor kinematical axes to become non-orthogonal.

1.2 Theoretical Considerations

The very first N body simulations of realistic disk galaxies proved to be susceptible to bar instabilities (Hockney & Hohl 1969; Miller & Prendergast 1968; Sellwood & Wilkinson 1993). The rotationally supported (cool) disks were unstable against bar formation and it became a greater problem to prevent the structures from forming rather than creating them (Sellwood 1996). One possible explanation for the bar instability comes from Toomre (1981) who suggested that the bar is formed by the amplification of leading and trailing density waves that are reflected and reversed (i.e. trailing waves become leading waves and vice versa) at the corotation resonance and the galactic center. This mechanism,called the swing amplifier, will create stationary waves upon successive reflections of the density waves (Combes 1995). An immediate consequence of this theory is that bars cannot be longer than the corotation radius. At the same time, when ILRs exist and are large enough (e.g. the nuclear ring grows through the accumulation of inflowing gas, the feedback process can be significantly decreased and possibly lead to bar destruction.

An alternative approach to bar formation[2] is the alignment of elongated orbits near the central region of the galaxy that contains two ILRs (Lynden Bell 1979). Unfortunately, the bar created by this method is small and cannot explain the typical large scale bars that are seen and appear to end near corotation. Interestingly, the paper published by Contopoulos & Papayannopoulos (1980) who have dealt with stellar orbits in bar potentials and led the way to a more elementary and physically meaningful approach.

---

[2] Another method of bar formation that is unrelated to the discussion at hand is through tidal interaction (Athanassoula & Bosma 2003; Gérin et al. 1990; Noguchi 1987

1.2.1 Stellar Orbits in Barred Galaxies

This subsection is an introduction to the theory of stellar orbits and how the bar is formed by the nature of the orbits in the plane of the disk. A fuller description of stellar orbits can be found in Chapter 4 and a complete discussion of the theory is given by Contopoulos (2002).

The orbital structures of stellar orbits in barred galaxies have been studied in detail for approximately the past three decades, highlighted by the works of Contopoulos (1980), the review of Contopoulos & Grosbøl (1989), Contopoulos & Metzamakis (1977) and Contopoulos & Papayannopoulos (1980). The orbits are typically derived through numerical integration. Under the influence of the bar perturbation, orbits that are circular in an axisymmetric potential will become elongated. The orbits are stable and periodic and make up the central family called x_1. These orbits are oriented along the bar between the corotation resonance and either the ILR or OILR if one or two such resonances exist. Similarly there are also x_2 family of orbits that are perpendicular to the bar when an ILR exists.[3] There are also other orbits within the bar that also support the structure. These orbits can be associated with higher order resonances, asymmetric, or multiperiodic. Outside corotation there are no families that provide bar support as most are aligned perpendicularly to the bar. Hence the immediate conclusion is that bars are formed by stable orbits and that they cannot be longer than the corotation radii, in agreement with Toomre (1981). Although the maximum limit to how far a bar extend appears to be well-established, the minimum limit is less clear. Through numerical simulations and observations, Combes & Elmegreen (1993, Figures 14 and 15) and Elmegreen & Elmegreen (1985) have reported that bars can end near the ILR or much the 4:1 resonance respectively.

---

[3] For the case of two ILRs, x_2 is perpendicular to the bar between the two resonances.

Gas Dynamics and Simulations

Despite its small contribution to the total mass of a barred galaxy, gas is still of special interest to the overall dynamical study of the system. The ability to stay relative cool through heat dissipation makes gas an ideal tracer of the underlying gravitational potential. Gas will generally follow the orbital paths of stars near them. However, the streamlines of gas do not cross like stellar orbits (collisions between gas clouds will produce shocks) and so the orbital structures of the two are not exactly the same. The paths taken by gas are typically elliptical near the bar region much like the local stellar paths. However, their orbits will gradually shift by 90° near the major resonances (e.g., the Lindblad resonances and corotation resonance) while stellar orbits become perpendicular to one another at the same location (Sanders & Huntley 1976; Sanders & Tubbs 1980; van Albada & Roberts 1981). The progressive change leads to orbit crowding and has been used to explain the gaseous spiral features seen in simulations. Inside the bar, the shift in orientation of gas flow near the ILR resonances can produce shocks and dust lanes as well as leading or trailing gaseous bar or spiral (Laine 1996).

One of the most effective way to study such phenomena is to develop hydrodynamical models of the gas flow. These simulations have been in prevalent use for about the past three decades, starting with the earlier works of the authors quoted in the previous paragraph. The galaxy group here at the University of Florida has maintained a focused research on such a modeling program as well. The works of Ball (1992), England (1988, 1990), and Hunter et al. (1988) have used the "beam scheme" code (Sanders & Prendergast 1974) to model the flow of gas. The simulations were able to duplicate the bar regions of their galaxies successfully. But to produce the observed spiral arms, an additional oval component was required to be added into the potentials. The recent doctoral work of Seppo Laine (1996) on NGC 7479 incorporated the use of multi-wavelength observational data with the Smoothed Particle Hydrodynamic (SPH) numerical method. The code, written by Dr. Clayton Heller, was used for comparison with the observations. In addition, the potential that the simulations used is derived from actual data and is not model-dependent. The successful results of Laine's research [illegible] same method to study the dynamical processes in NGC 3359

To understand the dynamics of NGC 3359 the SPH code will be used to calculate the gas response to the potential of the galaxy [4] The potential will be estimated from the I band photometry image under the assumption of constant mass-to-light ratio The underlying orbital structure which specifies the gas flow will be studied in parallel as it has been done for NGC 4314 in Patsis et al (1997)

Features produced by the models have to be in agreement with corresponding features identified in the optical images of NGC 3359 The gas flow of the models should match two main types of morphological features the dust lanes observed along the bar and the morphology of the spiral arms in the outer disk of the galaxy Studying the gas dynamics in parallel with the orbital dynamics of the bar will allow for a clearer understanding how the stellar and the gaseous components interact with one another

1 2 3 Previous Observations of NGC 3359

The object of research in this dissertation is the barred spiral galaxy numbered 3359 in the *New General Catalogue* It has been classified as type SB(rs)c in RC3 and SBc(s) 1 8 in *A Revised Shapley Ames Catalog of Bright Galaxies* by Sandage & Tammann (1987) and SBc in the Hubble (1926) classification scheme The latest classification given to the galaxy was made by Elmegreen & Elmegreen (1982 1995) who labeled the galaxy as type 5 based on its multi-arm appearance that arises from the the northern arms spurs The first published report of NGC 3359 (that can be found) was made by Hubble (1949) who suggested that the system was an outlyer of the Ursa Major galaxy cluster He estimated the distance to the galaxy to be $\sim$ 1.5 Mpc ("five million light years") More recent distance determinations have yielded the values between 11 Mpc (Ball 1986 de Vaucouleurs 1979) and 22.63 Mpc (Mollenhoff & Heidt 2001) As this dissertation will make multiple comparisons with the previous works of Dr Ball the value of 11 Mpc has

---

[4] The version of the SPH code that is used to construct the models in Chapter 5 comes from Dr Panos Patsis The potential that is used to run the code is derived in Chapter 4

[illegible] This value is rather low Given that the recessional velocity of the galaxy is close to [illegible] km s^{-1} the quoted distance would give $H_0 \simeq 92$ km s^{-1} Mpc^{-1} Nonetheless the value will be used throughout this research project for the sake of consistency

In the B-band the galaxy has a total (photometric) magnitude of 11 03 ± 05 and a dimension of 7 2 × 4 4 square arcminutes at the 25th magnitude per square arcsecond isophotal contour The IR observations of IRAS have found the flux density of the galaxy at 12 25 60 and 100 μm to be 0 44 ± 0 027 0 59 ± 0 024, 6 27 ± 0 03 and 16 79 ± 0 138 Jy respectively (Soifer et al 1989) the absolute far-infrared (FIR) luminosity is log(L_{FIR}) = 9 90 $L_\odot$ (Condon et al 1990) Carbon monoxide intensity is related to FIR flux (e g in star formation regions) and the first measurements of NGC 3359 produced values that were moderately low Both Stark et al (1987) and Braine et al (1992) reported CO (1 0) integrated intensity values of 0 3 – 0 48 K km s^{-1} Although the former reported the galaxy as detectable at 2 6 mm the latter listed their observation as inconclusive The most recent CO observations made by Young et al (1995) fall into the same range of values Hodge (1969) counted a total number of 46 H II regions within NGC 3359 in the initial Hα observation of the system Rozas et al (2000a) made more sensitive observations and catalogued a total of 547 ionized hydrogen regions They also gave the total Hα flux of the system to be $L_{H\alpha} = (8\ 8 \pm 0\ 6) \times 10^{40}$ ergs s^{-1}

The first radio observation was made by Heeschen & Wade (1964) at 750 and 1400 MHz using the original, single-dish 300-foot Transit Telescope at the National Radio Astronomy Observatory Rogstad et al (1967) used the Owens Valley Observatory s two-element interferometer to determine the first set of H I properties of NGC 3359 They estimated the mass of the galaxy to be 7 7 × 10^{10} M$_\odot$ but cautioned that the value was susceptible to their inaccurate distance to the galaxy determination However most of their values are in good agreement with those found by Ball (1986) and here Bosma (1981a) published the first H I velocity field However the bulwark of H I study of NGC 3359 were made by Ball (1986) and Gottesman (1982) The first kinematical analysis of the galaxy was performed by Dr Gottesman The investigation was continued by Dr Ball who also studied the the gas dynamics of the system with the use of the beam scheme (Ball 1992). In the article it was established that the best model that reproduced the gas densities and kinematics was a combination of an inhomogeneous triaxial ellipsoid (inferred from an I band image) and an oval distortion. The other results and findings of his work will be discussed in Chapters 2 and 5.

The properties of the bar have been covered extensively in recent years. Elmegreen & Elmegreen (1985) initially found it to have an exponential profile but later classified it as flat (Elmegreen et al. 1996a, 1996c). Both interpretations may be correct because the first analysis used shorter B and I wavelength observations while the latter used the NIR J, H, and K bands. The methods of determining the bar strength noted earlier have also been used on NGC 3359. In the same article in that he introduced his method, Martin (1995) found $\epsilon_b = 7$ (where a value of 8 is considered very strong) while Aguerri (1999) reported $\epsilon_b = 5$ (as inferred from the published value of $b/a = 0.48$). Laurikainen & Salo (2002) employed the Buta & Block (2001) method to derive $Q_b = 0.46$, 0.42, and 0.45 using the 2MASS H, J, and K infrared images. In a separate NIR study using data from the Calar Alto observatory, Möllenhoff & Heidt (2001) found the bar to be "fairly weak" and give the axial ratio of the bar as 0.29 and 0.28 for the J and K band respectively. Hence, the strength of the bar remains unclear. Lastly, there are only two published estimated values of the pattern speed for the galaxy. Aguerri et al. (1998) published the value of 50.04 km s^{-1} kpc^{-1} while Sempere (1995) preferred two speeds in the simulation of NGC 3359. The values that best fit her models were 100 km s^{-1} kpc^{-1} for the nuclear region and 27 km s^{-1} kpc^{-1} for the outer bar and spiral pattern.

One last important finding that will be mentioned in this chapter is the study of the oxygen distribution in the bar and disk of the galaxy by Martin & Roy (1995). Within the bar region, they found a large gradient of the O/H distribution while the slope is flat in the (outer) spiral arm region. This show that the bar was an important contributor to the chemical evolution of the galaxy, and the authors also suggested that the bar of NGC 3359 is still forming (i.e., they estimated the age to be $\sim 4 \times 10^8$ years old). This result could be very significant since it is normally assumed that observed bars are well developed. If the conjecture of Martin & Roy (1995) is true, then the dynamics of the stars and gases found in this research may help bridge the early to middle (or older) stages of development in barred galaxies.

Other important observable properties of the galaxy that have been published are summarized in Table 1.1. For a more comprehensive listing of spectroscopic measurements, please refer to Ho et al. (1997). The specifics of the important works of Ball (1986, 1992) and the Spanish group at the Instituto de Astrofísica in Spain (Rozas et al. 2000a, Rozas et al. 2000b) will be deferred to later chapters for purposes of reference, comparison, and contrast.

NGC 3359 is a good candidate galaxy for a multi wavelength research as the galaxy is nearby and therefore relatively large. It is also not only bright photometrically but also in H I. Its disk is oriented such that it is ideal for studying both the tangential and radial components of its velocity field. The galaxy has numerous star formation regions that produce strong Hα emission that are observable with a Fabry-Perot interferometer, thereby producing another set of data from which kinematical information of the system can be extracted.

Much of the past work on the dynamics and H I observations of NGC 3359 have been performed by Ball (1986, 1992). However, the data that is present for this dissertation project are more sensitive and the Hα observations were unavailable for Dr. Ball's research. The method in which the hydrodynamical models are made is also different. Most notably, the potential used for the numerical simulations is directly obtained from observations and is not an artificial construct.

In Chapter 2, the 21-cm data will be presented and analyzed. The gas distribution and kinematics will be investigated. Similar results to that of Ball (1986) are expected. The optical and NIR observations of the system are then reviewed in Chapter 3. Specifically, the color indices, bar position angle, and disk scales of the stellar and gaseous data will be determined. In addition, the kinematics of the ionized hydrogen gas will also be analyzed and compared with the results of the H I study. In Chapters 4 and 5, numerical methods are used to calculate the stellar and gaseous orbital structures and responses to the underlying gravitational potential (that has been extracted from the I-band image). In Chapter 6, the synthesis and summary of the previous chapters are presented. Also included in the final chapter are discussions of the possible future works that could be extended from this project

Table 1-1 General observational properties of NGC 3359

Property	Value
Object names[a,b]	NGC 3359 UGC 05873
Morphological type[c,d]	SB(rs)c SBc(s) I.8
Equatorial coordinates[e]	
Right Ascension (B1950)	$10^h43^m20^s.1$
Declination (B1950)	$63°29'15''.8$
Right Ascension (J2000)	$10^h46^m36^s.7$
Declination (J2000)	$63°13'27''.0$
Heliocentric radial velocity[c]	1013 ± 3 km s^{-1}
Distance[c]	11.0 Mpc
Linear scale	53.33 pc arcsec^{-1}
Distance[c]	11.0 Mpc
Photometric data	
U_T[c]	10.83 ± 0.06
B_T[c]	11.03 ± 0.05
V_T[c]	10.57 ± 0.06
J_{tot}[f]	9.439 ± 0.027
H_{tot}[f]	8.734 ± 0.035
K_{tot}[f]	8.521 ± 0.046
IRAS 12 μm flux[g]	0.43 ± 0.03 Jy
IRAS 25 μm flux[g]	0.56 ± 0.02 Jy
IRAS 60 μm flux[g]	6.27 ± 0.03 Jy
IRAS 100 μm flux[g]	16.79 ± 0.14 Jy
L_{FIR}[h]	$7.9 \times 10^9 L_\odot$
$L_{H\alpha}$[i]	8.8×10^{40} ergs s^{-1}
Diameter[c] at $\mu_B = 25$ mag arcsec^{-2}	$7'.2 \times 4'.4$
Bar attributes	
Type[j]	Flat
Projected radius[k]	43″
Projected position angle[l]	25°
Radio properties	
H I flux[m]	171.84 ± 28.20
H I linewidth at 20% level[m]	263 km s^{-1}
H I mass[c]	5×10^9 M$_\odot$
Total mass[n]	1.2×10^{11} M$_\odot$
CO flux[o]	$(0.315 \pm 0.059) \times 10^3$Jy km s^{-1}
H_2 mass[p]	2.5×10^7 M$_\odot$
Position angle[c]	170°
Inclination angle[l]	51°

[a] Dreyer (1888) [b] Nilson (1973, [c] RC3 [d] Sandage & Tammann, [e] Falco et al. (1999) [f] Jarret et al. (2003) [g] Soifer et al. (1989) [h] Condon et al. (1990) [i] Rozas et al. (2000a) [j] Elmegreen et al. (1996) [k] Aguerri et al. (1998) [l] Elmegreen & Elmegreen (1985) [m] the average value of the reported fluxes from Huchtmeier & Richter (1989), [n] Ball (1986) [o] Stark et al. (1987) [p] Braine & Combes (1992)

CHAPTER 2
OBSERVATIONS OF ATOMIC NEUTRAL HYDROGEN

2.1 Introduction

Most of the hydrogen that exists in the Universe is in stars (roughly 74% by mass; Elmegreen 1998). Hydrogen not in stars exists in various phases of the gas, from the neutral to ionised atomic hydrogen to the extremely cold ($\approx 10K$) H_2 molecules of giant molecular clouds. The amount of gas in galaxies appear to follow the Hubble diagram sequence: ellipticals contain mostly stars with little or no gas at all, (barred) spiral galaxies are known to have up to 10% of its total mass while irregulars have the most copious amount of gas (more than its stellar content).

The distribution of various species of hydrogen vary throughout a barred spiral galaxy. Molecular H_2 clouds, traced out by CO_2 observations, typically reside in the central part of the galaxy while the ionized hydrogen associated with star formation is usually seen along shocked regions such as the spiral arms and the bar though this is not always the case (e.g., the arms of M51 contain about 50% of its H_2 content). Atomic hydrogen (H I) is often distributed throughout the entire visible disk and beyond, sometimes forming rings or pseudo-rings around the central regions of barred spirals, as is the case for NGC 3359. Along with being the source of future stars, the gas is also critical in cooling the heating made by stars through its dissipative nature. The removal of heat allows the stability of the disk through rotational support to be maintained. In addition, the cool gas is an ideal tracer of the underlying galactic potential because of its low velocity dispersion.

Studies of hydrogen gas in barred galaxies have contributed greatly to our understanding of galactic dynamics. For atomic hydrogen, its 21 cm emission line is the product of the (forbidden) transition between two hyperfine levels of the hydrogen atom in the ground state (Appendix A). The first detection of H I was made on March 25, 1951 by Ewen and Purcell with the horn antenna. Early, initial observations of the gas were limited to large angular scale structures owing to the large beam solid angle (i.e. low resolution) of the single dish antennas. But with the advent of large radio interferometer arrays such as the Very Large Array (VLA) telescope, today's 21-cm observations allow us to probe and analyse the H I structure and content of galaxies in greater detail with (moderately) high — as compared to optical bands — resolutions of the interferometers. The strength of interferometric data is further fortified by the fact that the velocities at which the gas flows can also be observed (at velocity resolutions of a few to tens of km s^{-1}). The inherently low velocity dispersion and widespread distribution of H I over the entire galaxy makes it a good candidate for studying the dynamics of the system.

In this chapter, the H I-rich galaxy NGC 3359 will be studied in detail. The galactic gas content and structure will be probed and its overall H I mass estimated. Moreover, the kinematics of the gas will be analyzed with various methods. It will be shown that the gas flow is complex and the kinematical model made from simple assumptions satisfies only the general pattern of the observed velocity field. The development of more realistic hydrodynamical models in Chapter 4 will help explain the phenomenology seen in this chapter. Further discussions of the technical descriptions of the 21-cm emission and the data reduction method process are given in Appendices A and B.

The outline of the chapter is as follows. Section 2.2 presents the 21 cm data and the process of creating moment maps. In addition, the continuum field of the galaxy is also obtained and discussed in this section. The amount and distribution of H I within NGC 3359 is presented in Section 2.3. Next, Section 2.4 investigates the kinematics of the gas whereby the global properties and the rotation curve of NGC 3359 are obtained. The results from this section are used to create the axisymmetric model velocity field of the system as well as mass models in Section 2.5. The chapter concludes with a description of the satellite companion to galaxy in Section 2.6 and a brief summary in Section 2.7.

2.2 The Data

The 21 cm data that will be used for this dissertation were made from multiple measurements of the neutral hydrogen emission from the galaxy NGC 3359. All observations were performed at the Westerbork Synthesis Radio Telescope (WSRT[1]) in the Netherlands. A total observing time of 48 hours consisting of four 12-hour sessions were made to obtain the UV data.[2] The total bandwidth used in the observations, 2.5 MHz, was split up into 64 separate channels of 39.2 kHz (8.2 km s^{-1}) each. The central frequency at which the total bandwidth was centered on varied with the observation date. Table 2-1 gives the detailed list of the cursory information described above.

A total of 40 interferometers (antenna-antenna baselines) were used for the observations. The pointing center of the array was (RA, DEC) = $10^h43^m13^s.0$ and $63°27'42''.0$. The configuration of the WSRT array was set up so that the projected baselines ranged from 36 m to approximately 2.7 km. Standard data reduction processes, described in Appendix B, and a fast Fourier transform were applied to convert the UV data into a 512×512 square grid of $5''.004 \times 5''.004$ pixels. Thus, the field of sky coverage for each image is 42.7×42.7 arcminute^2. The combination of the two spatial and one spectral (velocity) axes form what is known as a data cube. Two separate cubes were created from the process that have, respectively, 15'' and 30'' angular resolutions. The first four and last three signal-free channels were trimmed off during the construction process to create the final data cubes. This data reduction and construction of the data cubes were made by the observer Dr. A. H. Broeils. He has kindly given me the permission to use the H I data for this thesis.

The mean r.m.s. noise of the cleaned cubes are 0.62 and 0.78 mJy per beam solid angle for the high and low resolution data sets. These values were obtained by taking the noise statistics of different areas that were free of line-signals. The corresponding brightness temperatures for the r.m.s. noise are 1.71 and 0.54 K, respectively.

---

[1] The Westerbork Synthesis Radio Telescope is operated by the ASTRON (Netherlands Foundation for Research in Astronomy) with support from the Netherlands Foundation for Scientific Research NWO.

[2] The initial raw data obtained from the radio observations. The "UV" term refers to the alignment of the telescope's baselines or the plane of the telescope array.

Table 2-1 Observational properties of the 21-cm data for NGC 3359

Parameter	
Telescope	WSRT
Observing Dates	December 1986 to February 1987
Total observing time	48 hours (4 × 12)
Number of interferometers	40
Baselines (minimum maximum increment)	36-2736-36 m
Pointing center R.A. (B1950)	$10^h43^m15^s.0$
Pointing center Dec. (B1950)	$63°27'42''.0$
Synthesized beam (FWHM)	
full resolution	$14.8'' \times 14.9''$
low resolution	$29.8'' \times 29.7''$
FWHP primary beam	$37'$
r.m.s. (1σ) noise per channel	
full resolution	1.71 K
low resolution	0.54 K
Bandwidth	2.5 MHz
Number of Channels	64
Channel Separation	
frequency	39.1 kHz
velocity	8.3 km s^{-1}
Velocity central channel	986.8 km s^{-1}
Temperature-flux conversion	
full resolution	2.76 K per mJy $beam^{-1}$
low resolution	0.69 K per mJy $beam^{-1}$

Channel maps of the 21-cm spectral line data are shown in Figure 2-1. Along with those that show emission greater than three times the r.m.s. noise value, two signal-free channels are included at each end of the figure. The central velocity value and number of each channel are displayed at the top right and bottom center of each frame respectively. In this and all subsequent figures, north is up and east is to the left. H I emission from the satellite of the galaxy, discovered by Ball (1986), can be seen in channels 22 – 25. The contour lines appear like flapping wings because surfaces of constant Doppler shifts on an inclined, rotating disk are parabolic in shape (Rupen 1989). As each channel of the data cube is limited by its frequency (velocity) width, only regions emitting the corresponding Doppler-shifted radiation will be seen.

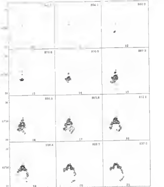

Figure 2 1 H I channel maps of NGC 3359 The central velocity of each channel is shown at the top right corner in units of km s^{-1} The 15″ beam is shown at the bottom right Contour lines are plotted at (−3 3 5, 7 10 and 16) × the r m s noise level per channel (1 7 K) Channels 10 to 21 of 53 (from upper left to bottom right panels) are shown on this page

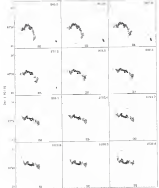

Figure 2.2 Contour map of channels 22 to 33 of the $15''$ data cube. Contour lines are plotted at (−3, 3, 5, 7, 10 and 16) × the r.m.s. noise level per channel (1.7 K)

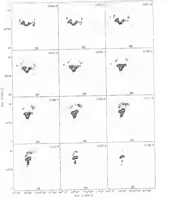

Figure 2-1 Contour map of channels 34 to 45 of the 15″ data cube. Contour lines are plotted at (3, 4, 5, 7, 10 and 15) × the r.m.s. noise level per channel (1.7 K)

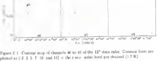

Figure 2.1. Contour map of channels 46 to 48 of the 15″ data cube. Contour lines are plotted at (-3, 3, 5, 7, 10, and 16) × the r.m.s. noise level per channel (1.7 K).

Figures 2.2 to 2-4 show three different views of data cube in its native 3-D form. It can be seen in Figure 2-2 that the blue-shifted side of the galaxy is located in the south. Assuming that the arms are trailing the rotation of the galaxy, the western half represents the near side toward us. In this orientation of the cube, the whole galaxy appears to rotate as a single system across the velocity plane (i.e., the velocity increases with declination). However, this view no longer holds when Figure 2-3 is viewed. Rather there are hints of three separate velocity systems delineated by major structures within the galaxy. The most discernible is the northern extension of the eastern arm that appears to have a slightly lower redshift than the main H I disk.

In Figure 2-4, the the velocity-declination plane of the data cube is shown. Running across the center of the diagram is the inner (∼ 70″) disk of the galaxy (the region between the two green horizontal lines). The H I region that contains the optical arms (the region between the two red lines) lies on another plane that is inclined at about 20° with respect to the inner disk. Finally, the features that form the steepest slope that runs almost diagonally across the diagram are the northern and outer western H I arms. Indeed, these structures do not rotate at the same rate. This 3-D representation of a velocity-declination plane is typical for a spiral galaxy with a (nearly) flat rotation curve in the outer part and a steeply rising central region. If the rotation curve were to fall off in a Keplerian manner to signify that the majority of the mass has been observed, the

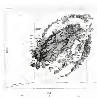

Figure 2.4 Three-dimensional representation of the galaxy. Note the slight change in the velocity phase of the outer arms.

outermost features would have a backward-S appearance. This is not seen in the figure and a flat rotation curve is expected for NGC 4488.

The most important information that can extracted from data cubes are its moments. These two-dimensional representations of the gas content of the galaxy not only offer a simpler way to view the original data but they also describe the physical field of the H I gas within the galaxy. All moments are calculated from the base equation

$$\text{moment}_n = \int T_B(x,y) V^n dV \tag{2.1}$$

The zeroth moment map is made by integrating the individual channel maps over all positions. The H I column density at a point (x,y) is given by

$$N_H = 1.8224 \times 10^{18} \int_0^{+\infty} T_B(x,y) dV \quad \text{atoms cm}^{-2} \tag{2.2}$$

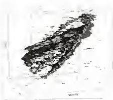

Figure [illegible] point of the three-dimensional representation of the galaxy. At this [illegible] be seen that the galaxy has three separate components that rotate at different rates.

Similarly the *temperature weighted* mean velocity of the point (i.e. the first moment) is calculated from

$$\langle V(x,y)\rangle = \frac{\int T_B(x,y)V(x,y)dV}{\int T_B(x,y)dV} \quad \mathrm{km\,s^{-1}} \tag{2.3}$$

(Allen et al. 1974)

Lastly the velocity dispersion of the line at (x,y) is defined as

$$\left\langle V^2(x,y)\right\rangle = \frac{\int T_B(x,y)V^2(x,y)dV}{\int T_B(x,y)dV} \quad \mathrm{km^2\,s^{-2}} \tag{2.4}$$

The brightness temperature of each pixel is calculated from

$$T_B(x,y) = \frac{c^2 S_\nu}{2k\nu^2\Omega} \tag{2.5}$$

where c is the speed of light, S_ν is the flux density per beam solid angle at the frequency of observation ν and k is the Boltzmann constant. The term Ω is the synthesised beam

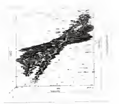

Figure 2 4 Same as Figures 2 2 and 2 3 but the Velocity Declination plane is shown here This diagram clearly shows that the inner and outer disk as well as the outer H I gas arms rotate at different rates

solid angle for the data The equations above assume that the gas is optically thin as is usually the case for H I (For the optically thick case, please see Appendix A)

In an ideal world where data contain only line emission a simple summation of pixels (with weights when applicable) would produce the moment maps However it is expected that any real emission from a specific location will exist only in a small range of contiguous channels Any peak that appears at the same pixel in non consecutive channels is likely a noise spike The physical argument is that any region of gas will emit spectral lines for a range of frequencies due to the motion of the galaxy and unless the disk is warped the line peaks should appear only once in a narrow range of velocities in the data. In the case of (extreme) warps the line-of-sight may intersect more than once the same point in the galaxy Thus a simple integration of the all strong emission peaks can produce images that are filled with more noise than signal owing to the inclusion of spurious noise spikes A more detailed discussion of this matter has been written by Bosma (1981)

All of the moment maps that are used in this thesis have been created from the task MOMENTS in the WSRT's data reduction program GIPSY (Groningen Image Processing SYstem). The program has taken the problem of noise spikes in data cubes into consideration and attempts to ameliorate it by combining the standard practice of noise reduction (cut off method) with the "window" method introduced by Bosma (1981).

The first step in creating the moment maps is to create a mask cube. This data set is the product of convolving the original data cube's spatial and velocity axes with a Gaussian and Hanning kernel respectively. Next, a threshold level is set to eliminate the smoothed pixels whose values lie below the specified acceptance gate. Then the window method is used to process the remaining "good" pixels. At each pixel, the velocity of the peak profile is first determined and an initial window is established. Values outside the window are estimated and then the size of the acceptance gate is widened gradually in velocity. For each subsequent iteration, the values outside the window are compared with those of the previous window. Eventually both values will reach an accepted tolerance value and the window procedure is stopped for that pixel (see Figure 2 of Bosma 1981 for a good graphical representation of his method). The acceptance level is a combination of the r.m.s. noise level of a channel map plus a "continuum" level that is empirically defined (England 1986). In this way, single channel noise spikes are eliminated from the maps and line-signals, which are contiguous for a number of channels, remain. Pixels that do not pass either of these criteria are flagged and the corresponding pixels in the original data cube are set to "blanked" out (i.e. set to undefined values). Unblanked pixels are then integrated to make the desired moment map(s).

To create the moment maps that are analyzed in this chapter, the initial cube was convolved with a Gaussian kernel of two beam width in spatial position along with a running, three-point Hanning function. This velocity smoothing kernel has the form

$$X_n = 0.25X_{n-1} + 0.5X_n + 0.25X_{n-1} \tag{2.6}$$

where n is the current channel of analysis. The moment maps were created by summing up all the pixels of each individual channel that had values greater than $|\pm 2.5|$ times the av[illegible] level (Table 2.1) of the cube. This ensured that any positive bias were excluded [illegible] of the maps typically spanned four channels on average.

Three additional information that are gathered from the data cubes that will also be utilized to analyze the physical properties of the H I gas are (1) the global profiles, (2) the continuum field, and (3) the position velocity profile maps. The first is derived by integrating the total flux of the 21-cm emission from each channel of the data cube with respect to velocity axes. The second can be obtained by analyzing the line-free channels of the cubes. The process is described more fully in subsection 2.3.4. And lastly, position velocity (PV) plots are made by taking slices through one of the coordinate axes and the velocity axis. This method allows follow the distribution and flow of gas at specific positions along the slice through a range of velocities. As PV diagrams pertain to the kinematical behavior of the gas as well as its intensities, they will be discussed after the distribution of H I and the kinematics of the gas have been reviewed.

2.3 H I Distribution and Continuum Emission

2.3.1 Global H I Properties

The global profiles of the galaxy for both 15″ and 30″ data sets are shown in Figure 2.5. Despite the large number of lop-sidedness profiles[3] that have been observed (Haynes et al. 1998, Richter & Sancisi 1994), no clear evidence of such feature is seen for NGC 3359 (i.e., the difference between the two "horns" of each spectrum is only 30 mJy (4% of the profile peak). The width at 20% of the peak flux (W_{20}) is 267.7 km s^{-1}. Single-dish measurements by Staveley Smith & Davies (1988) and Tifft (1980) have yielded results of 264 km s^{-1} and 269 km s^{-1} respectively. However, it has been pointed out by Broeils & van Woerden (1994) that W_{20} must be corrected for instrumental broadening. The correction W_{20}^c (Bottinelli et al. 1990) takes the general form

$$W_{20}^c = W_{20} + (a \cdot l + b) \cdot \Delta v \tag{2.7}$$

---

[3] This term refers to the asymmetric distribution of H I with respect to the center. One clear case of lop-sidedness in a galaxy is M101 (Kamphuis et al. 1991).

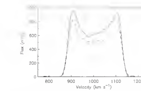

Figure 2.5. Global profiles of the galaxy at 15″ (dashed) and 30″ (solid line) resolutions

where $a = 0.0014$, $b = -0.83$, l is the percentage level, and Δv is the velocity resolution. For NGC 3359, $W^c_{20} = 261.0$ km s^{-1}. The line-of-sight systemic velocity, as determined from the midpoint of the 20% width-level, is 1006.4 km s^{-1}. This value compares favorably with the 1008 km s^{-1} value of Ball (1986) and 1006.7 km s^{-1} of Rozas et al (2000b) that was derived from their Hα data analysis. Similarly, Staveley-Smith et al (1988) found 1012 km s^{-1} with their data.

To calculate the total H I flux and mass of the system, the 15″ moment was eschewed in favor of the 30″ map that is more sensitive to the low surface brightness features owing to the larger beamsize. First, the only the area where emission arises from the galaxy was integrated and then multiplied by the pixel size (in arcseconds^2). The derived value (in units of Jy beam^{-1} × km s^{-1}) was then divided by the beam size to produce the total H I flux of 195.6 Jy km s^{-1} for the galaxy. The result is in good agreement with those (139.4 – 204.1 Jy km s^{-1}) given by the H I catalog of Huchtmeier & Richter (1989). Staveley-Smith & Davies (1988) and Tifft (1990) reported their findings as 193.7 and 131.6 Jy km s^{-1}, respectively. Finally, by applying equation A.3 from Appendix A, the total H I mass is determined to be $M_{HI} = 5.6 \times 10^9$ M$_\odot$. Single-dish measurements have yielded H I masses of 5.8×10^9 M$_\odot$ (Rots 1980), 6.1×10^9 M$_\odot$ (Fisher & Tully 1981)

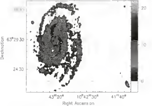

Figure 2-6. H I surface density map of NGC 3359 and its satellite. The contours are at plotted one (2.5σ), 2.5, 5, 10, 15, and 20 $M_{\odot}$ pc^{-2}. The 15″ beam is plotted at the upper right corner of the diagram.

and 5.6×10^9 $M_{\odot}$ (Staveley-Smith & Davies 1988). Hence, the observation made by the WSRT interferometer does not appear to have any significant loss of emission due to the lack of short baseline coverage or the zero-spacing issue.

2.3.2 H I Surface Density Distribution

Figure 2-6 shows the zeroth moment map of NGC 3359 seen at 15″ resolution. Throughout this chapter, the area confined within the inner ~ 9′ (i.e. 26.8 kpc) of the major axis of the galaxy will be referred to as the main H I disk (i.e., excluding the outer gas arms). This feature is larger than the D_{25} of the 25 mag arcsec^{-2} B-band isophote (RC2) by almost 25% and contains the northern and southern optical gas spiral arms of the galaxy (Figure 2-7). Protruding from the left and right of the H I disk are the eastern and western gas arms that, when traced out, appear to be continuations of the southern and northern parts of the western of eastern optical gas arms respectively.

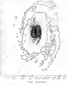

Figure 2.7 1.25 $M_\odot$ isodensity contour line of the $15''$ data highlighting the extent of the H I distribution as compared to the stellar component of the galaxy (the grayscale Digital Sky Survey B-band image)

The distribution of the gas within the main disk is generally symmetric with the two long continuous arms, giving the galaxy a "grand design" appearance (Elmegreen 1981). The cloud complexes are distributed in clumpy patches throughout the galaxy down the limit of the resolution (~ 800 pc). The total extent of the H I content[4] encompasses a length of about 48 kpc along the major axis. The maximum column density projected onto the sky, is $N_H = 2.8 \times 10^{21}$ atoms cm^{-2} (22 $M_\odot$ pc^{-2}) and the average density is 7.8×10^{20} atoms cm^{-2} (6.3 $M_\odot$ pc^{-2}). This peak is situated in southern arm near a bright H II region. The locations of the highest gas concentration tend to be distributed around the main arms of the H I disk as they represent strong potential wells where the gas can be easily trapped.

In showing the global symmetry between the arms Ball (1986) measured the winding of the spirals at various radii. It was found that the pitch angles of both arms

---

[4] The low resolution data was used to determine the H I diameter of the galaxy, Figure 2.13

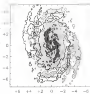

Figure 2 8 A grayscale surface density map with contours from its mirror image. Good symmetries exist between the main disk and arms of the galaxy The asterisk marks the center of the galaxy

were in agreement especially at larger radii. The mean values derived for the logarithmic spiral fit were 19° for the southern arm and 16° for the northern arm with the former being better approximated The large angular values are consistent with late type galaxies that have loosely wounded arms On average the H I density of the outer arms is about three times less than that of the main disk The eastern gas arm is well-delineated starting from almost immediately east of the nucleus and curving around the north before ending at a position angle of +30° east of north and about 22.5 kpc away from the center The western arm appears to split into a fragmentary inner part and a thicker section that forms the outermost region of the galaxy Their attachments to the galactic disk are not as easily distinguishable nor do they wrap around the disk as much as their eastern counterpart

Figure 2-8 displays the symmetry that exist for the two halves of the galaxy The plot shows that the eastern arm resembles the inner western arm more so than the outer in radial displacement from the center as well as the winding angles The figure also displays the highly symmetric distribution of gas between the northern and southern halves of the main disk. Just beyond the southern edge of the disk lies a patch of H I that breaks the symmetry between the two sides. This addition of gas extends the south side by about 2.7 kpc more than the north and has an estimated H I mass of 1.6×10^7 $M_\odot$. Due to the spurious arrangement of the H I clouds in the inner western arm, it is not clear whether this area of gas is actually part of it although the contour line of the mirror image mildly indicates the possibility.

Near the (stellar) bar region, the H I arms wound around and form a rectangular shape pseudo-ring of 60′ in projected radius. Confined within the ring is the gas deficient central region of NGC 3359. This phenomenon is not uncommon as our neighboring galaxy M31 also has a centrally-depressed region of atomic neutral hydrogen in its H I distribution. The lack of H I in this area is probably caused by the sweeping motion of the bar that funnels the gas (as it loses angular momentum near the bar ends) toward the nucleus. The inflowing gas can form shocks or gas compression that lead to the formation of new stars (as seen along the bar of NGC 3359). These two phenomenons are addressed in the Chapter 3. Although it is possible that the center could be filled with molecular hydrogen, past CO observations of the system, as reviewed in the last chapter, indicate that NGC 3359 emit weakly in the millimeter wavelength regime. Hence, it is more than likely that the H I gas of this region is associated with the star formation lying along the bar of the gas.

2.3.3 Radial H I Profile

A more quantitative study of the H I distribution can be performed by analyzing the radial density profile of the galaxy, as shown in Figure 2-9. The peak of this azimuthally averaged profile corresponds to the gas-enhanced pseudo-ring. The surface density is approximately 27% higher here than the central region. Some the densest H I regions of the galaxy reside in the southern arm and are covered by a single annulus used in the construction of the profile. This local enhancement has created the second peak in the plot. After this peak, the density drops off rapidly and the slope of the gradient can be fitted by an exponential of the form

$$\Sigma(r) = \Sigma_0 \, e^{-(r/h_{HI})} \tag{2.8}$$

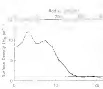

Figure 2-9 Surface density radial profile of NGC 3359 Filled circles represent the best-fit exponential function to the decreasing part of the profile The horizontal line denote the 1 $M_\odot$ pc^{-2} level

From the equation above I derived the H I scale length h_{HI} = 7.0 ± 0.1 kpc for the galaxy The surface density reaches the D_{HI} level of one $M_\odot$ pc^{-2} at approximately 280″ or 1.3R_{25} within the range of 1.7 ± 0.5 that Broeils & Rhee (1997) found with their sample of 108 spiral and irregular galaxies.

2.3.4 Continuum Map

Along with the (continuum-subtracted) clean cubes that have been used to derive the previous results the UV data of the observations made by Dr Broeils were also obtained and re-reduced them to determine the extent of the continuum emission near and from the galaxy The map was made by averaging line-free channels 4 – 12 and 51 – 58 of the original 64-channel data then "cleaning" (Appendix B) the product down to the expected noise r m s level The continuum field at 14.03″ × 12.80″ resolution is displayed in Figure 2-10 More emission has been detected than that found by Ball (1986) although the same core source of radiation is found near the center No detectable radio continuum is found near the type II supernova 1985H although the data was taken shortly after the explosion Rather the locations of the peaks tend to coincide with areas of star formation that hints at the continuum arising from thermal processes rather

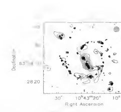

Figure 2 10 Radio continuum emission seen around the galaxy The center of the galaxy is marked by the asterisk The star marker denotes the supernova 1985H as reported by Kristian, Nemec & Staples (1985) Contour levels are at 3 5 7 and 11 times the rms noise level of 0 37 K The beam size of observation is plotted at the top right

than synchrotron radiation The continuum field is dominated by the H II regions along the bar followed by a patch of ionized hydrogen northeast of the galactic center It will be shown in Chapter 3 that these two areas are also some of the highest flux-emitting regions observed in the Hα Balmer line

2 4 H I Kinematics

2 4 1 Velocity Field

The first moment maps of NGC 4389 made from Equation 2 3 are shown in Figures 2 11 to 2-13 Figures 2-11 and 2 12C are Renzo diagrams showing isovelocity contour lines (isovels) plotted atop the H I surface density image The underlying design of the isovels is similar to a typical "spider" pattern of a rotating disk that has been projected onto the sky plane The spider diagram of Figure 2-12A is a velocity contour map of a circularly rotating disk that is inclined to the line-of-sight It is a velocity field of an idealized rotation curve with Keplerian fall off at large radii In the diagram, the ovals indicate the locations of the maximum rotation velocities of the rotation curve The only velocity component that can be observed along the kinematical minor axis is the systemic

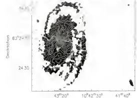

Figure 2-11. The velocity fields of NGC 3359 and its satellite. The contour levels are from 850 to 1150 km s^{-1} in steps of 10 km s^{-1}. The heavy white line denotes the systemic velocity. The 15″ beam is plotted at the upper right corner of the diagram.

velocity of the galaxy. This constant value is depicted by the vertical middle line. The other principal axis of the system, the kinematical major axis (not shown), bisects the ovals and the galactic center. In principle, the two axes should be perpendicular to each other but strong streaming motions along the bar can offset this alignment.

It is clear that there are significant non-circular motions that manifest themselves as kinks in the velocity field contour lines of Figure 2-12C. The largest deviations from circularity are near the bar and spiral arms. Around the neighborhood of the arms, this velocity streaming (Gottesman & Weliachew 1975; Rots 1975) effect is caused by the response of the gas flow as it travels through the density waves that make the arms. The effect appears to be especially strong on the eastern side of the galaxy where the velocity displacement is more pronounced than the other side. The undulating velocity contours of the approaching (southern) half is bent by a greater degree than the receding half in general. The fragmented western arm just beyond the disk seems to have little effect on

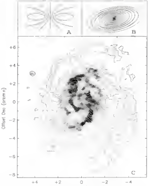

Figure 2-12 Example plots of A) the spider diagram of a Toomre disk and B) a sample set of tilted-rings used to determine the rotation curve of the galaxy. C) Isovelocity contours overplotted on grayscale image of the moment zero map

the materials moving through it as the isovels remain fairly [illegible] passage. However the systemic velocity contour line is skewed the observed kinks indicate the presence of non-circular motions that will be investigate further in subsection 2.4.3. The closed contour lines on the velocity map represent the maximum value of the observed rotational velocity.

In the neighborhood of the galactic nucleus, the isovels head toward the east along the bar major axis. The contours within the bar region aligning themselves into an S-configuration as seen in many other barred systems. This is expected for the gas flowing in elliptical orbits around the bar (Huntley et al. 1978, Prendergast 1983, Sanders & Huntley 1976, Sellwood & Wilkinson 1993, van Albada & Sanders 1982). The contours are turned toward the bar in such a way that they appear to be pinched together at two diametrically opposing positions located northwest and southeast of the bar. As this area contains mainly elliptical motions, it will be excluded in the processes used to derive the global H I kinematical parameters of the galaxy that will be discussed next.

2.4.2 Global Kinematical Properties

Consider a galactic disk that has its kinematical major axis rotated by the position angle ϕ and is inclined at an angle i from the line-of-sight. The observed velocity at any point (x, y) on the disk can be described by the equation

$$V_{obs}(x, y) = V_{sys} + V_c(r)\cos\theta\sin i + V_{nc}(r)\sin\theta\sin i + V_z(r)\cos i \tag{2.9}$$

where V_{sys} is the systemic velocity of the center of the galaxy (x_0, y_0), V_c and V_{nc} are the circular and non circular (radial) velocity components of the observed velocity, and V_z is the velocity in the z direction. The azimuthal angle θ is related to (x_0, y_0), i, and ϕ by the equations

$$\cos(\theta) = \frac{-(x - x_0)\sin\phi + (y - y_0)\cos\phi}{R} \tag{2.10}$$

and

$$\sin(\theta) = \frac{-(x - x_0)\cos\phi - (y - y_0)\sin\phi}{R\cos i} \tag{2.11}$$

The position angle is measure counterclockwise from the north in the plane of the sky to the major axis of the receding half of the galaxy. For the present case, the radial term and vertical [illegible] motions are assumed to be small [illegible] as is typical for disk galaxies.

The unknown kinematical properties just defined have been found by using an ensemble of individual rings (Figure 2-12B) to model the observed velocity field. The rings can be assigned separate sets of initial values so that each ring is completely independent from another in the fitting algorithm. GIPSY's ROTCUR program and the iterative scheme of Begeman (1989) were used specifically to derive the desired parameters. The Begeman algorithm is a refinement of the methods employed earlier by Warner et al. (1973) and Gottesman & Weliachew (1975).

Initial estimates of the unknown parameters needed to start the tilted-ring method were taken from previous observations of NGC 3359. These values were used to derive calculated velocity values that were then fitted to the observed line-of-sight velocity with least squares minimization. This produced new and improved input parameter values that were subsequently used for the next iteration step. The procedure is continued until a level of χ^2-minimization is reached. As weights can also be assigned to each pixel, those that were near or along the kinematical major axis are assigned the highest importance as they carry most of the information about the circular velocity of the galaxy. Similarly pixels near the minor axis were weighted the least owing to the fact that the observed velocities are mostly radial. The determination of the global parameters were made with the lower resolution 30″ data (Figure 2-13) to minimize the inclusion of local non-circular perturbations near the arms and the bar region.

The kinematical center (x_0, y_0) was the first term determined. The initial value of the center from the NASA/IPAC Extragalactic Database (NED[5]). The initial systemic velocity, position angle and inclination values, taken from Rozas et al. (2000b) were 1006.8 km s^{-1}, −10° and 53°. These three values were held fixed during this stage. It was found that the fitted values was effected by structures within the disk and hence the solutions did not converge. The centers of the annuli [illegible] north northwest and southwest of the NED center at different radii. Thus no accurate determination could be made from the annuli fit. Although dynamical centers of galaxies have been found not to coincide with their optical counterparts (e. g. Knapen 1997, Ryder et al. 1996), it is also not uncommon to assign both centers the same values (Moore & Gottesman 1998, Weiner et al. 2001).

---

[5] NED is operated by the Jet Propulsion Laboratory, California Institute of Technology, under contract with the National Aeronautics and Space Administration.

The second parameter solved was the systemic velocity of the galaxy. This was done by keeping the dynamical center and inclination constant while using ROTCUR. Owing to the large formal errors (up to 4.6 km s^{-1}) for the inner ring solutions and near steady values of V_{sys} in the middle region of the galaxy (between $180'' < r < 420''$), the adopted heliocentric velocity for the galaxy, based on 21 cm observations, is the (error) weighted mean value of 1005.2 ± 0.1 km s^{-1}. This value is in agreement with the global profile determination of 1006.5 km s^{-1}, the 1006.7 km s^{-1} and 1008 km s^{-1} results from Rozas et al. 2000a and Ball (1986) respectively. Gottesman (1982) found V_{sys} = 1024 km s^{-1} for the galaxy.

To find the position angle and inclination of the galaxy, the region between 13 – 23 kpc was used as the solutions remained stable and varied the least within this neighborhood. The individual ring fits for each parameter are shown in Figure 2-14. Starting with the $\phi = -10°$ (Rozas et al. 2000b) and holding (x_0, y_0), i, and V_{sys} constant, the position angles of the rings fitted to produce the weighted mean value of $-9.8° \pm 0.8°$.

Likewise, at radii beyond 13 kpc, the ring solutions for i stabilized and did not vary by more than 2° from one another. The average value of i, as determined from annuli fitted to both halves of the galaxy, is 52°. This is the same value as found by Broeils & van Woerden (1994) and one degree more than the value found by Gottesman (1982) who used the NRAO's three-element interferometer and Ball (1986) who used 21-cm observations from the Very Large Array telescope. Rozas et al. (2000b) found $i = 53°$ based on their Hα kinematical study of the galaxy.

Moore & Gottesman (1995) and Weiner (2001) have pointed out that inclination angles will typically increase in areas with considerable streaming motions. This is also the case for NGC 3359. The highest value for i coincides with the outer eastern spiral

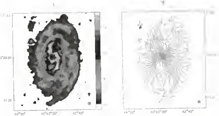

Figure 2-13 Low resolution surface density and velocity field of NGC 4359. A) Isodensity contour lines at levels of 0.4 (3σ), 1, 2, 5 to 15 $M_\odot$ pc^{-2} by 3 $M_\odot$ pc^{-2}. B) Isovelocity lines are from 850 to 1150 km s^{-1} in steps of 10 km s^{-1}. The beam is plotted at the bottom right of each image.

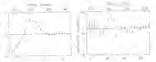

Figure 2.14. Individual ring fits to the position angle and inclination angles of the galaxy using the 30″ first moment map. Error bars denote the formal errors from the least-squares fit.

arm where the streaming motions are strong. The pixels within this area are the most disturbed for any of the arms of the galaxy. However, since the effect is localized and the fit is steady at larger distances, the final result of $i = 52 \pm 2°$ has been selected as the best inclination value for NGC 3359.

2.4.3 Rotation Curve

The rotation curve of the galaxy was determined by using the previously derived kinematical properties and both the 15″ and 30″ velocity fields. The higher resolution map will mitigate the effect of beam smearing in the central regions that cause V_c to be underestimated (Teuben 2002). But the lack of sample points beyond the main H I disk of the galaxy (near $r = 13.3$ kpc) necessitated the use of the lower resolution data, in that more signal (and hence sample points) is detected in the interarm region than the 15″ data. The rotation curve of the whole galaxy, obtained from combining both sets of data, is shown in Figure 2-15. The circular velocities for the approaching and receding sides were also estimated and are plotted in the same figure. The radial extent of the graph is $7'.25$ (23.2 kpc). Beyond this radius, the lack of sample points led to velocity estimates with extremely large and unacceptable errors.

Overall, both sides of the galaxy appear to be rotating with similar speed as a function of radius. The exceptions are the bar region (where strong elliptical gas motions make the estimates for V_c difficult to determine) and in the area between $\sim 6.5 - 10$ kpc

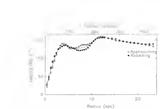

Figure 2–15 The rotation curve of NGC 3359 for both sides (solid line) as well as the blue- and redshifted halves of the galaxy (open circle and filled squares respectively) The 30″ data was used to construct the final 10 kpc of the diagram

Owing to this symmetry it can be inferred that the kinematical center must be close to or possibly coincide with the NED optical value that has been in used throughout the analysis

From 6 to 10 kpc the difference (maximum value = 13 7 km s^{-1}) between the two halves can be attributed to the spiral arms within the disk The annuli used to fit the approaching half of the galaxy within this vicinity show higher velocities because they lie at the outer edge of the southern arm where streaming motions add to the rotation curve (Rohlfs 1978) Excluding the region just discussed, the average difference between the two sides for the whole galaxy is less than 3 km s^{-1}

The rotation curve within the first 3 kpc from the center can be described by solid-body rotation that rises steeply at a rate of 144 ± 6 km s^{-1} $arcmin^{-1}$ (45 km s^{-1} kpc^{-1}) Previous measurements made by Ball (1986) and Rozas et al (2000b) at similar radii have yielded values 160 ± 15 and 142 ± 6 km s^{-1} $arcmin^{-1}$ respectively The secondary maximum of the rotation curve ($\sim$ 140 km s^{-1} at 4 kpc) occurs just slightly beyond the bar area. Between 4 and 7 kpc the rotation curve descends to a minimum value of $\sim$ 125 km s^{-1} before rising again until V_{max} is reached. This peculiar region begins from the

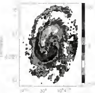

Figure 2-16. The residual velocity field made from subtracting out the circular component of the observed data. The ellipses denote the region between the double peak feature seen in the rotation curve. The straight line marks the major axis of the galaxy.

end of the pseudo-ring region and continues outward just short of the edge of the H I disk thereby encompassing the two inner (optical gas) arms of the system.

The most striking aspects of the rotation curve are its two peaks. The second peak of the curve is the true maximum rotational velocity of the galaxy (Figure 2-15). It occurs just slightly before the edge of the main H I disk at ~ 12.8 kpc (240″) and has a value $V_{\max} = 158$ km s^{-1}. After this point, the rotation curve begins a long and slow decline for about 8.5 kpc (nearly two-thirds of the gas disk) until the last point is reached. The rate of change is -2.0 ± 0.1 km s^{-1} kpc^{-1}. This is above the Keplerian drop-off in velocity at large radii that is expected for a system that has its total mass confined within the observed maximum radius. As in many rotation curves of other disk galaxies (Rubin et al. 1985), the slow decline is typically conjectured to be caused by the existence of undetected matter.

To analyze and locate the non-circular components of the observed velocity, a circularly rotating model was made using the rotation curve as a guide. Figure 2-16 shows the residual velocity field from the subtraction of the model from the observed

Table 2.2 Kinematical and Physical Properti[illegible] based on the [illegible] data

Parameter	Value
Kinematical center (B1950.0)	
Right Ascension	$10^h43^m20^s.14$
Declination	$63°29'15''.8$
Systemic velocity (km s^{-1})	1005.2 ± 0.1
Mean inclination, i (degrees)	52 ± 2
Mean position angle ϕ (degrees)	-9.8 ± 0.8
Maximum rotational velocity (km s^{-1})	158.11 ± 0.67
H I scale length (kpc)	3.0 ± 0.1
H I disk radius (kpc)	24.0
Maximum surface density of H I ($M_\odot$ pc^{-2})	22.2 ± 0.8
Total atomic hydrogen mass ($M_\odot$)	$5.6 \pm 0.01 \times 10^9$
Total mass ($M_\odot$)	9.9×10^{10}

velocity field. The area encircled by the two red ellipses correspond to the region between the two velocity peaks of the rotation curve. Within the annulus, large non-circular motions with (projected) values of 40 km s^{-1} are noticeable. In the plane of the galaxy, this translates to non circular motions in excess of 50 km s^{-1} and are sufficiently large enough to produce the odd depression in the rotation curve at 8.8 kpc. Hence, the velocity minimum is caused by the the optical gas arms of the main disk and is not a phenomenon associated with circular motions. Rotation curves of other galaxies are known to have two velocity peaks (Kent 1987), but such occurrences are not common. Clearly, this shows that NGC 3359 possesses strong spiral arms.

The total dynamical mass is another physical property of the galaxy that can be determined with the aid of the rotation curve and also the equation

$$M_T(R) = 2.33 \times 10^5 \left(\frac{R}{kpc}\right)\left(\frac{V^2}{km\,s^{-1}}\right) M_\odot \tag{2.12}$$

(Giovanelli & Haynes 1988). For NGC 3359, the total mass interior to the last measured point of the rotation curve, at $R = 23.2$ kpc and $V = 135.4$ km s^{-1}, is 9.9×10^{10} $M_\odot$. The models of Generalized Mestel, $n = 1$ Toomre, and exponential disks of Ball (1986) approximated the total mass values of 1.12, 1.30, and 1.19×10^{11} $M_\odot$ respectively. The calculated M_T, along with the rest of the results found in this section are given in Table 2.2.

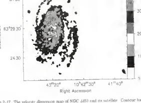

Figure 2-17 The velocity dispersion map of NGC 3359 and its satellite Contour lines are from 5 to 40 km s^{-1} in 5 km s^{-1} steps The 15" beam is plotted at the upper right corner of the diagram

2 4 4 Velocity Dispersion Map

The second moment map of the galaxy is displayed in Figure 2 17 This moment is a measure of the r m.s. value of the velocity of each pixel (α δ) and can be expressed formulaically as

$$\sigma \equiv \sqrt{\left\langle [V_i - \overline{V}(\alpha\ \delta)]^2 \right\rangle} \tag{2 13}$$

where i is the velocity channel and $\overline{V}$ is the temperature weighted mean velocity (Equation 2 3) Large velocity dispersions occur in areas where emission exists for an extended number of channels. In areas where σ is between $15 - 20$km s^{-1} emission can be detected in $8 - 11$ successive channels Approximately 11–13 channels contribute to the two highest peaks near the center One reason why the central region has the highest average dispersions is due to the steep velocity gradient of the rotation curve being smeared out by the beam (Laine 1996 Moore & Gottesman 1995) As the curve flattens at larger distances from the center the effect of beam smearing is lessened and

Consequently so does σ For NGC 3359 the average value decreases to σ 10 km s^{-1} $1-\sigma$ and the radius of 11 kpc These values are common for spiral galaxies The overall observed r m s velocity that is present in the figure also includes other line-broadening mechanisms such as instrumental width thermal broadening and natural linewidth In addition the dispersions may not be confined within the disk but also include vertical motions whose values typically do not exceed 10 km s^{-1} as seen in face-on galaxies (Laine 1996 Lewis 1984)

There also appears to be a correlation between areas of high dispersion and the distribution of ionized hydrogen gas of the galaxy There are strong H II regions that appear to be associated with places where H I emission is continuous for many channels (Chapter 3) This is especially true for the two peaks of Figure 2-17 as they coincide with two of the strongest H II regions that are strung out along the Hα bar of the galaxy

2 4 5 Position Velocity Diagrams

As mentioned earlier a plot of a slice through the data cube parallel to the velocity axis is known as a position velocity (PV) diagram This powerful tool is typically used to inspect the gas motions within the plane of the galaxy and has the potential to trace the out-of plane motions or structures that cannot be inferred from the two-dimensional velocity field under normal circumstances

Figure 2 18A shows a PV plot made from taking a slice along the major axis of the galaxy at the position angle = −10° The contours trace out the rotation curve of the galaxy that is marked by the filled circles The part of the gas ring that lies on the major axis distinguishes itself as peaks near 65″ on either side of the center The 3σ contour lines of the main disk extend out further in the southeast region by about 1 3 kpc than the northwest side This slight overdensity also manifests itself as the small additional flux density of the left peak of the global profile Patches of gas of the same intensity further lengthen the southeast side to about 18 kpc while in the northwest the one region of equal intensity is situated at approximately 19 2 kpc from the center The location of

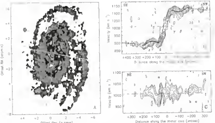

Figure 2 18 Position velocity plots of the minor and major axes of NGC 3359 A) Slice configuration for the P V plots shown B) Position velocity diagram of the major axis ($\phi = -10^\circ$) Dash dot line represents the systemic velocity of the galaxy Contour lines are at 2 2 3, 6 10 14 and 18 times the r m s level of 1 7 K See text for notes on the letters C) PV diagram of the minor axis ($\phi = 80^\circ$)

this solitary region (labeled by the letter α) coincides with the northern extension of the eastern arm. The gas is more extended in the southern part of the galaxy in general.

Of more interest is the minor axis slice (Figure 2-18C) taken at the position angle of 80°. From Equation 2-9, it is apparent that only radial and out-of-plane terms of the velocity will show up along the minor axis. If these motions are absent, only the systemic velocity will be present. The left side of the plot shows gas moving at lower velocities than the expected V_{sys} that one would expect for material that is rotating in a circular fashion. The maximum deviation (point α) is located at the middle of the eastern arm and has a magnitude of 30 km s^{-1} as seen along the line-of-sight (38 km s^{-1} deprojected). The second moment map shows that there are large velocity dispersions (> 20 km s^{-1}) within the proximity of α as well. Near the center of the spiral arm, gas responding to the spiral density wave perturbation will move radially inward (Rohlfs 1977). Point α is an example of the gas flowing toward the center. There is no such effect seen west of the nucleus. Along the western (right) half of the galaxy, small differences between the gas velocities at points **b** and **c** and V_{sys} could be due to either radial motions within the plane or to out-of-plane motions. The situation is unclear although the latter is more probable. Additional support for this conjecture is seen in Figure 2-4 that shows that the outer western arms are not properly aligned with the main disk of the galaxy (spectrally).

It has recently been suggested by Fraternali et al. (2001) that inspection of the PV plots for non edge-on galaxies can show the existence of thick H I disks. In the current scenario, the gas disk actually consists of two parts: the regular cold disk component and a surrounding (vertically) thick H I layer that rotates at a slower rate. In addition, there is also an associated inflow motion from the outer hydrogen envelope that presents itself as features called "beards". These features can be seen in the position-velocity diagrams as gas extending from the main disk toward the systemic velocity. There appears to be beards in the major axis slice near or at points β, γ and δ. To increase the signal-to-noise ratio for further examination of the three points, an additional but thicker slice along the major axis was made. The result, a 15″ wide PV plot (Figure 2-19), shows an additional (possible) beard that is symmetric with δ some $\pm 50''$ from the galactic

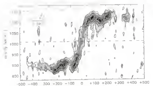

Figure 2 18 Position-velocity plot of the 15″ wide slice along the major axis of the galaxy

center The location of these two features coincide with the gas ring and the gas may be streaming around the spiral arms rather than falling in from the layer above. Near β there is no particularly striking feature that coincides with the position However the most interesting case for infalling material is at γ It can be seen from Figure 2 18A (or Figure 2 2) that there is a dense region of H I in within the vicinity of this point More interestingly is the fact that a small star formation region also exists within the area. The zone is isolated from the spiral arms of the galaxy that could have induced its formation The velocity range of this particular beard extends from the observed rotation curve of ~ 130 km s^{-1} down to approximately 15 km s^{-1} Owing to this fact it is possible that what we are seeing is a gas complex similar to the intermediate-velocity clouds (IVCs) that are observed in the Galaxy It may also be possible that some of the infalling material has caused stars to form in the area through cloud disk collision Tenorio-Tagle (1981) has shown that an IVC colliding with a high density area releases an energy of approximately 10^{47} to 10^{52} ergs that is sufficient to instigate the formation of giant H II regions However the contour that outline the beards is at the 2σ level so their actual existence are circumstantial but tantalising

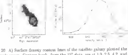

Figure 2.20 A) Surface density contour lines of the satellite galaxy plotted the 30″ grayscale image. Contour levels, from the 15″ data, are at 1.3, 2.5, 4.2 and 6.2 $M_\odot$ pc^{-2}. The B) Global profile of the satellite.

2.5 Satellite Galaxy of NGC 3359

Located toward the southwest of NGC 3359 is the satellite galaxy that Ball (1986) discovered. The companion can first be seen in four channels of the data cube (velocity range 945.3 − 970.2 km s^{-1}) in Figure 2-1 and most conspicuously in the moment maps.

Recent literature and catalog searches for the object have yielded little information on it. Emission in other wavelengths by the gas cloud is extremely deficient although a recent blue image of a digitized photographic plate obtained from the Digital Sky Survey (DSS) shows a very faint structure. However, a single pixel peak signal is no more than 1.5 times the background sky value and extremely difficult to see. A similar search was performed on the red DSS image and although several pixels were marginally brighter than the sky region, the object is so ill defined that no definitive detection can be concluded. A search around the area with NED, which usually reports recent published results electronically, yielded no findings.

The left diagram of Figure 2.20 is the surface density map of the galaxy at 30″ resolution with the contour lines from the high resolution data. The contours show that the core of the cloud appears to be elliptical in shape. The maximum column density $n_H = 1.0 \times 10^{21}$ atoms cm^{-2}, is located around the galactic center. Based on a two-dimensional (2-D) Gaussian fit made at 1.5 × 10^{20} atoms cm^{-2} (3σ level), the projected major and minor axes of the core are 2.8 kpc and 1.4 kpc respectively. The center of the Gaussian ellipse is located at the (B1950) coordinate RA = 10^{h}41^{m}23^s.6 and Dec =

[illegible] 1′7. This pos[illegible] with Ball (1986) who found RA = $10^h41^m25^s.6$ and Dec = −63°21′9. The distance between this point and the center of NGC 3359 is 47 kpc assuming that both objects are at equal distances from us.

The atomic hydrogen mass within the core is 1.5×10^7 M$_\odot$. The 30″ zeroth moment image shows a tail structure extending out for ∼ 8.0 kpc and pointing in the direction of NGC 3359. The total neutral hydrogen mass of the H I complex, after integrating the column density over regions (the left panel of Figure 2-20) with values of 3σ and higher is 5.9×10^7 M$_\odot$.

The velocity field of the gas cloud is a juxtaposition of random motions and although no orderly motion can be traced out with certainty, there does appear to be a slight hint of rotation such that the receding side of the satellite is situated to the north. The small velocity gradient that may exist is in the range of approximately 10 − 20 km s^{-1} and so the object may be slowly rotating.

The global profile of the satellite galaxy from the full resolution data is shown in the right plot of Figure 2-20. By fitting a Gaussian to the curve, an estimate of the object's dynamical mass can be found by using the equation

$$M = v_{W_{20}}^2 R/G \tag{2.14}$$

where W_{20} is the 20% half width of the fitted Gaussian profile and R is the radius. The mean of the fit is 855.8 km s^{-1} and the full width at 20% is 20.2 ± 1.3 km s^{-1}. The velocity has been corrected for instrumental broadening and inclination effects estimated from the axial ratio. Using $R = 1.4$ kpc as the upper limit value, the total mass of the companion galaxy is calculated to be about 1.3×10^8 M$_\odot$ or 2.4% of the H I content of NGC 3359.

The dispersion of the Gaussian fit is 10.0 ± 0.3 km s^{-1} that is the typical velocity dispersion seen in disk galaxies (Tully & Fouqué 1985). Hence, it is possible that the observed global profile may not be indicative of ordered motions within the satellite. If the system is assumed to have a circular disk, its inclination must be close to 80°, based on the determined major and minor axes of the core. In order for the velocity dispersion to agree with the observed profile, the object would need to be inclined at less than 30°

from the line-of-sight. Therefore, the estimated total mass from Equation 2.14 gives the upper bound for the total mass of the satellite while the lower bound can be constrained by the H I mass determined from the core size.

2.6 Summary

To summarize this section, I conclude that the H I distribution within the galaxy is quite symmetric on the global scale although there is slightly more gas in the southern edge of the main disk. This extra material is reflected in left peak of the 21 cm line profile of the galaxy being slightly higher than the right by ~ 30 mJy. The nature of the H I gas is clumpy in nature, some of the features are smaller than the full resolution beam size of 0.8 × 0.8 kpc^2. This is not unexpected as most of this particular species of hydrogen tend to reside in cloud complexes. The densest regions observed are within the optical-spiral arms that form a pseudo-ring at around 3.2 kpc from the galactic center. The stellar bar region contains little atomic hydrogen gas due to the rotation of the bar sweeping the gas in toward the center. The outer arms are composed of neutral atomic hydrogen only.

The last vestige of integrated H I density resides in the western arm, some 5.25′ away from the center. In the radial profile, this last remnant has a column density value of approximately 1×10^{19} atoms cm^{-2} where, coincidentally, is the characteristic cut-off value for the galaxies observed by van Gorkom (1993). The total extent of the H I content is more than twice of R_{25}. The total H I mass of the galaxy, based on the projected 3D surface density map, is 5.6×10^{8} $M_\odot$. The total dynamical, determined from the last point of the rotation curve, is 9.9×10^{10}.

The global kinematical properties of the galaxy, summarized in Table 2, were used to derive the rotation curve of the galaxy that show two apparent maximum circular velocities. The first occurs at ~ 4 kpc from the center and is 15% smaller than the observed maximum (158 km s^{-1}) at the radius of 12.4 kpc. The extent of the rotation curve extends out to end of the northern gas arm. Its shape is smoothly varying with no truncation signature. Hence the mass distribution in the outer disk exists beyond what is observed.

The large non-circular velocity residuals (maximum 50 km s^{-1} in the disk plane) from Figure 2.46 confirm that both the bar and density waves of the galaxy are the main perturbers of the gas motions and induce the double peaks seen in the rotation curve. How much of this disturbance is contributed to the bar can be inferred from numerical simulations of gas response to the underlying (bar) potential of the galaxy. Such models have been constructed in an effort to match the irregularities that are observed in the velocity fields of the cold atomic neutral hydrogen as well as the ionised hydrogen gas

CHAPTER 3
OBSERVATIONS OF IONIZED NEUTRAL HYDROGEN

3.1 Introduction

In this chapter, the optical and near-infrared (NIR) observations of NGC 3359 will be used to analyze the stellar component of the galaxy in order to gain a deeper understanding NGC 3359 as a complete dynamical system. The discussion of the H I gas distribution and kinematics from last chapter can be used to understand of how the contents of the galaxy react to the underlying gravitational potential. However, as gas is naturally dissipative, its response to the potential will invariably differ from that of stars under certain circumstances (e.g., at resonances). Consequently, stellar distribution and kinematics merit a separate study from the gaseous component. The analysis of the stellar kinematics will be deferred to Chapter 4 as multiple long slit spectroscopy for the galaxy is not available. Such observations are greatly limited by three factors: the weak stellar absorption lines, the need to use high spectral resolution to obtain accurate line-of-sight velocities (that further weakens the signal-to-noise ratio), and the inherently low surface brightness of galaxies. Therefore, an indirect theoretical study of stellar orbits will be used instead to probe the kinematics of the stars within NGC 3359. However, recent developments of Integral Field Spectrograph instruments such as SAURON (Bacon et al. 2001) offer near-future hope for acquiring high spatial resolution stellar spectrograms of galaxies in a relatively short observing time.

The goal of this chapter is, then, to analyze the stars and H II gas of the galaxy. Assessing the optical and NIR broadband images immediately reveals one advantage in comparison to the radio data: spatial resolution. For NGC 3359, this factor is about one order of magnitude and so the images, especially within the central region of the galaxy, can be studied in great detail. Some general but important subjects such as (a) the identification and analysis of the the structural components of the galaxy, (b) the distribution of the stellar population as well as star formation, (c) the role of dust lanes

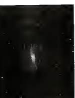

Figure 3 1 Three-color picture of NGC 3359 The image was made by combining together the U R and I images taken by the Isaac Newton Telescope

and (d) the check for consistency/similarity between the photometric and kinematic properties (derived from H I) are resolved by this investigation

The outline of this chapter is as follows in Section 2 the optical and NIR data are presented The morphology of the galaxy based on the data is also discussed Section 3 presents and discusses the color indices of the galaxy The photometric properties for each filter are obtained in Section 4 For Section 5 the Fabry Perot interferometry observations of the H II regions within NGC 3359 are presented and investigated Finally the findings of this chapter are summarized in Section 6

3 2 The Broadband Data

All but one of the broadband images presented in this chapter were obtained from the Instituto de Astrofísica de Canarias (IAC) Canary Islands Spain They have been generously provided by Dr John Beckman of the Institute The Spanish data consist of the U R and I-band images plus observations of the galactic H II regions centered around the Hα Balmer emission line The Hα observations include a broadband image and the Fabry Perot interferometer data cube The latter will be used primarily as a

Table 3-1. Observing log for the optical and NIR data of NGC 3359

Filter	Instrument	T_{exp} (s)	Date	Observers
U	PF TEK3	1800	02/13/96	Prieto, Gottesman, & Beckman
R	PF TEK3	1800	02/12/96	Prieto, Gottesman, Beckman, & Lourenso
I	PF TEK3	1800	02/12/96	Prieto, Gottesman, Beckman, & Lourenso
Hα	PF TEK3	1800	02/11/96	Cepa, Prieto, Gottesman, Beckman, & L
Hα	TAURUS	1800	03/31/96	Rozas & Sempere
K	FLAMINGOS	35	03/26/03	McKenzie, Ferreira, & Rashkind

diagnostic tool to investigate the kinematics of the ionized hydrogen gas around star formation and high compression/shock areas. The discussion of these data and results, as mentioned, will be given in Section 5. Two full nights of observations were required to obtain the data at the Isaac Newton Telescope (INT) in February 1996. The images were acquired as part of the BARS international time project of the Canary Island Observatories. The only image of NGC 3359 not originating from the IAC was taken this year at the Kitt Peak National Observatory (KPNO) in Arizona. The filters, instrument, exposure times (T_{exp}), exact dates, and observers involved in the data acquisition process are listed in Table 3-1.

3.2.1 Stellar Images

Figures 3-2 to 3-4 show the U (360 nm), R (659 nm), and I (840 nm) images of NGC 3359 respectively. As these images were pre-processed and calibrated at the IAC and have been thoroughly described in Rozas et al. (2000, hereafter RZB), only a general overview of the reduction procedure will be given here. The final images that are shown were processed through standard data reduction routines for optical images: the raw data were first bias and sky subtracted, then corrected for flat-field and cosmic ray effects. Standard stars of known magnitudes were used for the flux calibration. Astrometry was performed by fitting two-dimensional Gaussian to field stars common to every image. A positional accuracy of better than 0.5′ was achieved. The pixel scales of the three images are the same, 0.59″ per pixel. Similarly, the field of view for each image is roughly a 10′ square.

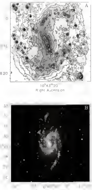

Figure 3-3 U band grayscale and contour maps of the disk of the galaxy. A) Contours are from 19.1 to 23.5 in steps of 0.4 mag arcsec^{-2}. B) The U band image of NGC 3359. The range of magnitude values shown is from 19 to 25 mag arcsec^{-2}.

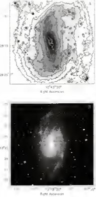
A
Declination
63°29'10"
29'20"
10h43m20s
Right Ascension
B
Declination
63°2
28
10h43m20s
Right Ascension

Figure 3.5: R band grayscale and contour maps of the disk of the galaxy. A) Contours are from 18.5 to 22.5 in steps of 0.5 mag arcsec^{-2}. B) The R band image of NGC 3359. The range of magnitude values shown is from 18.5 to 25 mag arcsec^{-2}.

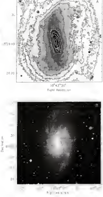
A
30
28 20
10h43m20s
Right Ascension
B
Declination
30
20

Figure 3-4 I-band grayscale and contour maps of the disk of the galaxy A) Contours are from 18 2 to 22 2 in steps of 0 4 mag arcsec^{-2} B) The I band image of NGC 3359 The range of magnitude values shown is from 18 to 25 mag arcsec^{-2}

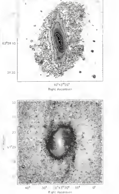
Dec
63°29'10
29 20
10h43m20s
Right Ascension
32
31
30
51°29'
28
27
40s
30s
10h43m20s
10s
0s
Right Ascension

Figure 3.5 K band grayscale and contour maps of the disk of the galaxy. A) Contours are from 15.2 to 18.8 in steps of 0.4 mag arcsec^{-2}. B) The K band image of NGC 3359. The range of magnitude values shown is from 15 to 21 mag arcsec^{-2}.

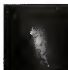

Figure 3–6 Combined three-color picture of the bar region. The image made from combining together the B, V, and R images taken by the Hubble Space Telescope.

Observations of the galaxy at 2.2 μm wavelength using a K filter were taken by the Florida Multi-object Imaging Near IR Grism Observational Spectrometer (FLAMINGOS) at the 2.1 meter telescope located at KPNO in imaging mode. Observing time the galaxy was generously provided by Drs. R. Elston and E. Lada. The primary detector of the instrument is a CCD camera that images the focal plane onto a 2,000 × 2,000 pixel HgCdTe detector. The data obtained is typically reduced by the FLAMINGOS reduction pipeline that have been largely developed by Mr. Carlos Roman and Ms. Joanna Levine. Due to the large amounts of information that are acquired each night by the instrument, such an automated process is warranted.

For NGC 3359, a set of 22 dithered images, each of 35-second exposure time were gathered and combined to produce the initial intensity image. The superscript `crunchflamingos` of the pipeline was used to correct for non linearity in the field and to remove the dark current as well as the sky noise contribution from the image. The initial reduced image, produced by the script `smoothflamingos`, is a resampled map that has all the bad pixels removed and contains geometrical distortion correction. Photometry and astrometry of the image are obtained by using the package `PINKPACK`. The guide stars used to perform both tasks were obtained from the 2MASS catalog. Figure 3-5 shows the final, reduced K image from the pipeline. The pixel scale and field of view is 0.3″ per pixel and 20′ × 20′ respectively. The determined FWHM of the point spread function (PSF) is 2.9″ and the precision of the astrometry is better than 0.2″.

Numerous blue regions seen through the U filter highlight the star formation (SF) areas that populate the galactic bar and spiral arms. Only a certain number of intense star formation areas can still be seen in the redder images. But in general, the light distribution from the galaxy is smoother at longer wavelengths, owing to the older and cooler stars that populate the entire galaxy. The asymmetric spiral arms contain most of the SF regions of NGC 3359. The western arm starts from the northern bar end and extends southward, finally ending at approximately 200″ (10.7 kpc) away from the galactic center. This arm contains some of the brightest Hα emission areas and is brighter than than its counterpart. The eastern arm breaks into the arms spurs shortly after it has passed the kinematical minor axis of the galaxy (PA = 81°). The presence of these fragments define the multiple-arm morphology (class 5) formulated by Elmegreen (1985). Within the bar there appears to be a core that is veiled by dust. This makes a definitive visual identification difficult even at the NIR wavelengths. Isophotal analysis of the surface brightness (Section 3.4) offers a better techniques of searching for structures in the centers of galaxies.

The most prominent and obvious feature of the system is the bar. The length of the structure is about 86″ in the plane of the sky or ~ 100″ (5.4 kpc) deprojected. This value was derived by Aguerri et al. (1998) from matching a corresponding increase in the odd Fourier components of the light distribution with a local peak of their B-I profile. The width of the bar is approximately 30″ or 1.6 kpc in size. The average position angle of the bar is 12°. A closer inspection of the isophotes in the U and I images reveals a slight asymmetry for several of the bar isophotes. For example, the U-band 21.5 and 21.8 mag arcsec^{-2} contours and the R band 20.8 and 21.3 mag arcsec^{-2} contours extend farther out in the east than the west. This is more likely caused by observational effects, specifically dust extinction, as stellar orbits are not expected to display such asymmetric pattern with respect to the center of the potential. Being much less affect by dust, it can be seen that the K-band isophotes are much more regular and symmetric.

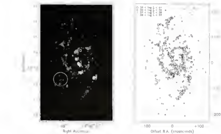

Figure 3-7 Hα broadband image of NGC 3353 highlighting the various H II regions within the galaxy. A) The ten brightest star formation zones, starting with the brightest at #1, are labeled. See text for explanation of the largest circle ("x"). B) The schematic diagram of the intensity of each H II region. The size of the circles correlate proportionally with the luminosity values in units of erg s^{-1} given in the top left of the panel (after RZB)

Figure 3-6, like Figure 3-1, is a combined three-color image of the U, R, and I data. This color image is the best data available that shows the dusty environment of the bar zone that cannot be seen easily in the other images (including Figure 3-1). The distribution and location of dust between the southern and northern halves of the bar are different. The features are somewhat easier to identify in the south. Two dust lanes that start near the southern end of the bar and curve around the major axis of the bar connect with each other near the middle of the galaxy. A pair of short dust lanes appears to originate from the connecting point and run through the western side of the galactic center, obscuring part of the light emitted from the nuclear region. As a result, the isophotes from the area have a tear-shaped pattern (Figures 3-2 to 3-4). Toward the northern part of the bar, dust is not as conspicuous although large filaments exist near the northwestern end. The existence of the interstellar grains at the ends of the bar is probably related to the orbital structure of the gas streamline within the vicinity. The nature of such gas flow is explored in Chapter 5.

3.2.2 H II Observations

The non-stellar broadband image of NGC 3359 was observed in the Balmer Hα line. The emission line originates from ionized atomic hydrogen (H II) regions around hot stars, typically of classes O and B on the Hertzsprung-Russell diagram. Within this volume (the Strömgren sphere), the hydrogen gas is heated up by ultraviolet radiation to temperatures around 7 000 K to 14 000 K. The observed Balmer lines are produced by hydrogen atoms that cascade down to the ground state following electron capture (i.e., H II + e⁻).

Observations of the Hα line from the galaxy were obtained on February 12, 1996 under photometric conditions using the TeK 7 CCD detector with an exposure time of 1,800 seconds. The filters were centered around the 659.6 and 668.6 nm respectively. The displacement of the second filter and the bandpass of each filter (4.4 nm) allowed for accurate removal of the continuum field. Similar standard reduction routines (Rozas et al. 1996, RZB) like those used for the U, R, and I images were used. Only the continuum subtraction process, performed before the astrometry stage, separates the two reduction procedures. The final reduced image has a pixel scale of 0.58″ per pixel and a field of view near $10' \times 10'$ in size The resolution of the images is 1″ based on the PSF measured in the final images (RZB)

Galactic emission in Hα for many galaxies have been investigated by the IAC group headed by Dr J E Beckman In RZB the Hα photometric properties of NGC 3359 were studied in detail In the paper they reported the Hα scale length to be 2 4 ± 0 2 kpc or about 75% of the H I scale length In addition they constructed the H II region catalog of NGC 3359 in that the positions and luminosities of individual SF regions were determined The ten brightest from the catalog are emphasized in Figure 3-7A The graph also reveals that the bar contains three of the most intense H II regions of the galaxy

The final continuum-free Hα image of NGC 3359 (Figure 3 7) demonstrates that the distribution of the SF regions can be divided into the two zones, the bar and the spiral arms The bar estimated to be 2.9′ (9 kpc) in deprojected length (RZB) contributes approximately 17% of the total observed flux (Martin & Roy 1995) Although there appears to be no nuclear activity present the center is surrounded by several bright H II regions to the northeast and southwest of the bar In the galactic disk the H II regions are distributed along the northern arm spurs as well as the southern arm Closer to the center the eastern arm shows a slight "overshoot" past the southern bar end to that it attaches Combined with the winding arms the overshoot forms an annulus analogous to the H I ring seen in the last chapter It is within this ring-like structure that most of the SF zones of the galaxy are located However several strong sources also exist in both arms that are not part of the ring Lastly a moderately intense region located 81″ (4 3 kpc) southeast of the galactic center also exists but does not seem to associated with any galactic structure (the x circle of Figure 3-7A)

3 3 Color Index Maps

The stellar color distribution of NGC 3359 can be inferred from Figures 3-8 to 3-12 The images are difference maps obtained after subtracting two different color images Due to the pixel scale difference between the K image and the Spanish data the task `HGEOM` in AIPS was used to transform the former to match those from the IAC in scale resolution and orientation. No adjustment for seeing was required as all of the data have similar values.

Like the Hα image, the SF regions are prominently displayed in the U-I color index map although the brightest H II regions residing within the bar are not the bluest (the mean value is 0.3) because of the extinction of light caused by the dust located around the central region. The spiral arms are easy to distinguish by their bluer surface color as compared to the underlying disk; again, the southern arm is brighter than the northern arm spurs owing to the presence of more luminous and extended SF regions in the former. Magnitude differences between 0.5 to -0.9 around the H II regions can be seen in the U-I map, with the greatest difference occurring along the arms where the dust has a smaller optical depth. Broad dust lanes lying on the northwestern side of the bar are displayed unambiguously in the index map. The U-I color difference in that area typically has values of +2.1. The southern dust lanes are difficult to depict in the image but are again viewable in the U-K color index. As expected, the color variations between the U and R data are not as large as the U-I color index. The R filter, although designed to observe redder, cooler stars, is still sensitive to the Hα continuum flux from star forming zones. In addition, dust extinction is still significant for the wavelength range covered by the filter. And although the R and I filters are closer in wavelength, the effects of star formation and dust are still considerable at these wavelengths. The R-I image, although fairly smooth overall, shows the contribution of both effects. In the northern part of the bar, the western dust lane is clearly seen to cross the entire width of the bar and ending on the eastern side in a large patch of dust that shroud the most intense H II region of the galaxy. The R-I colors range from 0.5 to 0.6 in this zone while diametrically opposite, the value range is 0.35 to 0.45. The best illustration of the dust seen in the previous figures comes from the U-K color index map (Figure 3.11). Both the northern and southern dust lanes are clearly enhanced as the reddest features of the image; the bright central SF regions appear the bluest, as expected. It can also be seen in the figure that light from central region is heavily reddened.

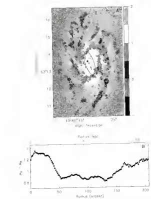

Figure 3-8 The U–R color index map of NGC 3359. A) The black oval denotes the dimensions and orientation of the bar. B) Azimuthally averaged values of the index map as determined by fitting elliptical annuli along the major axis of the disk ($\phi = -10°$).

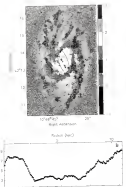

Figure 3-9 The U-I color index map of NGC 3359. A) The black oval denotes the dimensions and orientation of the bar. B) Azimuthally averaged values of the index map.

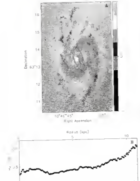

Figure 3–10 The R I color index map of NGC 3359 A) The black oval denotes the dimensions and orientation of the bar B) Azimuthally averaged values of the index map

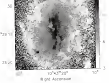

Figure 3-11 The U-K color difference map of the bar region

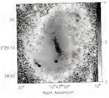

Figure 3-12 The I-K color difference map of the bar region

The NIR color difference (I-K) map offers a better diagnostic probe of the dust distribution within NGC 3359. At these wavelengths light contribution should predominantly originate from older stars in the galaxy although the contributions from young supergiant K stars cannot be entirely discounted (Rix & Rieke 1993; Patsis et al. 2001). Nonetheless, the I and K images are simply less sensitive to the presence of young stars. At 2.2 μm, the K-band light will also contain less dust obscuration than the I-band at 0.84 μm. In Figure 3-12, the color index of the two IR images proves both points: (1) the nucleus of the galaxy is heavily reddened and (2) no blue H II regions are visible. The dust distribution is also quite symmetric in the image with the average value of the interbar region being 2.6. A comparison between the U-K and I-K indices indicate that the obscuration of light is at maximum in the central region of the galaxy.

The lower bottom plots of the color indices show the azimuthally-averaged radial profiles of the images (using the position angle and inclination values derived from Section 3.4). It is clear that the bar is reddish in color despite the string of SF regions within it; the average values of the color contrast within the majority of the bar for the two figures are 1.28 and 1.78 in the U-R and U-I data respectively. Between the bar ends and the outer extent of the pseudo-ring structure where most of the H II regions reside, the difference shifts markedly to more negative (bluer) values as an abundant region of SF areas are found here. Further out into the outer disk, the region reddens once more. The average color distribution for the R and I images appear to be similar within the inner disk.

3.4 Photometric Properties

In this section, the broadband images are initially used to determine the major axis position angle (ϕ) and axial ratio (ellipticity, ϵ) of the photometric disk (and bar). These properties were derived by analyzing the isophotal contours of each image and are useful for investigating the structures within the galaxy. The results are then used to analyze the radial profiles and disk scale lengths of the galaxy.

3.4.1 Position Angle and Ellipticity of the Disk

As a check for consistency with the kinematical results that were derived for the H I observations of NGC 3359, the shape and position angle of the disk for the galaxy were determined. However, foreground star subtraction was required to limit the light contribution to only that of the galaxy. This was done by masking out the pixels of the offending stars with a variable size circular aperture and replacing them by values determined from a second-order interpolation of the pixels in the surrounding annulus. The task `imedit` of the Image Reduction Analysis Facility (IRAF[1]) program was used to serve this purpose. Next, the "smooth" images were used as input files for the standard IRAF isophotal analysis program `ellipse`[2]. The task, as described by Jedrzejewski (1987), fits elliptical isophotes to images and works by performing least-squares iterative corrections to the geometrical parameters of the fitted ellipses. Consequently, the program produces solutions (i.e. the center coordinate (x_0, y_0), ellipticity, position angle and semimajor axis a) to each fitted isophote. For a more thorough discussion of the process, please see the cited article or the IRAF help page.

Results from using `ellipse` on the images are shown in Figure 3-13. During the run, the photometric center was held constant while the position angle and ellipticity parameters of the individual ellipse were allowed to vary. Inaccurate positions of the center were found if the values were not fixed. That is, certain ellipses ended up being centered around the spiral arms rather than the galactic nucleus. The spacings between each fitted isophote was set to 1.5″ or the resolution of the images.

The top diagram of Figure 3-13 demonstrates that the bar of the galaxy is quite elongated along its major axis, the average (weighted) mean value ranging in between 0.6 to 0.8 for all observed passbands. The finding is consistent with Duval & Monnet (1985) who found that late-type galaxies have more elliptical rather than boxy-shaped bars (i.e. axial ratios between 0.1 to 0.3) like that of early-type galaxies (Ohta et al. 1990). Slightly beyond the ends of the bar at 43″ (Aguerri et al. 1998), the isophotes become

---

[1] IRAF is written and supported by the IRAF programming group at the National Optical Astronomy Observatories (NOAO) in Tucson, Arizona. NOAO is operated by the Association of Universities for Research in Astronomy (AURA), Inc. under cooperative agreement with the National Science Foundation.

[2] This IRAF routine is part of the STSDAS external package provided and maintained by the Science Software Group at the Space Telescope Science Institute (STScI).

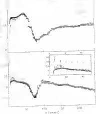

Figure 3.13 Ellipticity and position angle fits to the isophotes of the broadband images. The purple markers represent the position angle fits to the Hα bar.

very round ($\epsilon = 0.2$) near the region where the spiral arms connect with the bar. Out in the disk (beyond 150″) the isophotal ellipticities settle to a near constant value of 0.46. Assuming that the disk is intrinsically circular and $\epsilon = 1 - \cos i$ the ellipticity value implies the galaxy is inclined at an angle of 57° with respect to the sky plane.

Of more interest is the photometric position angle plot of the galaxy. At large radii the position angle of the disk drifts progressively to $\phi = -10°$ (the same value as reported by RC3 and the H I study). However the major axis of the fitted isophotes drifts away from the position angle of the disk closer to the center of the galaxy ($a < 20''$) most noticeably with the U image. This is not an uncommon occurrence as many other galaxies have shown isophotal twists within their inner regions (Elmegreen et al 1996c Jungwiert et al 1997). One plausible explanation of such a phenomenon is the existence of an inner bar. Another is the existence of a triaxial bulge/core. The dusty environment

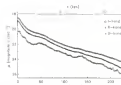

Figure 3-14 Azimuthally averaged radial profile of the U, R, and I images of NGC 3359

of the center and the high inclination of the galaxy hinders accurate identification. Nonetheless, the similarity between Figure 1 of Wozniak et al. (1995) and the shape of the ellipticity curve for NGC 3359 suggests a bulge + bar scenario.

The most curious feature of the $a - \phi$ diagram, however, lies within the bar region: there is a persistent change in ϕ values with respect to wavelength. There is a clear separation in the alignment of the bar between the U image versus the remaining passbands. In fact, the weighted mean value for each filter indicates that the bar rotates systematically from the position angle of the disk at smaller wavelengths (Figure 3-13 and also see Figure 1 of Martin 1995). The position angle of the bar, as seen with the U band, is 18°. For the the R, I and K filters, $\phi = 12°, 11°$ and $10°$ respectively. Finally, the Hα bar (as shown in the insert diagram of Fig 3-12) shows the greatest position angle shift, with $\phi = 28°$. More qualitatively, the passbands that trace out the younger stellar population (i.e., in the U and Hα wavelengths) are rotated counter-clockwise toward the east with respect to their stellar counterparts seen in the I- and K-bands. This can be explain if the gas is flowing from the bar and forming a newer generation of stars downstream. Theoretically it has been shown that there is a phase delay (up to

Table 3.2 Photometric properties of the broad band images of NGC 3359

Filter	Bar position angle (degrees)	m_0 (mag arcsec^{-2})	R_h (arcseconds)
U	17.0 ± 0.7	20.65 ± 0.06	43.8 ± 0.5
R	11.7 ± 0.6	20.11 ± 0.06	49.4 ± 0.8
I	10.9 ± 0.0	20.20 ± 0.04	60.3 ± 0.6

45°) between stellar and gas responses (Wada 1994). Hence the offset between the two bars is quite possible.

3.4.2 Surface Photometry

The azimuthally averaged surface brightness profile of NGC 3359 for the U, R, and I filters are shown in Figure 3-14. Each profile was created by dividing the respective broadband image into 1.5″-wide elliptical annuli of constant inclination and position angle ($\phi = -10°$ and $i = 57°$, as found in the last section). No internal extinction corrections have been applied to the results.

The profiles are generally typical of late-type galaxies, with redder images having smoother profiles. The undulations in the U band profile are due to the SF regions to which the filter is sensitive. In particular, the two peaks located near 50″ and 130″ are made by associations of young blue stars residing at the ends of the bar and three major star formation areas in the north and south arms. The surface brightness of the galaxy also increases in the two red filters near where the bar ends (40-50″) although it is mild compared to the U band profile.

The disk portion of the brightness profile is approximately exponential and can be described by the equation

$$m_D = m_0 \exp - \left(\frac{R}{R_h} \right) \tag{3.1}$$

where m_0 is the central surface brightness of the disk and R_h is the disk scale length. The results of the fit are given in Table 3.2.

The exponential law fit was made to the outer disk of the galaxy. That is, equation 3.1 was applied to regions beyond 135″ to avoid the strong light contribution emanating from the bar and the bright zones of H II regions within the inner disk. Such features, as noted earlier, are the causes of the local peaks and valleys that exist in the light profiles and color index maps. Elmegreen & Elmegreen (1985) reported $R_h = 82'$ for their study

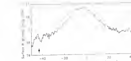

Figure 3-15 The K band surface brightness profile along the bar The arrows mark the ends of the bar and the abscissa values correspond to projected distances

of the radial profile of NGC 3359 in the I band The difference between their value and the one in Table 3-3 is caused by the different methods of radial profile extraction.

The surface brightness along the major axes of the bar as seen at 2 2 μm, is shown in Figure 3-15 Being mainly free of dust effects and H II emission, the slices show good symmetry for both sides of the bar The light distribution of the profile are consistent with those of the B- and I-band as shown in Figure 1 of Elmegreen et al (1996) All of the profiles indicate that NGC 3359 has a "flat" (the surface brightness decreases slowly) rather than an exponential (the light profile has a scale length close to that of the disk) bar

3 5 Fabry-Perot Observations

In this section the kinematics of the ionized hydrogen gas within NGC 3359 will be examined The Hα velocity field derived from the FP cube offers much better angular resolution than the H I data. Hence, the small scale structures that are seen in the velocity fields can be observed at higher resolution The immediate result shows that the kinematics of the gas contains interesting non circular components associated with the H II regions

3 5 1 Hα Data Cube

Observations of the H II gas in NGC 3359 were made by M Rozas and M Sempere on March 31, 1996. The instruments used were the TAURUS II (second generation

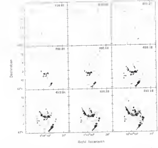

Figure 3 16 Hα channel maps of NGC 3359 The central velocity of each channel is displayed at the top right corner in units of km s^{-1} Channels 18 to 26 (of 55) are shown on this page Contour levels are plotted at (3, 10 25, 55, 115 235 375 500) ×1σ arbitrary units

TAURUS) FP instrument with an etalon spacing of 125 μm and a TEK 2 CCD detector attached at the Cassegrain focus. A narrow band ($\Delta\lambda = 15$ Å) filter centered at 6589 Å was used for order-sorting. The width of each channel (spacing between two image planes) was 0 34 Å(15 6 km s^{-1}) A total of 55 steps were required to cover the 17 23 Å wide FSR (Free Spectral Range Appendix C) The observers windowed the camera to a size of 540 × 540 pixels at 0 56″ × 0 56″ per pixel to avoid vignetting by the filter wheel, thereby producing images of 5′ × 5′ in size The exposure time for each image of the data cube was 140 seconds. The sky was photometric during the observing run and the resolution of the data was limited only by the seeing of $\sim 1.5''$

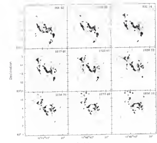

Figure 3–16 Contour map of channels 27 to 35 of the Hα data cube

After the phase and wavelength calibration of the data was performed (with the help of a CuNe calibration cube) the sky and continuum background emission were subtracted The removal of the sky was performed for each channel and the continuum was determined from a linear baseline approximation that was fitted to the line-free channels Positional astrometry was performed by using field stars and well-resolved bright H II regions from the broadband Hα image (Figure 3-7) to produce positional errors of less than 0 5″ for each plane of the cube

Figures 3-16 and 3-17 shows the inner 27 (of 55) channels and the global profile of the data cube respectively The asymmetrical distribution of the Hα emission within NGC 3359 is also shown by both figures–more emission can be seen in the southern half

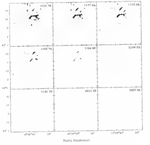

Figure 3-16 Contour map of channels 36 to 44 of the Hα data cube.

in the channel maps and the peak of the profile is located at the approaching side of the galaxy This asymmetry exists only for the Hα emission as the global profile of the 21 cm radiation is more symmetric for the same region (Figure 2 5)

3 5 2 Moment Maps

As pointed out by Rozas et al 2000b (hereafter RZB2) the initial moment maps made from the original reduced data cube contained many unacceptable noise spikes As such more data reduction was necessary before further analysis of the data could be made The method of data reduction performed in this section follows that of RZB2 The first step was to remove the continuum emission from the data cube by fitting a linear baseline approximation to the line-free channels and subtract it from the data

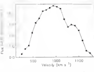

Figure 3 17 Hα global profile of NGC 3359 Units are in 10^5 arbitrary units

ul e This process not only removed the continuum but also removed some of the unusually bright single pixels that extended for several planes of the data cube These pixels were not associated with any emission regions Improvement of signal to-noise ratio was performed by using a Gaussian function to smooth the original 1 5″ data down to the lower resolutions of 5″ 10″ and 15″ cubes Next the 10″ and 15″ data cubes were used for initial removal of the noise spikes Pixels of the 10″ data cube with values below the 2 5σ limit of the 15″ data cube were blanked out The result of the process produced a 10″ conditionally transferred data cube that were mostly free of lower noise features To remove the high value noise spikes all pixels not within the Hα emitting region were blanked out This stage proved to be the longest part of the process Individual channels for both sets of data were required to be inspected interactively and one-by-one to produced the final "cleaned" cube The process just described was then applied to the 5″ and 1 5″ data to produce a set of cube that are used to analyze the kinematics of the H II gas

Figures 3-18 to 3-20 displays the final Hα moment maps constructed from the clean cubes by utilizing the moment equations shown in the last chapter All pixels that spanned less than three consecutive channels and have less than 3σ values were not excluded from the making of the moment maps

The zeroth moment map is similar to the image taken by through broadband filter (Figure 3-7) As the method of RZB2 was followed to produce the moment maps the

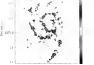

Figure 3-18 Hα integrated intensity (i e moment zero) map of NGC 3359 The units are arbitrary

intensity map also shows very good correspondence with Figure 2 of their paper Small differences between the two exist because of the minor variances in certain steps of the data reduction process (e g continuum subtraction r m s value determination and the subsequent signal acceptance range)

The most important product of the FP data cube however is its first moment The velocity field of the ionized hydrogen gas at various resolutions are shown in Figure 3-19 The 1.5″ map is difficult to interpret due to the patchy nature of the Hα emission seen at full resolution. There is more coherence in the velocity field at lower resolution (starting at 5″) with the increased sensitivity gain owing to the convolution process The best representation of the flow of H II gas can be seen at 15″ In general, the velocity field indicates that the gas is flowing circularly throughout the disk But as in the H I velocity field kinks in the Hα isovels near the spiral arms can be attributed to the streaming motions associated with spiral density perturbations The 5″ velocity field also has strong non circular effects within the inner part of the disk Bar streaming motions are quite apparent in the 15″ data as marked by some of the contour lines that run nearly parallel to the bar near the galactic center Perturbations of 30 to 50 km s^{-1} in the plane of the galaxy can be estimated from kinks in the isovels (RZ82)

High velocity dispersion of the line profiles are outlined in the second moment map (Figure 3-20). There is a strong and direct correlation between the intensity of the H II region and the surrounding velocity dispersion of the ionized gas. The ten brightest regions of Figure 3-7 have dispersion values within the range of 25 and 45 km s^{-1} (the largest occurring within the two central sources) while the average dispersion for the galaxy lies between 15 to 20 km s^{-1} as seen along the line-of-sight. RZB2 showed that the correspondence still existed after the removal of the natural line, instrumental, and thermal width contributions to the observed spectral lines. It will also be shown in section 3.5.5 that there is also a relationship between the residual velocity field, made from subtracting a circularly rotating model, and the second moment map. Because of this correlation, it is possible that the non-circular velocity components associated with the intense H II regions could very well be non-planar, expansion motions of hot gas (RZB2). That is, the gas may have radial and/or vertical motions.

3.5.3 Rotation Curve and Position-Velocity Diagrams

The rotation curve of Figure 3-21 was obtained by fitting the 5$''$ velocity field with a series of concentric, elliptical annuli. The same procedure used to extract the H I kinematical properties (Begeman 1989) was employed to determine the corresponding Hα values that are listed in Table 3-3. The results of Chapter 2 were used as the initial estimates for the parameters. The width of each ring was set to one beamwidth. Like RZB2, the lower resolution maps at 10$''$ and 15$''$ were used as guides to solve for V_{sys} and i. Only annuli larger than the radius of the bar were used to compute the inclination. The values are weighted mean results of the kinematical parameters reported in Table 3-3. The discrepancies between the last three properties of the two sets of results stem primarily from the different centers used for each analysis. Indeed, if the kinematical center found by RZB2 was used, similar values for V_{sys} and V_{max} can be found. However, the overall fit using the velocity fields derived in this research is not as good as those that are listed in the table. Therefore, the values that are shown represent the best Hα kinematical parameters for this dissertation.

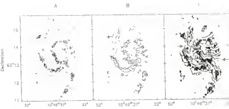

Figure 3-19 H I velocity field at three resolutions A) The 1.5″ B) 5″ and C) 15″ resolution velocity field. The arrows represent the systemic velocity $V_{sys} = 1008.9$ km s^{-1} of the galaxy

Right Ascen

Figure 3-20 Hα velocity dispersion (i.e. second moment) map of NGC 3359. The units of the color bar are km s^{-1}

Table 3-3 Hα kinematical properties of NGC 3359

Parameter	Current results	RZB2
Kinematical center (J2000.0)		
Right Ascension	$10^h\ 46^m\ 36.7^s$	$10^h\ 46^m\ 35.6^s$
Declination	63° 13' 27.0''	63° 13' 26.0''
Systemic velocity V_{sys} (km s^{-1})	1008.6 ± 0.8	1006.8 ± 0.3
Inclination i (degrees)	54°	53°
Maximum rotational velocity V_{max} (km s^{-1})	153.0 ± 0.8	162 ± 2.5

As was found in determining the H I kinematical center, if (x_0, y_0) was left as a free parameter, the position values that were determined varied dramatically at different radii and did not produce a satisfactory fit. Thus, the original value (i.e. the H I center) was used for the remaining steps of the fitting procedure. The position angle ϕ was left to vary with radius after initially fixing its value to −8° for the inner 45'' (bar) portion of the velocity field. It can be seen in the bottom plot of Figure 3-21 that ϕ varies with radius so a mean value cannot be used to fix the global position angle of the kinematical major axis as was done for the 21 cm data. The trend, as well as allowing ϕ to vary with distance, can also be observed in Figures 5 and 6 of RZB2.

The final rotation curve was derived from using the 5'' map and the estimated values in Table 3-3. Another rotation curve, at a resolution of 15'', was created in the same

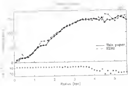

Figure 3-21 The Hα rotation curves of NGC 3359 as derived by RZB2 (dashed lines) and this dissertation (thick solid lines)

fashion but will be shown and used later to compare the Hα and H I kinematics. The graph covers approximately 85% of the H II field. Annuli fit to the region beyond the 100″ contained fewer sample points owing to the sporadic location of SF regions in the outer part of the galactic disk. This led to estimates of V_c with large errors that were considered unacceptable. These data points have been excluded subsequently. Nonetheless, the displayed plot is regular: the outer portion of the curve is fairly flat and the inner region ($r < 50''$) can be described by a solid body rotation that rises at a rate of 148 ± 2 km s^{-1} arcmin^{-1}. This value is similar to the 144 km s^{-1} arcmin^{-1} derived for the H I rotation curve and 142 km s^{-1} arcmin^{-1} of RZB2. The majority of the local peaks that exist in the rotation curve coincide with annuli that contained bright SF regions within them. For example, the local peak near $25''$ corresponds with the two brightest H II regions that are located just NE and SW of the galactic center. The minor differences between the derived kinematical parameters for this paper and RZB2 are reflected by the small variations (average difference = ± 5.7 km s^{-1}) between the two rotation curves in Figure 3-21.

As a check for the consistency and credibility of the derived rotation curve, the results have been plotted atop the (kinematical) major axis position velocity diagram

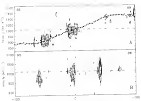

Figure 3-22 Position-velocity diagrams of the major and minor axes. A) PV plot of the major axis. The rotation curve is superposed as points. B) PV plot of the minor axis. The contour levels, in arbitrary units, are at (2, 3, 5, 7, 11, and 15) ×1σ

(Figure 3-22). The good correspondence between the two plots indicates the quality of the kinematical properties used to derive the rotation curve is reasonable. Structures that exist along the line-of-node, as labeled in the figure, are the southeastern arm (a), the bar and galactic center (b), a thin region of the western arm (c), and a section the northern arm spurs (d). The western side of the minor axis PV diagram is regular with the centers of the emission centered around the systemic velocity V_s. But the section of the eastern arm that lies on the minor axis has a line-of-sight offset that has been blueshifted by about 40 km s^{-1} from V_s. The position of this offset coincides with point a of the minor axis PV diagram of the 21-cm data (Figure 2-18). This suggests that both species of hydrogen gas under study are flowing inward toward the nucleus along the kinematic minor axis.

3.5.4 Residual Map

The kinematical property results from Table 3-3 and the fitted values of V_c from the 5° rotation curve were used to create an axisymmetric Hα model velocity field of NGC

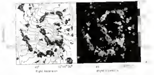

Figure 3 23 A) Isovelocity contours of the axisymmetric velocity field (from 850 km s^{-1} to 1150 km s^{-1} at every 15 km s^{-1} interval) plotted on top of the Hα moment zero map B) The 1 5" residual velocity field made from subtracting out the model from the observed velocity field Units of the color bar are in km s^{-1}

3358 The model, represented as isovels in the left panel of Figure 3-23 best resembles the 15" moment one map Strong non circular isovels within the region between the bar and the arms can be seen, much like the observed (15") velocity field The synthetic map also shows streaming motions near the spiral arms of the inner disk.

To study the non circular component of the H II gas flow within the galaxy in detail, a velocity residual map was made by subtracting the model from the 1 5" first moment image The residuals values in the right panel of Figure 3-23 have an overall average of 1 km s^{-1} but with values as large as ±20 km s^{-1} Also several of the largest differences are located near the brightest H II regions The strongest peaks occur within the bar region as can be seen by the apparent gradient within the structure in the figure As alluded to earlier in Section 3 5 3 these regions also show high velocity dispersion values and could indicate motions of expansion (either radially and/or vertically) produced by the O and B stellar members of active star formation regions Such motions have been observed in dynamical models (Zurita 2001)

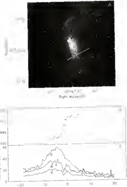

Figure 3 24 Velocity and isophotal slices through a dust lane A) HST R band image with position of the slice (Section 3 6) superposed B) Radial velocity profile of the slice, C) Intensity profiles made from cuts through the V R , and K band images The gray bars denote the location of the major dust lane The R and V intensity values have been scaled up by a factor of two to emphasize the feature

3.6 The Bar Region

The bar of NGC 3359 is believed to be in the development stage (Martin & Roy 1995). From dynamical studies of Friedli & Benz (1993) and Friedli et al. (1994), a vigorous flow of gas is expected around the young bar. The flowlines of the gas are highly elongated and produce nonaxisymmetric streaming motions that are reflected by the twisted isovelocity contour lines that are seen in the velocity fields. Thus, it is expected that the oval circulation of the gas will contribute a major non circular component to the observed velocity field. The robust flow of gas within the bar play a major role in creating the dust lanes that are seen typically in barred galaxies.

In NGC 3359, the northern dust lanes are rather ambiguous. The dust lanes in the south, on the other hand, are fairly prominent. These characteristic features of barred galaxies, based on hydrodynamical studies, are locales of shocks. These shocks occur when high velocity gas flowing along the bar potential in toward the center meets the slower, outward moving gas as it climbs out of the potential. Consequently, velocity jumps are expected to exist at the dust lanes. To determine whether such phenomena can be detected in NGC 3359, line profiles were made by taking a sample slice across the bar in the V, R, K, and velocity field maps. As plotted in Figure 3-24B, a jump in velocity is indeed present in the slice profile. The dust lane that exist just left of the slice center show a radial velocity change of only about 40 km s^{-1} (≈ 50 km s^{-1} deprojected) within 3″. This velocity gradient is relatively moderate and the shock is fairly strong.

An additional cut along the bar, made along the major axis, was made to study the flow of the H II gas inside the structure. Figure 3-25 shows the PV diagram of the slice. The rotation curve of the galaxy, projected to the bar position, is also plotted atop the intensity contours. Comparison of the two show that the H II regions within the bar, especially those SW of the center, have large non-circular velocity components associated with them. The largest difference is approximately 40 km s^{-1} as seen along the line of sight. These variations are consistent with the velocity gradient that are present in the residual map as shown in the previous section and provide another evidence of the strong nonaxisymmetric kinematics within the bar region.

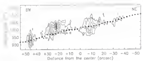

Figure 3 25 Position velocity diagram of the bar major axis The contour levels are at (2 5 6 0 9 0 13 0 17 0 21 0 25 0 35 0) ×1σ arbitrary units

3 7 Comparisons of H I and H II Kinematics

With the kinematics of each specie of gas analyzed a comparison of the two individual studies can be made However the original spectral and spatial resolutions of both data sets differ and so preliminary corrections were required to make them comparable to one another Adjustment to compensate for the larger FP data velocity resolution of 15 6 km s^{-1} was made by smoothing the spectral axis of the 15″ H I cube with a Hanning function The resulting smoothed first moment map has a velocity resolution of 16 6 km s^{-1} In addition the Hα velocity field has to be convolved to a spatial resolution that is comparable to that of the H I

3 7 1 Rotation Curves

The rotation curves of both data sets are plotted in Figure 3-26 There is very good correspondence of the two curves for the 35″ to 83″ (∼ 1 8 kpc – 4 4 kpc) region The average and maximum differences between the circular speed of the gases within this annulus are 1 9 and 4 7 km s^{-1} respectively Further out the H I curve begins its decline to a minimum V_c at 125″ as observed in the last chapter The H II gas however does not follow Rather the last two credible data points increase in value so that the difference between the two curves become as large as 20km s^{-1} This difference appears to be real and not an effect of the convolution process Rotation curves at higher resolution show the same dichotomy albeit with a slightly difference in amplitude Figure 6 of RZB2 also show a similar variation between the two graphs It is unclear as

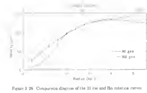

Figure 3.26 Comparison diagram of the 21 cm and Hα rotation curves

to what the cause of the difference may be. However, part of it is due to the different inclination angles that were used to obtain the curves (Table 3-3). It is also possible that the streaming motions may be stronger for the H II gas.

In toward the center of the galaxy, the circular flow of H I is faster than the H II gas by an average of about 20 km s^{-1}. As most of the velocity information for the FP data comes from the H II regions within the bar and are azimuthally averaged out, it is likely that the kinematics of the ionized hydrogen contain more information about the velocity fields associated with the star formation and stellar winds present in the bar (Jörsäter & van Moorsel 1995, Laine 1996) as well as (elliptical) bar streaming motion. This point is emphasized in the previous discussions of the velocity dispersion and residual maps. In addition, the H I rotation curve contains more sample points owing to the broader extent of the gas and therefore is not limited to and affected only by the SF regions or bar streaming motions. The effect of beam smearing, as described in the previous chapter made by convolving the original data, also contributes to the difference.

3.7.2 Velocity Fields

The H I-Hα residual map of Figure 3.27 is a direct comparison study of the two velocity fields. The intensity map of the H II gas at full resolution is also plotted in the figure to emphasize the convolution effects. The residual map demonstrates that the flow

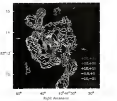

Figure 3 27 Color-coded isovels of the H I-Hα residual velocity field The background image is the 1 5″ Hα intensity map The plotted ellipse denotes the region in which the circular velocities of the H I gas is greater than H II (Figure 3-26) The arrows indicate the minor axis of the galaxy Contour units are in km s^{-1}

of both gases are in agreement for most of the Hα emitting region The mean velocity difference between the two maps is less than 2 km s^{-1} with an rms dispersion of about 5 km s^{-1} Most of the large differences (i e greater than 10 km s^{-1}) can be attributed to the smoothing applied as these locations coincide with the edges of the Hα velocity field And although convolution effects contribute to the largest peaks within the gradient (31 to 42 km s^{-1}) of the central region of the bar real kinematical differences between the cold and ionized gases are also present As seen in Figure 3-26, the rotation curve of the 21 cm data is greater in this area (marked by the oval in Figure 3-27) the radial velocity of the H I gas should therefore be larger than that of the H II for the zones above the minor axis of the galaxy Conversely H I radial velocities will be smaller than those of H II for the regions below the minor axis Indeed this is precisely what occurs in the residual map

3.8 Summary

In this chapter, many of the photometric properties of NGC 3359 have been investigated. The major feature of the galaxy, the bar, is found to be quite red in color despite having many bright giant H II regions located along its major axis (although none exist in the nucleus). The dust in the bar region contributes to observed colors. The K band light profile of the bar major axis was found to be flat and in agreement with Elmegreen et al. (1996) (although Elmegreen & Elmegreen had originally classified the light from the bar as exponentially decreasing in 1985). In the same papers, they have also conjectured that early types spirals have flat bars and so NGC 3359 is clearly at odds with this predicted trend. However, it is unclear how well established this relationship between bar light profile and the Hubble classification is. Coincidentally, another late-type galaxy that also has a flat bar is NGC 7479 and both galaxies have been suggested to have young bars–the bar of NGC 7479 is estimated to be approximately 0.5 Gyr (Martin 1995). It is therefore possible that the shape of the light profiles of the two galaxies are affected by their developing bars.

The spiral arms are the bluest component of the galaxy owing to the fact that (a) the majority of the galactic H II regions reside within them and (b) there is less dust obscuration. The color index at large radii (i.e., beyond ~ 150″) is reddish that suggests that the predominant occupants of the outer disk are older stars.

The position angle of the photometric disk tends toward the kinematical value of −10°and the ellipticity of the outer disk gives an inclination value of 57°. Both values are consistent with the kinematical analysis of the H I and Hα data. An analysis of the passbands, as reported in Table 3-2, suggests a linear increase of the disk scale length as a function of wavelength of observation. This relationship and the magnitude of the reddening of the outer disk is contrary from the study of 86 spirals made by de Jong (1996) and Graham (2003). Based on their published results, the majority of the objects in their sample have decreasing disk scale lengths at larger wavelengths. de Jong (1996) also found that the galaxies became bluer with increasing radius and that the increasing scale lengths point to the inner regions being older than the outer. NGC 3359 appears to contradict this trend due to the presence and effects of the bar. Not only is the bar forming, but the structure itself is funneling in gas to form newer bluer stars as well. In addition, the majority of the SF zones, as seen in the Section 3.2.2, lie in the inner to middle part of the disk. Thus, the outer disk of the galaxy lacks younger stars and consequently is redder.

The Fabry Perot observations of the Hα emission from ionized hydrogen is an additional and vital source for studying the gas kinematics within NGC 3359. The models of the velocity field show strong non-circular effects caused by spiral density waves and bar streaming motions around the arms and central regions of the galaxy respectively. The deviations from circular motion are as high as 45 km s^{-1} (in the plane of the sky). The derived systemic velocity (1008.6 km s^{-1}) and inclination (54°) of the Hα disk are in agreement with the 21-cm data.

The residual velocity field shows non circular effects indicative of streaming motions around the bar as well as the arms. There is an established gradient (from about 35 to −15 km s^{-1}) within the bar, as shown in Figure 3-23. Furthermore, some of the most intense SF regions with large residuals also have high velocity dispersions. Such peaks could be caused not only by streaming effects but also by vertical motions of expansion by the ionized gas around the hot stars. Recent investigations of several H II regions of NGC 3359 by Relano et al. (2003) have led them to suggest that a significant fraction of the regions have expanding shells that are driven by either stellar winds or gas acceleration caused by stellar radiation (winds).

Within the bar, velocity jumps can be seen near the dust lanes. As discussed in Section 3.6, these features are indicative of shocks at their locations. The highest velocity jump that was able to be determined from taking slices across the width of the bar yielded values of only 40 km s^{-1} that indicates that the shocks are moderately strong. The dust features themselves are rather difficult to identify in most of the optical images (except for the combine three color HST image) and the redder color index map. The interstellar grains are mostly concentrated near the ends of the bar in patches although there is substantial obscuration of light close to the galactic center. The term "dust lane" has been used rather freely in this chapter as the bar does not have the typical offset curved dust lanes seen in many other late-type galaxies. The morphology of the dust distribution in the southern half of the bar is easier to depict from Figures 3-6 and 3-11 than the northern portion. These features have not been discussed much in past investigations of the galaxy (Ball 1986 and Hunter et al. 1990 saw the dust patches at the ends of the bar only). This difficulty in identifying the dust lanes should be kept in mind when the analysis of the gas models is discussed in Chapter 5.

Finally, a comparison study between the H I and Hα kinematics have shown that both species of hydrogen have similar motions throughout most of the galaxy. The largest differences between the two gases are at the bar region. For the first 30° of the area, the H I gas is moving faster than the H II as was shown in the last section. Based on these analyses, it appears that the ionised gas is affected to a greater degree by the local velocity fields of the H II regions that appear to have not only the usual circular velocity component but also radial and possibly vertical motions.

CHAPTER 4
STELLAR DYNAMICS

4.1 Introduction

While the observation of galaxies give us a wealth of detail about the objects that populate them their morphologies and internal dynamics can (and at times only) be more fully understood through theoretical considerations In light of this, Chapters 4 and 5 will be based on numerical simulations in that the basic properties of stellar orbits and gas flow will be modeled Such investigations will be useful in explaining the distribution of stellar and gas densities that are generally regulated by the motions of the stars and the gases that follow their orbits A brief excursion into the analysis of stellar orbits within the plane of NGC 3359 is made in this chapter

The morphological features that stars are associated with can often be related to their orbital structures Good knowledge of the stellar orbits and their stability in the underlying potential of the galaxy gives valuable information for the morphology and evolution of the system The study of stellar orbits is therefore not only an investigation of the dynamics of the current system but it also offers a glimpse of the possible future of the galaxy

Interesting non circular orbits are created with the introduction of the barred perturbation Many of the important theoretical considerations of the orbital structures within barred galaxies stem from the works of G Contopoulos One of the more notable results of his studies is that bars cannot extend beyond corotation and end close to it. In Contopoulos (1980), it was shown that the orbits that exist outside corotation were aligned anti-parallel with the bar and therefore provide no structure support Yet another important result from the study of stellar orbits in a barred galaxy comes from Athanassoula (1992a) she suggested that the ratio of the corotation radius to the bar radius should be within 1 2 ± 0.2 It will be shown in this chapter that the orbital structures within NGC 3359 conform to the both notions

The outline of this chapter is as follows. Section 4.2 is a small overview of the theory of dynamics of a disk system. Namely, the definition of epicyclic frequency, effective potential, and resonances are introduced. The importance of the latter phenomenon is also discussed. The angular rotation rates and the method to determine the resonances are also presented in this section. The method of extracting the gravitational potential of NGC 3359 is explained in Section 4.3. In Section 4.4, the method to finding the periodic orbits and their stability is formulated and then used to find the families of orbits that support the bar with two different models. The first consists of only the axisymmetric component of the overall potential while the second utilizes the full potential as derived from Section 4.3. The last section is a summary of the results found in this chapter.

4.2 Fundamental Concepts

To study properly the orbits of stars that are under the influence of a barred potential, some basic and fundamental concepts need to be introduced and will be presented in this section. Further details can be found in Binney & Tremaine (1987) and in Contopoulos (2002).

Assuming that the reference frame of study is corotating with the bar, the equation of motion is given by

$$\ddot{\mathbf{r}} = \nabla\Phi - 2(\mathbf{\Omega}_b \times \dot{\mathbf{r}}) - \mathbf{\Omega}_b \times (\mathbf{\Omega}_b \times \mathbf{r}) \tag{4.1}$$

where $\mathbf{\Omega}_b = \Omega_b\hat{\mathbf{z}}$ is the angular frequency of the rotating system (and the bar). The second and third terms of the right side represent the Coriolis and centrifugal forces respectively. The "energy" of a particle in the rotating frame can be expressed as

$$E_J = \frac{1}{2}\dot{\mathbf{r}}^2 + \Phi - \frac{1}{2}|\mathbf{\Omega}_b \times \mathbf{r}|^2 \tag{4.2}$$

and is an integral of motion known as the Jacobian; its importance will be shown in a later section of this chapter. The last two terms of Equation 4.2 are typically called the effective potential Φ_e of the rotating frame. In the rotating frame of reference, there are five positions of Φ_e called *Lagrangian points* that are of special interest. At these locations, labeled L_1 to L_5 in Figure 4-1, the gradient of the effective potential is equal to zero. L_3 is the minimum in the center, L_1 and L_2 are saddle points in the major axis

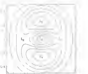

Figure 4.1 Equipotential contours of an effective potential Φ_e containing the logarithmic (bar) potential (Equation 3-77) of Binney & Tremaine 1987. The Lagrangian points are marked L_2 to L_5.

of the bar and L_4 and L_5 are the maxima along the minor axis. In general, L_4 and L_5 are stable and L_1, L_2 unstable points. The annular region defined by points L_1, L_2, L_4 and L_5 makes up the *corotation zone*. The particles within this area remain stationary in the rotating frame while appearing to travel in circular orbits when viewed from a fixed reference frame.

In the polar coordinate plane of the frame where $\Phi = \Phi(r, \varphi, z = 0)$, the radial and azimuthal components of Equation 4.1 are

$$\ddot{r} - r\dot{\varphi}^2 = -\frac{\partial\Phi}{\partial r} + 2r\dot{\varphi}\Omega_b + r\Omega_b^2 \tag{4.3}$$

$$r\ddot{\varphi} + 2\dot{r}\dot{\varphi} = -\frac{1}{r}\frac{\partial\Phi}{\partial\varphi} - 2\dot{r}\Omega_b \tag{4.4}$$

respectively. For particles that do not travel in a circular path, their orbits can be considered as consisting of small ellipses (epicycles) whose guiding centers travel circularly around the galactic center within the reference frame (as in the simple case of orbits in an axisymmetric field). For the axisymmetric potential Φ_0, the rate at which the particle executes an epicycle is called the epicyclic frequency κ and is given by

$$\kappa^2 = r_0\left(\frac{d\Omega^2}{dr}\right)_{r_0} + 4\Omega_0^2 \tag{4.5}$$

[illegible] is the circ[illegible] In other words $\Omega_0 = \Omega(r_0)$ where

$$\text{[illegible]}(r) = \frac{1}{r}\frac{d\Phi_0}{dr}$$

A moving particle in the rotating frame has two basic frequencies κ and Ω [illegible] resonance is established when the ratio

$$\kappa = \frac{n}{m}(\Omega - \Omega_b) \quad \text{[illegible]}$$

is rational. Periodic orbits at this location will have closed orbits after m revolutions about the galactic center and n radial oscillations.

For a bisymmetric perturbation like a bar, or a bisymmetric spiral as the one observed in grand-design spirals, the most important resonances are:

(1) Corotation (CR) or particle resonance, where $\Omega = \Omega_b$

(2) Inner Lindblad Resonance (ILR), where $n/m = 2/1$, and

(3) Outer Lindblad Resonance (OLR), where $n/m = -2/1$

It should be noted that, depending on the pattern speed or potential being considered, there could be one, two, or no ILR (Figure 4.2); also, another resonance of importance occurs when $n/m = 4/1$. This 4:1 resonance is frequently mentioned as the ultraharmonic resonance (UHR).

Resonances play a critical role in determining the global dynamics in a disk galaxy. They affect the stability, the orientation and the morphology of the periodic orbits in a rotating model. Starting with a particular periodic orbit, a set of such orbits, called a *family*, can be found by varying a parameter of the system (e.g., the Jacobian constant). For 2-D barred galaxy models, the major families have been found to be the so-called x_1 and x_2 families of periodic orbits (Contopoulos & Grosbøl 1989)[1]. The x_1 family has elliptical orbits along the bar and in standard fast 2-D rotating systems it is the main family supporting the bar until close to corotation (Athanassoula, 1992a; Combes

---

[1] In 3-D models of barred galaxies the role of the planar x_1 family plays a tree of 2-D and 3-D families called the "x_1-tree" (Skokos et al. 2002).

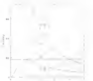

Figure 4.2 Frequency curves for a Toomre potential ($\Phi_3 = -1/\sqrt{r^2 + a^2}$) with $a = 1$. The constant pattern speed Ω_b is denoted by the horizontal line and the $\Omega - \kappa/2$ is the bottom curve. The lines are tangent to one another and produces one ILR. Two ILRs will exist if Ω_b intersects the $\Omega - \kappa/2$ at a pair of points (i.e. slower rotation). No ILR exists for a faster pattern speed. The rotation curve of the disk is given by the dotted curve.

et al. 1995; Contopoulos 1983; Contopoulos & Papayannopoulos 1980). If an ILR exist, then the x_2 family influences the dynamics at the region and has elliptical orbits perpendicular to the bar. Beyond corotation and out to the OLR, the orbits are once again perpendicular to the bar although their shapes are more circular than elongated. This is one of the main arguments in favor of the hypothesis that bars cannot extend past the CR (Contopoulos 1980).

Resonances also play an important and significant role in the study of galactic morphology. If their positions can be located within the disk, then one could claim that to a large degree, the dynamics of the system are understood. Unfortunately this task is not trivial and usually requires comparisons between the models and observational data. The extent of structures like bars and spiral arms is determined by the locations of resonances (Contopoulos 2002 and references therein). Nuclear rings like those observed in ESO 565-11 Buta et al. (1999) and NGC 3489 (Erwin & Sparke 2003) appear to be located at the ILR. Inner rings like those observed by Buta et al. (1995) are suggested to be the result of the orbital dynamics at and just beyond the UHR in barred potentials

(Patsis et al 2003) Dust lanes are predicted to change from lying on the inside to the outside of the spiral arms near the CR (Elmegreen 1998) The velocity fields of galaxies are also affected by the resonances and as such some authors like Canzian (1993) and Tremaine & Weinberg (1984) have tried to obtain their locations from kinematical information However, due to the various observational constraints and limits these resonances are not easily identified by image analysis Only a handful of galaxies have had their resonances properly obtained while the rest remain unsolved and require theoretical analysis to help resolve the structure of their morphologies

4.2.1 Derivation of the Gravitational Potential of NGC 3359

The underlying potential of the galaxy is the single most important datum for the theoretical study of the stellar and gas kinematics in NGC 3359 Information about the stellar content and its mass distribution plays the central role in determining the potential as the latter governs the gravitational field that the stars dominate The procedure that is employed here to obtain the galactic potential follows the work of Quillen et al (1994) Their Fourier transform method creates a model independent potential by convolving the surface mass density of a deprojected image with a function that is dependent on the vertical scale height

The first step of estimating the potential is to correct for inclination This was done by stretching the image along the minor axis by a factor of $1/\cos i$ so that the galaxy appeared face-on The result of performing the task (using `TRANSFORM` in GIPSY) is shown in Figure 4 3 In the program, $i = 52°$ (the disk inclination value of Chapters 2 and 3) and $\varphi = -10°$ were used as the deprojection parameter values The roundness of the outer isophotes shows that the inclination value used for the deprojection is acceptable

The vertical scale height function used for the convolution process is given by

$$g(r) = \int_{-\infty}^{+\infty} \frac{\rho_z(z)}{\sqrt{r^2 + z^2}} \, dz \tag{4.7}$$

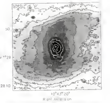

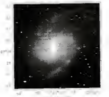

Figure 4.3 The deprojected I band image of NGC [illegible] from which the gravitational potential of the galaxy was extracted. The image has been rotated so that the major axis of the bar is aligned with the y axis of the graph.

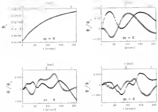

Figure 4.4 Graphical representation of the Fourier components of the potential listed in Table 4.1. Filled triangles and opened squares represent the cosine and sine terms of the components respectively.

where r is some radius in the galactic plane and the vertical density profile normalizes to one ($\int_{-\infty}^{+\infty} \rho_z(z) = 1$). It is assumed that the vertical distribution of the mass density resembles an isothermal disk so that

$$\rho_z(z) = (1/2h)\,\mathrm{sech}^2(z/h) \tag{4.8}$$

The term h denotes the vertical scale height of the disk. In Cartesian coordinates, the gravitational field of the galactic plane (that the stellar kinematics and hydrodynamical models will be based on) can be written as

$$\Phi(x,y) = -G \int \Sigma(x',y')\, g(x-x', y-y')\,\mathrm{d}x'\,\mathrm{d}y' \tag{4.9}$$

where Σ is the surface mass density (i.e., the deprojected image has unit values of $M_\odot$ pc^{-2}). The actual convolution process was made by multiplying the rectified image

Table 4-1 Polynomial coefficients of the gravitational potential of NGC 3359

Coefficient	$\Phi_0(r)$	$\Phi_{2c}(r)$	$\Phi_{2s}(r)$	$\Phi_{4c}(r)$	$\Phi_{4s}(r)$	$\Phi_{6c}(r)$	$\Phi_{6s}(r)$
a_0	5.459E+4	2.077E+2	1.907E+2	3.182E+1	3.109E+1	1.301E+1	-8.902E+0
[illegible]	9.206E+3	2.830E+3	1.405E+3	3.394E+2	2.261E+1	5.746E+1	1.768E+1
[illegible]	7.444E+2	1.111E+3	2.752E+3	2.753E+2	1.501E+2	1.025E+0	1.330E+1
[illegible]	1.923E+1	1.400E+2	1.613E+3	1.018E+2	1.304E+2	2.941E+1	1.076E+1
[illegible]	2.796E+1	1.435E+2	4.320E+2	3.707E+1	3.705E+1	3.271E+1	8.172E+0
[illegible]	5.408E+0	3.920E+1	6.183E+1	5.442E+0	5.361E+0	2.349E+0	7.759E+0
[illegible]	9.170E-1	2.972E+0	4.021E+0	2.907E-1	4.239E-1	2.156E-1	1.870E-1
[illegible]	3.380E-2	1.410E-1	-2.980E-1	1.411E-2	1.732E-2	8.875E-3	9.705E-3
[illegible]	7.053E-4	2.660E-3	3.544E-3	2.737E-4	2.918E-4	1.802E-4	1.998E-4

with the convolution function in Fourier space. The function itself was also an image that was created with an IDL program written by R. Pina.

The potential in the plane of the galaxy can be expressed in the form of a Fourier series so that

$$\Phi(r,\varphi) = \Phi_0(r) + \sum_{m>0} \Phi_{mc}(r)\cos(m\varphi) + \Phi_{ms}(r)\sin(m\varphi) \tag{4.10}$$

To find the components Φ_0, Φ_{mc} and Φ_{ms} of the equation above, the potential was divided into concentric annuli with the width of each ring being equal to one beamwidth (point spread function FWHM). A polynomial fit (of the form $\sum_n a_n r^n$) was made to the components. Table 4-1 lists the coefficients of the polynomials obtained from the fit. Similarly the Fourier coefficients are also shown graphically in Figure 4-4. As expected, the axisymmetric part of the potential dominates most of the galactic gravitational field and the bar is a weak perturber of the total potential, its maximum strength is less than 4% of the Φ_0 component. The Φ_{2c} term peaks at 32″ and crosses the Φ_{2s} term at around 65″. The latter position is close to the (deprojected) corotation radius (r_{RC}) of 63″ as given by Aguerri et al. (1998) and one that has been adopted for this chapter. At 65″ (3.36 kpc) $r_{RC} = 1.3\ R_{bar}$ that is within the 1.2 ± 0.2 range proposed by Athanassoula (1992a).

A few comments should be made about the derived potential. First, it was assumed that the mass-to-light ratio (M/L) was constant throughout the disk of the galaxy. This assumption does not appear to be threatened as the color differences between the infrared images shown in Chapter 3 show no dramatic population change throughout

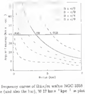

Figure 4.5 Angular frequency curves of $\Omega \pm \kappa/m$ within NGC 3359. The rotation rate of the reference frame (and also the bar), 39.17 km s^{-1} kpc^{-1}, is plotted as the solid horizontal line. Its intersection with the other curves of the figure mark the (approximate) positions of the major resonances in the galaxy.

the disk. Also, several potentials were created using different values of h and M/L to derive theoretical circular velocities that were then compared with the observed H I and Hα rotation curves. The best estimated values for the (imperfect) match between the rotation curves are 700 pc and 1.66 for h and M/L respectively. The differences between the theoretical and observed curves can be attributed to some, if not all, of the following reasons: the different kinematical values used to estimate V_c, beam smearing, and bar streaming motions. The potential will be used to describe the dynamics of the disk component. However, it lacks the inclusion of an explicit bulge component (however small the bulge may be) and is not accurate close to the center of the galaxy.

As mentioned in the end of last section, barred spirals normally do not have physical characteristics that reveal the positions of resonances unambiguously. Thus, it is left to theory to determine their locations. As an aid to locating the resonances of NGC 3359, the $m = 2, 3, 4$, and 6 terms of $\Omega \pm \kappa/m$ have been plotted in Figure 4-5. The pattern speed Ω_b at the corotation radius is assumed to be equal to 39.17 km s^{-1} kpc^{-1} (the horizontal line of the figure). The locations of the other resonances can be found by noting where the $\Omega \pm \kappa/m$ curves intersect with Ω_b.

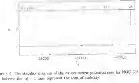

Figure 4.6 The stability diagram of the axisymmetric potential case for NGC 3358. The area between the $|\alpha| = 1$ lines represent the zone of stability.

4.3 Periodic Orbits and their Stability

Periodic orbits provide the backbone structure to a disk galaxy. If orbits are stable, then they will trap non-periodic orbits around them. However, if they are unstable, stochasticity is introduced to the nearby neighborhood (Contopoulos 2002). In the full bar potential the x_1 orbits are elongated along the bar and provide support when the perturbation is added to the total potential. For example, Patsis et al. (1997) found that x_1 supported the bar up the 4:1 resonance–or the end of the bar in the case of NGC 4314. The location and stability of periodic orbits in a given potential Φ can be found by using characteristic and stability diagrams. Appendix D gives the mathematical derivation of such diagrams. The focus for the rest of this chapter is to use the 2-D digrams to investigate the central family of orbits within NGC 3358.

4.3.1 Axisymmetric Case

In an axisymmetric potential, the x_1 family consists of direct and stable orbits that rotate circularly. The family is also comprised of the main $n:1$ resonance orbits that are simple-periodic in nature. Figure 4.6 shows the stability diagram of the x_1 family within the axisymmetric potential of the galaxy. The Hénon index values fluctuate between the lines of stability limit $|\alpha| = 1$. These lines denote the transition to instability and occurs near resonances. It can be seen that x_1 is stable everywhere. As marked in the stability diagram, the $m = 2$, 3, and 4 resonances occur at energies whose radial distances correspond to 0.11, 0.98, and 1.57 kpc respectively. The spacings between the higher order resonances become smaller as one approaches the CR. The separation between the last marked point (the 4:1 resonance) and corotation is 1.8 kpc. Note that the quoted distances apply only to the axisymmetric case as the values will change when the nonaxisymmetric Fourier components are added. The behavior shown in the diagram is typical for disk galaxies with axisymmetric potentials (Contopoulos & Grosbøl 1986).

4.4.2 Non-axisymmetric Case

Although the Φ_2, Φ_4, and Φ_6 terms of Table 4-1 (or Figure 4-4) indicate that they are rather weak as compared to the axisymmetric component of the potential, their influence on stellar orbits is significant. In this section, the impact of including the cosine and sine terms to the potential will be explored with the aid of stability and characteristic diagrams.

The stability diagram of the current model (Figure 4-7) indicates that the 3:1 resonance has shifted toward lower energy but is also larger in size. For $-51460 < E_J < -51680$, $\alpha > 1$. The intersection of the the stability curve with the $\alpha = 1$ axis is important: either a new stable (S) or unstable (U) set of periodic orbits are introduced into the system through bifurcation of the old parent family at the point. The new set will inherit the periodicity and stability of its progenitor. When a S → U transition occurs, the original family becomes unstable while bifurcating a new stable family. Conversely, a new unstable set of orbits is introduced into the system after a U → S transition. For the case at hand, an "inverse bifurcation" (Contopoulos 2002) is present (i.e., the new branch extends toward lower energies). However, the influence of the 3:1 resonance on the dynamics of the system is only local and hence an in-depth study of this phenomenon will not be explored here. The stability curve of the new 3:1 family that bifurcated from the S → U transition at $E_J = -51455$ has been plotted in the diagram. Near the 4:1 resonance, the stability curve has been noticeably reduced by the non-axisymmetric terms. The leveling off of the curve at the 4:1 resonance is not atypical. Near the 4:1 resonance, the stability curve has been noticeably reduced by the

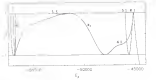

Figure 4–7 The stability diagram of x_1 and other stable families using the full potential listed in Table 4-1 The n 1 labels refer to the values of the Jacobian E_J for the associated resonances, and not to the names of the families

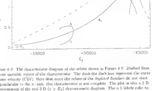

Figure 4–8 The characteristic diagram of the orbits shown in Figure 4 7 Dashed lines denote unstable region of the characteristic The dash-dot dash line represent the curve of zero velocity (CZV) Note that since the orbits of the depicted families do not start perpendicular to the x−axis this characteristic is not complete The plot is also a 2 D representation of the real 3 D (z x E_J) characteristic diagram The n 1 labels refer to the values of the Jacobian E_J for the associated resonances and not to the names of the families

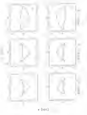

Figure 4-9 Evolution of the bifurcated 3:1 family orbits. Representative orbits from both (1 and 1') branches are shown.

non-axisymmetric terms. The leveling off of the curve at the 4:1 resonance is not atypical (Contopoulos & Grosbøl 1986, 1989; Patsis 1991) as Patsis & Grosbøl (1996) have even observed similar occurrence in their study of 3-D galactic models. The original x_1 stability curve also effectively ends at this region. The next curve starts off at higher stability value and ends at the 6:1 resonance, much like Figure 8 of Contopoulos & Grosbøl (1986).

Another frequently used tool for the study of the orbital dynamics of 2-D models is the characteristic diagram. It gives the x coordinate of the initial conditions of the periodic orbits of a family as a function of their Jacobi constant E_J. In the case of orbits starting perpendicular to the x axis ($p_x = 0$), with $y = 0$ and $p_y > 0$, only one initial condition, x, is required to specify a periodic orbit on the diagram. Thus, the initial conditions of such orbits are fully determined by a point on the characteristic diagram. Initial conditions of orbits that do not start perpendicular to the x axis are

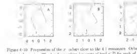

Figure 4-10. Progression of the x_1 orbits close to the 4:1 resonance. Orbit B is the stellar orbit at the x_1 tip. The Jacobian values (in units of km^2 s^{-2}) for each of the orbits are as follows: A) −47000, B) −46540 and C) −45780 respectively. The axes are in units of kpc.

not fully defined by their x coordinate. In these more general cases, the representation on the (E_J, x) diagram is not very useful. Owing to the form of the potential used to describe the potential of NGC 3359, the orbits of the x_1 family do not have $p_x = 0$ in general. Nevertheless, the (E_J, x) projection will be given to describe the evolution of the families in the models. The curve of zero velocity (CZV) line in Figure 4-8 denotes the region that stars may travel. At this line $\Phi_r = E_J$ and so any star on the CZV has zero velocity. Moving from the lowest energy in the diagram, the x_1 characteristic branches up the x axis monotonically with increasing E_J until the the 4:1 gap is encountered. At $(E_J, x) = (-46540, 1.28)$ the tip of the branch is reached and the curve begins to deviate downward with increasing energy. This gap is a typical behavior at the UHR. There are two classes of gap associated with the 4:1 resonance (Figure 1b of Contopoulos & Grosbol 1989). For the type 1 gap, the characteristic has no maximum peak but instead turn upward toward the CZV and a new, but unstable, x_1 family forms at equal energy but with lower x values. However, if the characteristic instead reaches a maximum x and deviate downward then type 2 gap is present. The new x_1 branch can be found at larger x values for the same energy but it is also unstable-i.e. the lower part of the curve is stable (Figure 2b of Contopoulos 1988). The 4:1 gap displayed by the x_1 characteristic curve for NGC 3359 is type 2. Beyond the gap, a new characteristic curve for the 5:1 and 6:1 family appears. This characteristic peaks at $(E_J, x) = (-45180, 1.4)$ and creates another (6:1) gap. In general, the central family will have gaps at all even resonances (Contopoulos & Grosbol 1986).

There are several regions in the two diagrams that merit close inspection. The first is near the center of the galaxy where two families have the equal energy (from $E_J = -57070$ to -56875) but different initial starting positions x. Here, the x_2 orbits lies above a smaller subset of orbits that become more elongated along toward the minor axis of the bar as the energy decreases (Figure 4-8). These orbits are similar to the x_1 family found by Patsis et al. (1997) that start out as ellipses along the bar major axis and fold at toward the minor axis for lower energies. Although these orbits are stable and periodic, their orbital extent and energies are small and therefore appear to play a minor role in the dynamics of the system.

The bifurcation of the new 3:1 branches from its associated resonance is also a point of interest as it is a good example of introducing the concept of bifurcation in a dynamical system. Here, the system corresponds to a potential that has been obtained directly from observations. When instability occurs at the odd resonances, two bifurcated families can be found just as shown in Figure 4-9. Although these branches have the same stability and energy values, their initial $(x, \dot{x})$ are different. The evolution of both t and t′ branches (Figure 4-9) display the typical mirror behavior for the bifurcated family (Contopoulos & Grosbøl 1989). It can be said that they are two branches of the same family; their orbits develop loops with decreasing energies. The shapes of these orbits are reminiscent of Figure 3b of Athanassoula (1992a). The top panel of the figure gives the maximum distance of the orbits of approximately 1.2 kpc or close to half of the bar radius. As in all of the orbits shown here, these orbits are only important when they are stable and can trap non periodic orbits.

The remaining areas of examination comprise of the higher order resonances. The orbits of x_2 start to develop loops around the tip of the branch (Figure 4-10). The 5:1 family is bifurcated from the 4:1 family and Figure 4-11C gives an example of its morphology. This family has a narrow stable part (Figure 4-7) between ~ -45000 and -45200. Close to -45200 the morphology of the 4:1 family tends to be barrel-like (i.e., its morphology is influenced by the 6:1 resonance). These orbits provide the longest projection orbits on the major axis of the bar. In essence, the 4:1 orbits, like those in NGC 4314 (Patsis et al. 1997), define the limiting radius of the bar.

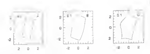

Figure 4-11. 4:1 to 6:1 stable orbits that support the bar. The Jacobian values (in units of km^2 s^{-2}) for each of the orbits are as follows: A) −45970, B) −45598, and C) −45028 respectively. The axes are in units of kpc.

4.4 Conclusion

The goal of this chapter was to find the simple-periodic orbits that support the bar of NGC 3359. The results are consistent with the E_J value expected at the end of the bar. Because the (deprojected) radius of the bar about 2.3 kpc, the estimated Jacobi constant at this distance is approximately −44300. All the stable periodic orbits that build up the bar structure have energies less than this energy value. The x_1 makes up the predominant "central" family of such orbits. There are other families of stable orbits that are not part of x_1 but also partially support the bar (Figure 4-8). These orbits are formed only near the resonances of the galaxy and as such, affect the dynamics of the system locally. The last set of orbits that have the longest elongation along the bar length can be found between the 4:1 and 6:1 gap. The outer structure of the bar is defined by this family (within E_J = −46000 and −45200): the rectangular-like shape orbits (Figure 4-12) mimic the boxy isophotes near the ends of the real bar.

The derived gravitation potential also appears to be a good approximation of the true potential, because the shapes and extent of the orbits reproduce the light contours of the bar well, including the observed isophotal twist. I conclude that the theory of stellar orbits applies very well in this system. Notice that in the case of a real galaxy, not all stable orbits will be populated. The sense of rotation, the energy of a family, and other factors such as a companion determine which and in what degree the stable orbits of a family will be populated. One is justified to choose the stable orbits needed to construct an appropriate model for a galaxy.

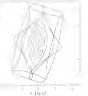

Figure 4 12 Representatives of the stable periodic orbits supporting the observed bar morphology in NGC 3359

Finally the same orbital analysis has been applied to several models with different bar speed values The primary result of applying such changes is that the location of the resonances and hence the length of the bar are different for each instance Faster angular velocities produced models with shorter bars and the opposite is true for lower values of Ω_b However the dynamics of the models at the same resonance remains similar independent of the location of the resonance on the disk The model presented here rotating with $\Omega_b = 38\ 17$ km s kpc $^{-1}$ places corotation at 3 5 kpc i e about 1 3 times the length of the bar This important result should be kept in mind as we proceed to the study of the hydrodynamical models for NGC 3359 in the following chapter

CHAPTER 5
GASDYNAMICAL MODELS

5.1 Introduction

Despite its relatively small contribution to the overall mass of a barred spiral galaxy, gas is a major contributor to the stability and evolution of galactic structures. The heat generated in a spiral galaxy owes its origin mainly to stars which exert work on the gas while the latter radiates away the energy and tries to keep the system cool and stable. In terms of evolution, Friedli & Martinet (1993) have shown that a large influx of gas driven into the central region can ultimately lead to the dissolution of the bar itself. This destructive process is due to the growth of the ILR(s) which effectively reduces the percentage of stellar orbits trapped around periodic bar supporting orbits. The spiral structures within the disk also appear to be maintained by the gas content of the galaxy. Specifically, the stellar spiral response is maintained for a longer period with the presence of gas and its cooling property (Lindblad 1996). Such theoretical findings are supported observationally by the lack of spiral structures seen in gas-depleted, early type barred galaxies. Hence, despite their low mass fraction to the overall galactic mass, the existence and evolution of gas plays a profound role in the structures of the disk systems and merit further analysis. Such investigations will be made via numerical simulations in this chapter.

Past numerical experiments have shown that the general response of gas to a gravitational potential can be predicted if the families of periodic orbits in the underlying potential are known. However, gas exerts pressure and is naturally dissipative and viscous. These characteristics combine to alter the pattern of gas flow near resonances. Around these locations, stars can cross orbits and/or develop loops as they are considered to be collisionless. However, gas is confined to travel on non-crossing orbits (Friedli & Benz 1993). Consequently, there is a gradual shift in the flowlines which causes orbital crowding and shocks. This effect has been attributed to the creation of dust lanes seen

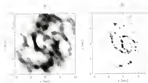

Figure 5 1 Deprojected grayscale images of the A) cold atomic and B) ionized hydrogen gas distribution

in numerical simulations (Athanassoula 1992b Englmaier & Gerhard 1997 Hunter et al 1988 Patsis & Athanassoula 2000 hereafter PA00 Sanders & Huntley 1976 Sanders & Tubbs 1980) Such differences between the stellar and gaseous components of the galaxy therefore merit different modeling techniques

Smooth Particle Hydrodynamics (SPH) is the numerical method used in this chapter to simulate the gasdynamics of NGC 3359 The main distinction which separates it (and other hydrodynamical programs) from stellar N body codes is the insertion of a damping (e g viscosity or friction) term which causes a phase delay to the responses of the gas orbits to the periodic driving force of the bar (Wada 1994) The additional term causes the damped orbits to gradually shift in their orientation Such numerical simulations of gasdynamics in barred galaxies have been performed here at the University of Florida for the past three decades In simulating the gas flow of the barred galaxies NGC 1073 1300 3359 3992 and 4731 (see e g England 1986 Hunter 1990 and references therein) the authors used the Beam scheme procedure (Sanders & Prendergast 1974) to model successfully the observed H I morphologies and velocity fields However their method required the addition of an oval component to the mass distribution to produce spiral arms at large radii It will be shown that the method used in this chapter obviates the

Table 5 1 Units in the SPH simulations

Property	Value
G	1
Length	1 kpc
Mass	2 33 × 10^5 $M_\odot$
Time	980 Myr
Velocity	1 km s^{-1}

used to add an ad hoc component to reproduce the gas distribution and velocity field of NGC 3359

The outline of this chapter is as follows The next section is a brief overview of the methodologies used to investigate the gasdynamical models Four models of different pattern speeds will be presented and analyzed with the observed data in Sections 3 and 4 Results and conclusions from the study are discussed in the last section

5 2 Overview

The goal for this phase of research is to create hydrodynamical models the properties of which duplicate the observed atomic and ionized hydrogen gas component of NGC 3359 It is assumed that the input parameters which produce the best fitting models are close approximations to the actual properties of the galaxy A modified version of the code used in PA00 has been used to create the hydrodynamical models which are discussed below An essential part of this work has been performed during my two month stay at the Academy of Athens in 2002 under the supervision of P Patsis The details of the numerical scheme can be found in Appendix C An extensive test of the properties of the code was performed by PA00 who also found the following (1) the gas response is essentially the same for models that have at least 10^4 particles The only significant difference between simulations with small and large number of sample points is that certain areas will contain fewer particles thereby reducing the resolution of the data, and (2) the optimal numerical values for the artificial viscosity is $(\alpha\ \beta) = (1\ 2)$ The definitions for α and β are given in Appendix D These results are used in all of the models analysed in this chapter In addition the code has been tested to produce identical results with those in Patsis et al (1994) and Patsis et al (1997) The SPH program was shown to be consistent with another extensively tested and widely used hydrodynamical code called the Flux Splitting second order accurate scheme (FS2) (van Albada & Roberts 1981 PA00)

The starting properties used at the beginning of each simulation are as follows The radius of the initial two-dimensional disk of gas particles is between 10 to 12 kpc The gas is assumed to be isothermal and has a sound speed of 10 km s^{-1} Self gravity is not taken into account as the gas is assumed to be tenuous The particles are initially subjected to only the axisymmetric part of the potential which was derived in the last chapter There are typically 15 000 to 20 000 particles at the beginning of each run The non axisymmetric (i e barred and spiral) perturbation is introduced gradually and linearly so that the gas may adjust to the forcing terms within two to three pattern rotations (Ω_p) The particles were initially set on circular orbits as determined by the rotation curve obtained from the axisymmetric part of the input potential The physical units of the simulations are given in Table 5-1

After each model was created snapshots at different (time) stages of the simulations were directly compared with the H I and H II gas morphologies (Figure 5-1) and the H I velocity field (the patchy nature of the H II velocity field prevented its usage) The criteria used to test the accuracy of the models can be separated into two broad categories

1) Morphology The surface density of the models should resemble the observed gas (i e H I and H II) distribution Several prominent characteristics of NGC 3359 will be used to compare with the model. These are the inner H I spiral arms and the pseudo-ring like annulus formed by the two structures The depression of gas density within the bar region should also be present in the snapshots

2) Kinematics Velocity information exists in both observable and model data Thus their velocity fields can be used to check for qualitative correspondence with particular attention paid to the the kinks near the bar and spiral arms Rotation curves taken from the major-axis profiles of the velocity fields allow for another method to check for the compatibility of the two data.

As the models are not expected to be perfect re-creations of the actual gas distributions only the gross general characteristics of the models are inspected for the goodness

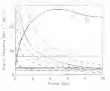

Figure 5-2. Angular frequency curves calculated from the axisymmetric part of the gravitational potential. The four horizontal lines mark the pattern speeds of the Models A–D. The dashed and dotted lines represent the $\Omega \pm \kappa/2$ and $\Omega \pm \kappa/4$ frequencies respectively. The $\Omega - \kappa/3$ and $\Omega - \kappa/6$ frequencies are denoted by the dash dot dashed lines. The solid line represents the circular frequency Ω calculated from the axisymmetric rotation curve (V_c).

of fit to the actual galaxy. Special emphasis will be made for the correspondence between the model and observed spiral arms. The current potential inherently contains the spiral density wave pattern that is typically added as a separate component in previous gasdynamical studies.

The comparative analysis performed here is based only on qualitative fits. That is, no quantitative procedures such as the χ^2-test have been performed. The discrepancies that arise from mismatched strong density or velocity points could be misleading in such tests (Lindblad 1996). The visual inspection methods performed in this chapter should be sufficient for the simple 2-D gas-only models being analyzed here.

5.3 Gas Models and Morphologies

The most important parameter of the simulations is the pattern speed at which the models rotate. Several models were constructed with various values of Ω_p. From these simulations four cases (Models A–D) are of interest. It will be shown that by altering the pattern speeds of the models, the size and extent of the major features of the galaxy

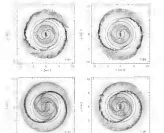

Figure 5-3. Evolution of the particle distribution for Model A (with $\Omega_p = 39.17$ km s^{-1} kpc^{-1}). The circles starting from the innermost denote the 4:1, corotation, −4:1, and outer Lindblad resonances. Listed at the bottom right corner of each panel is the time of each snapshot.

can be varied extensively. Figure 5-2 can be used as a guide to the approximate locations of the resonances which are pointed out in the following discussions.

5.3.1 Model A

The first obvious choice of pattern speed for the simulations is $\Omega_p = 39.17$ km s^{-1} kpc^{-1}, the value used to show the stellar orbits which provided bar support. The evolution of Model A is shown in Figure 5-3. The distribution of the particles is fairly smooth within $r \sim 4.7$ kpc (i.e., the −4:1 resonance). Beyond this radius, two clumpy outer arms form and quickly wind around the disk. Within the inner disk, a pair of

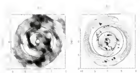

Figure 5.4 Gas response of Model A (contour lines) at three bar rotations and after smoothing the original particle density image with a 15″ Gaussian beam. The inner and outer circles indicate the positions of the CR and OLR respectively.

trailing inner spiral enhancements form at the ends of the bar and appear to end near the CR position of 3.35 kpc. The length of the bar in this model is approximately 2 kpc.

The comparison of the morphologies of Model A and the actual galaxy (Figure 5.4) show that the gas response from the simulation is markedly different nearly everywhere. The contours of the model show that the spirals which extend from the short gas bar overlap a small region of the actual arms. However, it is obvious that their origins (i.e. where they attach to the bar) are well short of the actual beginning of the observed spiral arms. The outer arms appear to originate close to the corotation radius and overlap parts of the H I regions (marked α and β) which reside to the east and west of the pseudo H I gas-ring. These arms are long-lived features that appear to the end of the simulations (t=1.4). It is also of interest to note that they exist beyond the OLR. It has been suggested from previous gasdynamical studies (e.g. Ball 1992 and references therein) that a pure bar potential cannot produce spiral arms which extend much further than the corotation radius. The present case does not contradict such observations, as the underlying potential contains both the bar and spiral density waves components that are typically added piecemeal during hydrodynamical simulations. However, their morphology underlines the fact that the current pattern speed is clearly insufficient to reproduce the gas distribution of NGC 3359. In the subsequent models, slower pattern

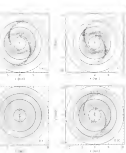

Figure 5-5 Evolution of the particle distribution for Model B (with $\Omega_p = 15.52$ km s^{-1} kpc^{-1}). The circles, starting from the innermost, denote the radius of the bar, the positions of the UHR, CR, and OLR.

speeds are used to produce gas responses which have much better correspondence with the major features of the galaxy.

Owing to the overall morphological mismatch as described above, Model A is considered an unrealistic representation of NGC 3359, although the same pattern speed has been shown to produce the stellar orbits which describe the structure of the bar.

5.3.2 Model B

The gas distribution of NGC 3359 is much better reproduced by using slower pattern speeds in the simulations. The evolution of Model B, with $\Omega_p = 15.52$ km s^{-1} kpc^{-1}, is shown in Figures 5-5 and 5-6. In Figure 5-7, contours of the model gas response are

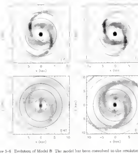

Figure 5-6 Evolution of Model B The model has been convolved to the resolution of the H I data (15″) Circles are the same as Figure 5-5

plotted on the grayscale image of the H I surface density map It can be seen that the observed H I depression in the bar region is duplicated in the model also The model arms attach to the ends of the bar and spiral outward with pitch angles that are in good agreement with observations. Also the middle of the arms along with the ends of the bar contain the greatest concentration of particles throughout the simulation After viewing Model B in a movie sequence of snapshots it was noticed that most of the density maxima are confined within and up to the 4:1 ultraharmonic (UHR) resonance located at $r = 5.88$ kpc In the north the model arm winds slightly faster than the observed arm This is also true for the next model It is possible that a small warp in the

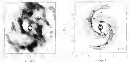

Figure 5-7. Gas response of Model B (contour lines) at t=1.15. Explanation of A and B markers is given in the text.

disk is the cause of this minor discrepancy. Conversely, the similarities between the model and the observed arms show that the disk of the galaxy has no significant warping.

There is also good correspondence between the morphology of the model and the observed distribution of ionized hydrogen gas in NGC 3359 (Figure 5-7). The H II gas arms are fitted especially well by the model arms. Several of the density maxima in the model overlap the SF zones, particular at the ends of the bar and the large H II regions located in the middle of the eastern arm (region A). The maxima indicate regions of shocked regions where gas is compressed and leading to formation of new stars. However there is no observable SF region which corresponds to the density maximum of the western arm (region B). Both A and B are persistent areas of density maxima where the gas particles are constantly shocked.

5.3.3 Model C

The angular frequency of this model is 13.53 km s^{-1} kpc^{-1}. Given that the value of the pattern speed is only slightly less than Ω_p of Model B, the results of this simulation do not differ greatly from those of the former. Nonetheless Model C is presented here as it contains many similar features seen in the real galaxy.

The evolution (Figures 5-8 and 5-9) and morphology (Figure 5-10) of the model once again shows that the density maxima lie within the UHR. Most of the features seen in Model B are duplicated in the present case. However, they exist slightly further out in

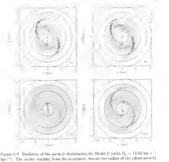

Figure 5-8 Evolution of the particle distribution for Model C (with $\Omega_p = 13.53$ km s^{-1} kpc^{-1}) The circles starting from the innermost, denote the radius of the (deprojected) bar and the positions of the UHR CR, and OLR.

the disk owing to the slower rotation rate Consequently the spiral arms are marginally more open although they still coincide with the observed gas arms quite well

The best attribute of Model C is its reproduction of the point where the eastern arm breaks/bifurcates into separate segments (arm spurs) in the northern half of the galaxy The separation is noticeable in both data sets though it is much easier to see in the Hα intensity map (Figure 5-10B) near $(x\ y) = (-3\ 3\ 5)$ kpc. Unfortunately the contour line outlining the break does not trace out the bifurcated arm (spur) to large distances This feature is not observed in Model A or B

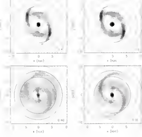

Figure 5.9 Evolution of Model C. The model has been convolved to the resolution of the H I data (18″). Circles are the same as Figure 5-8.

5.3.4 Model D

In order to see if improvements of the matching between the models and the observations can still be made, the pattern speed was decreased to 10.00 km s^{-1} kpc^{-1}. The model arms are now quite flaccid and barely overlap the real gas arms. The shock locations at the ends of the model bar have been shifted counterclockwise throughout the length of simulation, the density of the two regions decrease to the current observed morphology of Figure 5.11. Thus, the gas response of the model in Figure 5.11 (and also its kinematics, see subsection 4.3) indicates that lower limit of Ω_p has been exceeded. Yet, the primary concern of this chapter is to obtain the proper Ω_p value to match the gas spiral arms. And for the previous two models, the simulations have been in agreement

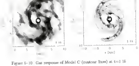

Figure 5-10. Gas response of Model C (contour lines) at t=1.16.

with observations. However, the gas response of Model D differed considerably from the observations and led me to conclude that the lower limit of the spiral pattern speed has been exceeded.

Note that although the snapshot time for Figure 5.11 is only at t=0.78, the full bar potential time was set to t=0.64 to produce the model (for a quick inspection and determination of the pattern speed limit). Hence, the model is as dynamically evolved as the others.

5.3.5 Surface Density Radial Profiles

The azimuthally averaged surface density profiles for various snapshots of Model B and the H I disk are presented in Figure 5.12. The initial disk of uniformly distributed particles evolved to one with an annulus of high surface density located between 2–4 kpc from the galactic center, matching the observed pseudo H I gas-ring (Chapter 2). Farther out, only the last snapshot of the model (t=1.64) shows a very small increase in the surface density corresponds to that of the H I disk near 7.6 kpc. However, it can be seen that the radial profiles of the model at later times (i.e., after the bar perturbation has been fully introduced) are qualitatively similar to the observed H I gas profiles in shape. The density contrast, however, is higher for the later snapshots than the actual gas profile. The ratio of the maximum over the mean value for the H I profile for $30' < r < 150''$ is approximately 1.18 while they are 1.80 to 1.94 for the last three profiles of the figure. The best quantitative match is from the snapshot taken at t=0.90.

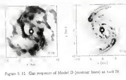

Figure 5-11. Gas response of Model D (contour lines) at t=0.78.

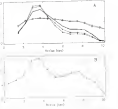

Figure 5-12. Azimuthally averaged surface density profiles for A) various snapshots of Model B and B) the H I disk. The times for the snapshots are t=0.77 (open circles), 0.81 (open squares), 1.55 (filled triangles) and 1.64 (filled squares). The dark solid line denote the time (t=1.40) when the potential is fully introduced.

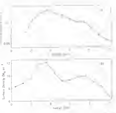

Figure 5-13 A) Surface density profiles of Model B at t=0.90 and B) th [illegible] the major axis slice

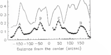

Figure 5-14 Major axis surface density profiles of Model B at t=0.90 (filled triangles) and the H I data (solid lines)

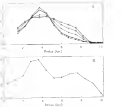

Figure 5 15 Azimuthally averaged surface density profiles for A) various snapshots of Model C and B) the H I disk The times for the snapshots are t=0 78 (open circles) 0 90 (open squares) 1 11 (filled triangles) and 1 56 (filled squares) The dark solid line denotes the time (t=1 41) when the potential is fully introduced.

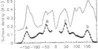

Figure 5 16 Major axis surface density profiles of Model C at t=0 803 (filled triangles) and the H I data (solid lines)

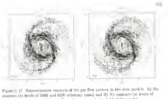

Figure 5.17 Representative example of the gas flow pattern in the slow models. A) Hα contours (at levels of 2000 and 6500 arbitrary units) and B) H I contours (at levels of 10.9, 15.1, 18.4, and 20.5 M$_\odot$ pc^{-2}) on the vector velocity field of the model.

(Figure 5.13A) where the ratio of max/mean is 1.18. Also shown is the major axis surface density profiles of both data in Figure 5-14. The cut passes through the ends of the bar (the inner peaks) and the spiral arms (the outer peaks of the figure). The model profile maxima at points A–C are less than 250 pc from the H I peaks. The largest offset between the peaks of the two data ($\sim$ 500 pc) occurs at point D. There is also a slight discrepancy in the general shape of the profiles. The model slice shows that the ends of the bar have higher density than the arms, while the opposite is true for the H I profile. The difference could be due to the fact that no additional gas particles are added during the simulation. For the real case, H I gas can be replenished through various mechanism (e.g., photodissociation of surrounding H$_2$ clouds from OB stars). Similar surface density diagrams for Model C are shown in Figures 5-15 and 5-16.

5.3.6 Gas Flow Pattern

Representative diagrams of the flow pattern of gas in the slow models are shown as velocity vectors in Figure 5-17. The orientation of the gas orbits in the center region region is aligned with the x_1 family and therefore flow parallel to the bar. The vectors crowd around the ends of the bar where the gas particles are shocked and flow inward as angular momentum is lost. Such tendencies also occur around the inner parts of the spiral arms. Consequently, there is good analogy between the crowding of the flowlines that the locations of the H II regions (Figure 5-17A). This naturally explains compressions of gas that instigate the formation of new stars. Other areas of star formation, which lie in low density regions, may have been formed by mechanisms other than gas compression due to crowding of the orbits (e.g. spontaneous star formation).

5.4 Kinematics

In this section, the kinematical information of the models will be compared with the observed data. The model velocity fields that are shown have been projected to the same sky orientation as NGC 3359 and convolved to 15″ resolution to match the detail of the higher resolution data of the 21-cm observations. The RMS errors (~ 5 km s^{-1}) associated with velocity values given here are due to the convolution process that smoothed down the original velocity values. The reader is advised to keep in mind that the bar of NGC 3359 is considered to be young and forming (Martin & Roy 1995) and it is unclear which features of a standard bar have time to develop properly. This ambiguity can be responsible for some of the deviations discussed below. In addition, only a qualitative analysis, like those performed in the previous section, is made here. This is due to the following sequence of events that occur during the simulations: the SPH particles are shocked as they move around the center of the galaxy and loose angular momentum. Consequently, there is a continuous streaming of particles to smaller radii. And because there is no replenishment of particles during the simulations, the comparison of the kinematics can only be done on a qualitative level.

5.4.1 Model A

In Figure 5-18, the velocity fields of Model A and the 21-cm data have been drawn on the grayscale image of the H I density map. Particular attention should be paid to the bar region (marked by the circle in the diagram), as the pattern speed of this model is the same as that of the bar. Within the bar dominated region, the behavior of the model isovels (particularly those west of the galactic center) is similar to the real contours. Immediately NW and SE of the nucleus and within the first 20″, the kinks in the contour lines made by the twisted elliptical gas orbits in panel A match those of panel B. However, the non circular effects arising from streaming motions associated

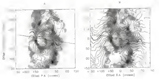

Figure 5–18 Velocity field comparison between A) the $\Omega = 39.17$ km s^{-1} kpc^{-1} model convolved to the 15″ resolution of the H I data (b). The snapshot time is t=0.807. The circle represents the bar region

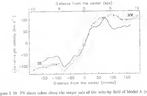

Figure 5.19 PV slices taken along the major axis of the velocity field of Model A (solid line) and the H I data (filled circles) at t=0.807

with the bar and less severe for the model NE and SW of the nucleus. The flowline of the H I gas is more disturbed than the simulated gas in its orbit around the bar. In fact the isovels in all of the models show that the gas in the western half of the bar region is disturbed considerably more than the opposite side. Thus, the zero velocity contour is better fitted to the western side owing to the fact that it, along with the real systemic velocity contour, does not intersect the minor axis line. Beyond the bar region, the model velocity field shows noticeable discrepancies. In the region where the model and observed spiral arms mismatch, the isovels likewise do not match each other (e.g., toward the western half and beyond the bar radius). Another mismatch is the location of the oval contour that indicates the turning point of the rotation curve. Panel A shows that these points on either side of the galaxy are located further in than observed.

The position velocity slice taken along the major axis, as seen in Figure 5-19, shows the discrepancy more clearly. The fit for the Model A and the H I slices is good only for the inner 25″. Beyond this radius, the two curves diverge strongly.

The following conclusions can be made for this subsection: (1) the velocity field of Model A bears close resemblance to the observed velocity field within the region dominated by the bar, (2) the streaming motions of the region are less than those in the real galaxy, as seen by the smoother model contours, and (3) the model velocity field is less credible in the outer disk, as expected from the earlier inspection of the model's morphology. Despite the stated dichotomy, this model, based on its kinematics *within the bar region only*, is worthy of further consideration.

5.4.2 Model B

The velocity field of Model B is shown in Figure 5-20. Overall, the eastern side yields a better fit. This result is not surprising as the gas response (surface density) of the model matches best with the eastern arm of the galaxy. The bending of the isovels, caused by streaming motions along the spiral arms, are nicely duplicated in the southeastern side. The contours in the NE region have similar kinks but are pulled up toward the major axis, unlike the observed data that bend back toward the minor axis at large radii. This dissimilarity owes its origin to the lack of sample points in the outer disk of the model. Subsequently, the convolution process used to smooth the image to 15″

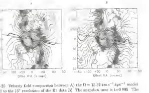

Figure 5-20 Velocity field comparison between A) the $\Omega = 15.52\ \mathrm{km\,s^{-1}\,kpc^{-1}}$ model convolved to the 15″ resolution of the H I data B) The snapshot time is t=0.805 The circle represents the bar region

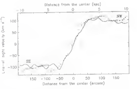

Figure 5-21 PV slices taken along the major axis of the velocity field of Model B (solid line) and the H I data (filled circles) at t=0.805

[illegible] to involve blank areas with nearby points. The model and observed [illegible] are matched primarily in the northern half away from the minor axis. The southwestern isovels are similar to their diametric counterparts in that the contours develop kinks as they traverse through the spiral arm but bend back toward the major axis shortly after returning to a more circular flow pattern. The zero (or systemic) velocity contour line of the model has a form similar to the actual line but appears to be an extended version of it. For example, in the outer disk and along the minor axis, the simulated gas flow becomes circular at about $r = 125''$, 30% farther out than the corresponding positions in Figure 5-20.

Inside the bar radius, the contours are twisted into the typical S configuration. The bending of the isovels are larger than that of Model A. It can be deduced then that the non-circular perturbations caused by the bar are larger with slower pattern speeds. Hence, gas flows inside the bar in a more elongated manner. Immediately east and west of the galactic center and on the zero (i.e., systemic) velocity contour line, there are indications of radial flow of gas along the minor axis. Inspection of the minor axis slice through the model shows that the flow of gas is directed radially inward, matching the observed H I inflow first seen in Figure 2-18C. In the western half of the bar region, the greater number of bent model isovels indicate that the degree of disturbance in the model is larger than the H I velocity field. Along the inner edge of the eastern arm, the tangential streaming motions are stronger in the real galaxy than the model, as shown by the smooth transition of the isovels through the arm.

As in the analysis of Model A, a major axis slice has been made to compare and contrast the rotation curve of Model B with the 21-cm data (Figure 5-21). The rotation curves are still qualitatively similar to Model A in the bar region. However, the H I rotational velocities in the outer disk are much better fitted with Model B. Both sides of the slice show a similar velocity drop-off. However, the velocity peak of the slice along the SE part of the model appears earlier than the H I peak ($r = 51''$ and $80''$ respectively).

5.4.3 Models C and D

Much of the kinematical conclusions reached in last subsection can be applied for the Model C. The increased radial flow of gas within the bar regime, induced by the slower

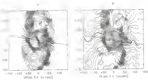

Figure 5-22 Velocity field comparison between A) the $\Omega = 13.53$ km s^{-1} kpc^{-1} model convolved to the 15" resolution of the H I data B) The snapshot time is t=0.805 The circle represents the bar region

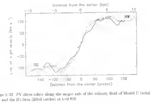

Figure 5-23 PV slices taken along the major axis of the velocity field of Model C (solid line) and the H I data (filled circles) at t=0.805

pattern speed has produced a larger disturbance to the velocity field in the bar region [illegible] the structure the isovels are noticeably skewed more so than the east in Models A and B and extend (unrealistically) up to the length of the bar The eastern isovels near the bar also begin to develop kinks similar those observed but to a lesser degree Outside the bar radius the similarities and differences exhibited between Model B and the H I velocity field are also observed for Model C Because of the smaller number of particles in the outer disk, the velocity field of Model C (Figure 5-22) is smaller than Model B

The major axis PV plot (Figure 5-23) is comparable to that of Model B In fact the SE part of the slice is a better fit to the real rotation curve of the galaxy especially where the model curve peaks (30″ Figure 5-23)

Comparisons of the kinematics of Model D with the observations proved unsatisfactory (much like the model gas response, Figure 5-11) For example the velocity gradient within the model field was larger than that of the H I This discrepancy is yet another indication that the pattern speed of Model D is the lower limit of Ω_p

In summary the results of the last two subsections show that the current potential and SPH code are adequate in producing gas models that have similar kinematical responses as the real gases within NGC 4359 The velocity field of the bar region is sensitive to the changes in the the pattern speed From the simulations lower values of Ω_p tend to induce stronger inflow of gas within the bar This in turns increases the strength of the bar streaming motions and therefore the bending of the isovelocity contours inside the region Athanassoula (2003) has recently found that the bar strengths of her models increased with slower pattern speeds

The kinematics of the gas in the outer disk is less responsive to the variations of Ω_p but shows better correspondence with the H I velocity field than that of Model A The rotation curve of the galaxy is also matched well by the models of the last two subsections with Model D being the lower limit of Ω_p The fit is most notable outside the bar radius. Inside the zone of the bar the linearly rising part of the curve is qualitatively similar to that of the fast model (Model A)

These results are in agreement with what has been found in Section 3 and further highlight the inability of simulating the gas flow within the galaxy with the bar pattern speed. The pattern speed that is required to properly simulate the distribution and kinematics of the gas in NGC 3359 lie within the range of values used to construct Models B-D.

5.5 Discussion

To state the present dilemma succinctly, NGC 3359 must have more than one pattern speed if the observed and model aspects of the galaxy are to agree. Stellar dynamics demand that the orbital structures of stars that support the bar not extend beyond the corotation radius (where chaotic orbits begin to dominate). In Chapter 4, it was demonstrated that the bar ends somewhere near either the 4:1 or 6:1 resonances, well within the CR for a pattern speed of 39.17 km s^{-1} kpc^{-1}. However, that same pattern speed failed to produce credible gas responses outside the bar region. Instead, models with lower pattern speeds were required to duplicate the H I and H II surface density morphologies and H I gas kinematics.

In a multipattern system, simulations (e.g., Sellwood & Spark, 1987; Patsis & Kaufmann 1999, hereafter PK99; Rautiainen & Salo 1999, hereafter RS99) show that the angular frequency of the bar (Ω_b) is greater than the spiral pattern (Ω_s). In addition, the pattern speed of the bar is expected to be high in order to support observational (e.g., Gerssen 2002; Aguerri et al. 2003) and numerical (e.g., Laine 1996) studies. Typically, there are three cases that occur when the rotation rates for the spiral and bar patterns are considered in conjunction with one another: (1) the patterns are rotating with the same angular frequency; (2) the features have different pattern speeds but are linked by a non-linear mechanism (Sygnet et al. 1988; Tagger et al. 1987); and (3) the angular frequencies of the bar and spiral arms are completely independent and unrelated (RS99).

It is typically accepted that the observed smooth continuation of the bar and spiral arm structures of a barred galaxy is indicative of the system being governed by a single pattern speed. However, Sellwood & Sparke (1988) have demonstrated that the bar and spiral arms can rotate at different rates, but the latter can still appear to originate from the ends of the bar. Tagger et al. (1987) suggested that such systems are linked causally through non linear coupling of resonances. NGC 3359 has been suggested to have two such pattern speeds by Sempere (1995, hereafter S95). The values of the pattern speeds of the nuclear bar and an outer bar + spiral components used by S95 simulations ($\Omega_p = 100$ and 27 km s^{-1} kpc^{-1} respectively) are quite high as compared with those used here. It is also unclear as to how the two values were determined. But it has been shown here that in order to simulate both the stellar and gas dynamics of the galaxy, two pattern speeds of smaller values are required.

5.5.1 Argument for Two Pattern Speeds

Figures 5-24 and 5-25 are illustrative examples of the stellar dynamics associated with Model B. Only Models B and C will be discussed here. The stellar orbits and gas pattern of Model D may be inferred from the discussion.

At the slower pattern speed, the simple-periodic orbits of the x_1 family extend relatively far out into the disk of the galaxy. The tip of the x_1 branch (Figure 5-24B) is now located at $E_J = -29037$ (as compared to $E_J = -46540$ for Model A). Owing to the form of the potential, the orbits precess with different E_J or radii. Most importantly, the elliptical x_1 orbits exceed the radius of 2.5 kpc, which is the extent of the bar in NGC 3359. This fact is further emphasized in Figure 5-25 where the A-O orbits have been plotted against the radius of the (stellar) bar. Figure 5-26 shows the flow pattern of the gas within Model B following stellar orbits on non-crossing paths. Both the gas simulation and stellar orbit study are in complete agreement with one another and emphasize the irreconcilable differences that arise from using a single pattern speed to simulate the galaxy. Not surprisingly, the tip of the x_1 branch for Model C is located at a smaller value of E_J (-26352) and so the x_1 orbits extend slightly farther out than in Model B (Figures 5-27 and 5-28).

In NGC 3359, the angular frequency of 39.17 km s^{-1} kpc^{-1} is sufficient to described the pattern speed at which the bar rotates. Stellar dynamics as well as the inner (bar) region of the velocity field of Model A and its rotation curve have shown that. Similarly, a value range between $\Omega_p = 15.00$ to 15.53 km s^{-1} kpc^{-1} provides the necessary ingredient to produce the models that match the outer region of the galaxy. These values are linked with the angular frequency of the bar via non linear coupling. Thus, the Ω_p

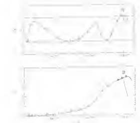

Figure 5 21 Stability A) and characteristic B) diagrams of the simple-periodic orbits in Model B The letters indicate the positions of the orbits that are plotted in Figures 5 25 and 5-26

values that were used to produce Models B-D did not come from trial and error Rather their selections were guided by the works of Tagger et al (1987) and Sellwood & Sparke (1988) The non-linear couplings associated with the current models are discussed in the following paragraph However a caveat should be stated beforehand resonance regions determined from full potentials are displaced from those predicted using only the axisymmetric part of the potential (a discussion of this offset for the ILR case is given by Athanassoula 1992b) In some cases the location of a resonance can be inferred only by careful study of the orbital dynamics Thus the resonance couplings discussed below are only approximate

In the coupling between models A and B the 4 1 resonance of the spiral pattern coincides with the OLR of the bar This scenario is similar to the work of Moore and

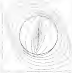

Figure 5-25 Compilation of the central family of orbits for Model B, spanning the entire x_1 characteristic curve. The thick dark circle denotes the (deprojected) radius of the bar. Only the 10 orbits of Figure 5-24 are labeled.

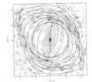

Figure 5-26 Matching correspondence between the computed x_1 orbits and the gas flowlines of Model B.

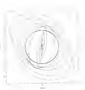

Figure 5.27 Compilation of the central family of orbits for Model C spanning the entire x_1 characteristic curve. The thick dark circle denote the (deprojected) radius of the bar

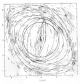

Figure 5.28 Matching correspondence between the computed x_1 orbits and the gas flowlines of Model C

Table 5.1: Properties of the Gas Models of NGC 3359

Model	Ω_p (km s^{-1} kpc^{-1})	Notes
A	39.17	Bar pattern speed
B	15.52	OLR 4:1 bar-spiral pattern coupling
C	13.53	4:1-ILR bar-spiral pattern coupling
D	10.00	4:1-ILR bar-spiral pattern coupling (see also §5.3.5)
B92	31.9	Bar + oval distortion hybrid model
S98	100 + 27	nuclear bar and outer bar+spiral

Gottesman (1995) on NGC 1398, where it was proposed that the OLR of the bar coincides with the ILR (or CR) of the spiral arms. The exact coupling between Models A and C is less clear, as one can argue that the end of the bar is located at either the 4:1 or at the 6:1 resonance. As discussed in Section 4.3, the barrel-like orbits of the 4:1 family that exist near the 6:1 resonance define the maximum extension of the bar. Thus, the ILR of the slow model (C) is probably coupled with the 4:1 rather than the 6:1 resonance; the latter is an upper limit for the bar supporting orbits and provides only marginal stability for the associated orbits (Figure 4-7). Stars are also unlikely to be trapped by orbits that are stable in a very narrow energy region, and/or being marginally stable (Patsis, private communication). In fact, and owing to the main conclusion made in the last chapter, it would be more appropriate to state that Models A and C are linked by the resonance that defines the length of the bar and the 2:1 resonance of the spirals. Support for this possibility is provided by the works of PK99, who produced realistic *N*-body models with two spiral modes coupled together. The outer spiral mode originates from the 4:1 resonance of the inner one. Table 5.2 lists the non-linear couplings associated with the models which have been discussed in this chapter.

5.5.2 Searches for Multi-pattern Speed Systems

The identification of resonances, and therefore of Ω_p, by direct observations using structural features is a difficult task in itself. Special geometries, projection effects, and other observational constraints limit our ability to determine a single pattern speed for a galaxy, much less two. Currently the Tremaine & Weinberg (1984, see also Chapter 1) procedure is the most often used method of attempting to determine pattern speeds of barred galaxies. Unfortunately, the procedure is mostly limited to galaxies of early speed because of the constraints set by the continuity equation upon which the method is based Thus [illegible] attempts to determine the elusive pattern speeds of galaxies are still left to theoretical considerations

The difficulty of obtaining a single pattern speed unambiguously naturally explains the small number of forays that have ventured into the realm of multi pattern speed investigations. Sellwood & Sparke (1988) have suggested it Tagger et al. (1987) and Sygnet et al (1988) have proffered a method (that we consider here) to explain its existence and several observations have suggested galaxies that may have it Yet the study of systems with separate bar and spiral pattern speeds has been slow to develop although the field has grown considerably in the last five or so years (e.g. Bissantz et al 2003 PK99 RS99)

The two-dimensional N-body and gas model analysis performed by R99 is of specific interest in the present context Several of the N-body models that were constructed showed evidence of two (or more) pattern speeds connected by non-linear mode coupling Some of the models showed amplitude-boosted beat modes near overlapping resonances Such elevated $m = 0$ and $m = 4$ beat modes of the $m = 2$ component are believed to be indicators of non linear couplings (Masset & Tagger 1997) but unlike the CR ILR coupling previously proposed the simulations of RS99 typically showed overlapping of the CR and 4 1 resonances. Moreover their hydrodynamical models with non linear mode coupling featured rings or pseudo-rings and multiple spiral arm features Unfortunately none of the models resembled the gas morphology of NGC 3359 probably because not one contained the OLR 4 1 or 4 1 ILR coupling that has been proposed here to explain the two pattern speed of the galaxy

One final result that requires comment is the emerging importance of the UHR for bars along with the Lindblad and corotation resonances Not only do strong spirals appear to end near the 4 1 resonance, but the location may also be associated with nonlinear coupling for some multi pattern speed systems Its importance in spiral systems has been addressed in Contopoulos & Grosbol (1986 1989)

Galaxies that could have more than one pattern speed include NGC 1068 and 1566 (Bosma 1992) NGC 1365 NGC 2273 (RS99 van Driel & Buta 1991) and as previously [illegible] NGC 1398. Overall, only a handful of barred galaxies have been conjectured [illegible] multi patterned systems. Perhaps the most obvious candidates are barred galaxies which also contain nuclear bars. Indeed, Friedli & Martinet (1993) determined that several such systems contained nuclear bars with higher angular frequency than the main bar.

5.§.3 Comparison between the SPH and Beam Scheme Results

In this subsection, the current findings will be briefly compared with those obtained by Ball (1992, hereafter B92). But first, a short review of the methodologies of both techniques will be given. In B92, the bar potential used in the beam scheme method was derived from an I-band image like the one used in Chapter 4. In fact, the actual potential derived from the image was that of a triaxial bar whose geometrical properties were derived from fitting elliptical isophotes to the surface photometry of the stellar bar. Similarly, the surface brightness distribution of the bar was determined by separating the light contribution of the disk from the overall observed brightness profile. The disk was fitted by an exponential law with a scale length of 51.4″ (2.7 kpc) (compared to the 60.3″ or 3.2 kpc found in Chapter 3). In his simulations, B92 used a Generalized Mestel disk (GMD) (Mestel 1963, Hunter et al. 1984) because it matched the nearly flat outer rotation curve of the galaxy. One final component, which was also used in a set of simulations, was an oval distortion of the GMD.

As shown in the last chapter, the potential used with the SPH code was derived from the Fourier decomposition of the I band image which has been convolved with a scale height function described by Equation 4.7. The Quillen et al. (1994, hereafter Q94) method is resourceful in terms of obviating the need to derive individual elements that are subsequently added piecemeal to create a potential. The observed bar and spiral components, along with other unforeseen terms, are automatically incorporated into the derivation of the gravitation field and the scale height function actualizes a realistic non-zero thickness disk of a galaxy.

Of the three sets of models constructed by B92, the one created from a bar + oval distortion potential best reproduced the observed structure and kinematics of the gas in NGC 3359. The pattern speed used to create these models was 33.9 km s^{-1} kpc^{-1}. The comparison made between the most successful representative of the set (cf Fig 3 of B92), and Models B-D yielded the following:

1) Morphologically both numerical simulation techniques are able to duplicate a bar region of lower gas surface density and the basic spiral features of the galaxy. The spiral arms of both methods show similar winding as observations for small radii. However the arms of the beam scheme are wound more tightly at larger radii than are the observed arms. It is unclear how the matching of the real and model arms were made by B92 but the agreement between the SPH model and real arms have been shown in the overlapping plots of this chapter. Furthermore the SPH models are better at reproducing the arms in two other aspects. First the arms start from the ends of the bar whereas those produced by the beam scheme begin about 1 kpc farther out. Second the angle between the beam scheme model arms and the bar arm transition is larger than those of the SPH simulations and observations. In general the fit to the gas morphology of NGC 3359 is better for the SPH models.

2) Kinematically the artificial rotation curves are in good agreement with the real one as are the velocity perturbations in the outer disk. The largest difference arising from comparing the velocity fields of the SPH and beam scheme models is within the bar region. In Models B-D bar streaming motions are clearly observable, especially in the western half of the bar zone. Such non-circular perturbations are not visible in the triaxial bar plus oval distortion models although strong streaming motions were reproduced by the bar-only models (cf Fig 7 of B92). It should be noted however that part of the reason why the models are smoother in the inner region for the beam scheme models is due to the convolution of the data with a larger simulated beam (~18″) than the one used here (15″).

The above results show that the SPH models are at least comparable, if not better than those produced by Dr Ball. However the discrepancy between the pattern speeds for each method remains to be answered. As mentioned previously B92 used $\Omega_p = 33.8$ km^{-1} kpc^{-1} for the best models. This value is 15.5% slower than the bar pattern speed derived here and more than twice the angular frequencies of the spiral pattern. One other major factor which controlled the output of B92's results was the bar mass. But this physical quantity influenced the non-axisymmetric structures within and slightly beyond the ends of the bar, not the extent or shape of the spiral arms. Furthermore, B92 also stated that the mass was also strongly dependent on the pattern speed. Mass is not a free parameter in the SPH simulations since they are response models in a fixed potential. Hence, the emphasis on Ω_p is justified in this discussion.

Although various pattern speeds were tried to improve upon the results of the model fit to the observed data, B92 found that only minor adjustments could be made. Slowing the pattern speed by as 5% produced a gas bar which was 40% longer than the real one. Conversely, increasing Ω_p by a large increment placed the CR within the bar (note that B92's estimated bar radius is $5''$ longer than the one used in this dissertation) in addition to forcing the spiral arms to become too tightly wrapped (and eventually form into a ring).

The results of this chapter have shown similar behavioral changes with pattern speed. The range for the SPH models, however, are larger. The beam scheme and SPH methods are variations of the same process of computing the gasdynamics in the galaxy and the results should be similar to one another. Hence, the variations between the results produced by the two methods must lie elsewhere. The primary suspect then is the potential for each modeling scheme. The one which was used by B92 comprised of two components, which is probably a fair assessment of the general properties of the underlying potential. However, the geometrical properties of the triaxial bar and the oval distortions are only approximations of the structures themselves. In the potential derived here, such generalizations are limited to fewer terms (e.g., the disk scale length). The combination of various building blocks for the potential is also avoided in the Q94 method. Thus, the arbitrary use of an oval distortion to provide the tangential forces to drive the spiral structure is not needed. It would also be interesting to see if other components could be added, or used, to replace the oval distortion (i.e., a spiral potential like that used by Lindblad 1996). Thus, it is possible that the actual potential of NGC 3359 may be composed of more than two components. The use of the Q94 method will at least contain certain aspects of the additional elements. In summary, the deficiencies which stem from the B92 are ameliorated by [illegible] of the use of a more natural derivation of the underlying potential.

5.6 Conclusion

The structural and kinematical properties of the gaseous content of NGC 3359 have been modeled with the potential obtained from Fourier analysis and the smooth particle hydrodynamical code. The procedure and results are improvements upon those obtained by B92. The SPH models are better at (1) producing spiral arms which attach to the ends of the bar, (2) the turning of the arms at the attachment points, and (3) duplicating the streaming motions near the bar in the velocity fields. Other features are in agreement with those of B92.

However, the most important conclusion of this chapter *as well* as this thesis is that NGC 3359 exhibits two pattern speeds. The morphology of Model A clearly does not show proper gas response outside the bar region. The arms are tightly wrapped and completely fail to match the fairly open spirals of the real galaxy. Kinematically, the rotation curve is credible only within the area of the bar. These results were derived from using the bar pattern speed of 39.17$\mathrm{km\,s^{-1}\,kpc^{-1}}$. To model the gaseous density and velocity field of the spiral component well an acceptable value somewhere between $\Omega_p = 10.00$ to about 16.00 $\mathrm{km\,s^{-1}\,kpc^{-1}}$ should be used. A value from this range will suffice to properly explain the spiral pattern speed that is connected to the bar pattern speed via non linear coupling. In Figures 5.25 to 5.28, the elliptical orbits of the x_1 stars extend beyond the ends of the bar. And although the orbits do lend bar support, it should be kept in mind that they also shape the physical structure of the bar. The deprojected images of the bar (Figure 4-3) show the isophotes are not elliptical but become more rectangular at large radii. This result is exactly what has been shown in Chapter 4 (and in part, by Athanassoula 1992a) where the x_1 and the 4:1 orbits have similar structures at larger energies using the fast pattern speed. Recently, Patsis et al. (2003) and Skokos et al. (2002) observed similar behaviors in their modeling of orbits in 3-D bars. Rectangular like orbits of the x_1 depend mostly on the pattern speed: fast bars produced more elongated rectangular orbits.

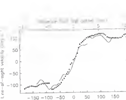

Figure 5-29 Hybrid combination of the rotation curves of Model A and Model C

Thus in order to conform to what is observed in the real galaxy the study of stellar orbits and gasdynamics must first agree with one another This can only be done by incorporating a fast bar with a slow spiral pattern via non-linear coupling A definitive coupling between which resonances of the two structures will be withheld here as the resonances can be close to one another not to mention that the models show similar responses and so I am unable to say which is the "best" It is however encouraging to see that the end-of-the-bar and ILR coupling (Model C) scenario is a viable option This case is in a way related to the best model produced by B92. Within the bar region, the gas can be driven by the forces produced by the structure itself, while just beyond the ends of the bar the spiral potential begins to dominate the outer disk, much like the role of the oval distortion in B92 In Figure 5-29 a hybrid combination of the two rotation curves of Model A and C is shown and supports the combination of the present resonance coupling scenario Finally the combined plot of the orbits for Model A (within the bar region) and C (outside the bar) are shown in Figure 5-30 This figure is a good representation of the structure of the central family of orbits within NGC 3359

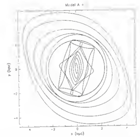

Figure 5-30 Combination of the x_1 orbits for Models A and C. This is the best theoretical representation for the (inner 5 kpc) morphology of the galaxy. Orbits from Model A and C are in blue and red respectively. The black circle denote the extent of the stellar bar

CHAPTER 6
CONCLUSIONS

6.1 Summary of Previous Chapters

The important results obtained in the past four chapters will be summarized in this chapter. The information is then combined to explain the physical conditions of the nucleus, the bar, and the disk of NGC 3359.

6.1.1 21-cm Data Observations

The 15″ and 30″ resolution data cubes which were obtained from the WSRT in Holland are the vital pieces of information of the galaxy upon which this research is centered. The continuum field of the galaxy, at 14.03″ × 12.80″ (0.75 kpc × 0.68 kpc) resolution, showed the primary source of radiation is the central part of the bar (specifically within the two major giant SF regions located immediately NE and SW of the nucleus). Within the area, a peak temperature value of 4.1 K (11σ) was detected. The nucleus itself is not a strong emitter of the 21 cm continuum radiation. Outside the bar region, the largest 21-cm continuum emanates from the area of star formation located ~ 94″ (5 kpc) northeast of the center, with a peak intensity value of 0.95 mJy (3.2 K). The available data cannot differentiate between the thermal and nonthermal components of the emission. However, the positions of the detectable radiation suggests that the majority of the continuum field is composed of thermal photons emitted by the intense SF regions though synchrotron radiation from supernovae cannot be discounted.

The global distribution of the H I gas is mostly symmetric about the center. The gas content of the bar region is lower than the surrounding pseudo-ring. The maximum *azimuthally averaged* surface density value, 12 $M_\odot$ pc^{-2}, is located at $r = 68''$ (3.6 kpc); the H I scale length of 56.3 ± 1.9″ (3.0 ± 0.1 kpc) was obtained in Chapter 2. The total extent of the gas, as determined from the 30″ data, is $r = 450''$ (24 kpc) or 2.1 times that of the photometric scale length (RC3). The total H I and dynamical mass are 5.6×10^9 and 1.0×10^{11} $M_\odot$ respectively.

The kinematical properties of the galaxy are shown in Table 2-2. It is not surprising to see strong non circular velocities associated with streaming motions along the bar and spiral arms. However, the interesting kinematical signature is the presence of double peaks seen in the rotation curve of the galaxy. The velocity drop-off between the two maxima are attributed to the large streaming motions associated with the spiral density waves. Owing to this fact, the tangential component of the observe radial velocities become smaller and produce the observed double-peak phenomenon.

Lastly, the gas companion of NGC 3359 found by Ball (1986) was also detected. The major axis core size and dynamical mass of the object are 2.8 kpc and $1.3 \times 10^8\ M_\odot$ (section 2.5). Given these physical attributes of the satellite and its location from the center of the galaxy (47 kpc), it is more than likely that the object exerts no significant dynamical effects on the galaxy. However, a faint, extended bridge between the satellite and the northern H I gas arm can be seen in the 60″ image convolved from the 30″ data.

6.1.2 Optical and NIR observations

Stellar images of NGC 3359 showed two wavelength-dependent trends. The first is the isophotal twist within the bar region, the position angle of the fitted isophotes increased with shorter wavelengths. The second is the observed increase in exponential scale length with redder images. Dust was detected around the bar region, predominantly near the center of the structure. Patches and filaments of the interstellar grain criss-cross each other, most noticeably in the southern end. Such irregular dust morphology may be due to the young bar.

The most intense H II regions lie along the Hα bar as well as the ends of the bar. Prominent SF regions appear to affect the kinematics of the surrounding gas near their locations. In addition to having high velocity dispersions, the regions also correspond to the peaks observed in the residual velocity field map. This combination hints at gas motions which may be flowing not only in the plane of the disk but also vertically. The cause for such out-of-plane motions may be attributed to outflows caused by either stellar winds from the central OB stars or radiation pressure from the same objects (Relano et al. 2003). Unfortunately, the current SPH code does not simulate star formation and is only limited to two-dimensional modeling.

6.1.3 Stellar Orbits and SPH Simulations

The bar of NGC 3359 is best represented by a fast bar. To construct a bar model which matched the observed data, a bar pattern speed of 39.17 km s^{-1} kpc^{-1} was required. The build-up of stable x_1 family of orbits,[1] showed that the structure could not extend beyond the 6:1 resonance of the galaxy. In fact, the boxy isophotes near the ends of the bar suggest the presence of an inner 4:1 resonance at this region. This scenario fits perfectly with a bar ending near the 2.3 kpc radius, which is the adopted bar radius.

However, the gas dynamical model which rotated with the same angular frequency value as the bar (Model A of Chapter 5) failed to duplicate many of the features seen in intensity maps of either the 21 cm and Hα data. To produce spiral arms which show similar pitch angles as the observed, a model with a slower pattern speed was required. The best gasdynamical models have Ω_p values between 10.00 and 15.52 km s^{-1} kpc^{-1}. Surface density maps and the velocity fields of these models are qualitatively similar to the morphology and kinematics of the real gas. In summary, these slow rotating spiral pattern models are to produce the basic morphology of the arms. Similar results have also been found by Kranz et al. (2001, 2003).

6.2 Examination of the Central Region of NGC 3359

The center of NGC 3359 is perhaps the most mysterious region of the galaxy. There is no noticeable bulge component, as evidenced by the isophotal analysis of the stellar images in Chapter 3. A hard x-ray source near the nucleus has been observed by the Roentgen satellite (ROSAT). The color index images (as well as Figure 3-6) show that the nucleus of the galaxy is covered in dust. Braine & Combes (1992) estimated the H$_2$ mass within the nucleus to be approximately 2.5×10^7 M$_\odot$. The nucleus lacks any central Hα emission, the H I density of the core is also low as compared to the surrounding pseudo-ring. SPH gas particles naturally drift into the center of the models after being shocked and stay there hence analyses of the nuclear region of the models offer no further insight to the nature of the nucleus Clearly high resolution, interferometric CO observations are needed for that part of the galaxy Comparisons between Hα and CO data (and dust) are more appropriate for the region and for the investigation of star formation

---

[1] Although chaotic orbits are known to support the bar structure also (e.g. Patsis et al. 1997) they were not considered here.

6.3 Physical Conditions of the Bar and the Surrounding Zone

The ionized hydrogen gas bar leads the stellar bar in the direction of rotation by approximately 18° This large difference is real and cannot be caused by projection effects The cause for the discrepancy is given in the subsection 6.3.1 The adopted length of the bar is $86''$ (4.6 kpc) as determined by Aguerri et al (1998) There is no H I gas bar of which to speak, although two knobby features can be observed near the ends of the Hα bar Color index maps show the bar and its surrounding neighborhood to be reddish in color Dust and the steep inner abundance gradient (Martin & Roy 1995 hereafter MR95) are major contributors to the interstellar reddening

Much of the 21 cm radio continuum coincides with the intense H II regions which lie along the Hα bar and suggests that the emission is thermal in origin although nonthermal synchrotron radiation from supernovae cannot be entirely discounted Measuring the spectral index of the region would resolve the issue However additional data, such as 2- and 6-cm observations, are needed to construct the spectral index.

The gas surface density is lower within the bar zone as compared to the surrounding pseudo gas-ring This feature was reproduced by the SPH models B and C The H II gas of the Hα bar is highlighted by three of the most intense SF regions within the galaxy (Figure 3-7) the deprojected distances of the two strongest emission peaks are located $12\farcs2$ (648 pc) NE and $15\farcs5$ (825 pc) SW of the galactic center, respectively The southern half of the bar is indeed brighter (Figure 3-10) although it is unclear as to what the cause may be Dust will play a factor and the irregular distribution of the material caused by the young forming bar (MR95), is conspicuous in various stellar images

6.3.1 Dust and Star Formation in the Bar

Classical linear dust lanes as seen in other galaxies (e.g NGC 1300 1365 and 7479) do not exist in NGC 3359 The most distinguishable region of dust lies in the

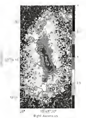

Figure 6-1 Contours of the broadband Hα image plotted on the J-K color map. The contour levels are, in arbitrary flux units, 150 × (5 15 80 100)

southern half of the bar (Figure 3-6) where a dust lane can be seen to start from the end of the bar and criss-cross the major axis of the structure before ending near the galactic center. As dust lanes are expected to be locations of shocks, slices were taken perpendicular to the bar and through the regions. From the beam smoothed data velocity jumps up to 50 km s^{-1} were observed. Higher resolution data should provide us with a better estimate of the true values.

The overall dust distribution is best seen in the color index image of Figure 3-12 and again in Figure 6-1 where the Hα image has been added as overplotted contours. The location of the two strongest H II regions in the galaxy (labeled 1 and 2, cf. Figure 3-7) are obscured by extinction to a lesser degree than others along the bar. Of more importance are the locations of the star formation zones in relation to the dust region of the bar. Figure 6-1 shows that the H II regions lead the dust in the sense of rotation. The effects are caused by the passage and compression of gas in the shocks and its subsequent collapse and formation of stars that occur downstream. This suggests that the azimuthal streaming motions of the gas may be high–a possibility enhanced by the fact that the bar is still forming and that the gas is circulating in elliptical orbits within the region (Friedli & Martinet 1993). Let us assume that the largest (projected) displacement between the H II regions in the bar and the dust lanes (lying along the major axis of the stellar bar) is 18°. Then, if both features have the pattern speed of the bar and accounting for projection effects, it can be shown that the maximum onset time for star formation must be less than 10^7 years.

Dust lanes were also simulated in the SPH models and were seen in some of the snapshots taken. However, the central region of the models are limited to low resolution as the initial disks were populated homogeneously with gaseous particles. Although inflow of particles toward the center was observed during the simulations, the models, constructed mainly to investigate the spiral structure, cannot be used for a detailed comparison with the observed dust distribution. Nevertheless, a nonlinear perturbation establishes the main characteristics of a bar (such as the location of corotation) within a few pattern rotations (Englmaier & Gerhard 1999; Patsis & Athanassoula 2000). However, the bar of this galaxy is relatively young. Therefore, there could be deviations of the modeled dust lanes from the observations as well.

6.3.2 Kinematics of the Bar Region

Individual discussion of H I and H II gas kinematics, as well as their comparisons have been covered in Chapters 2 and 3. The flow pattern of the SPH models (Figures 5-17, 5-26, and 5-28) clearly show the elliptical streamlines of the gas within the bar region. Such non-circular motions show up conspicuously in the velocity residual field of the galaxy. Indeed, by subtracting the best circular model from the observation deviations up to 28 km s^{-1} kpc^{-1} (in the plane of the disk, beam-smoothed) were observed. In the bar region, the largest velocity residuals of the real data reside in the western side. This feature was also reproduced successfully, as shown by the stronger bending of the isovels on that half of the model velocity fields (e.g. Figures 5-18).

6.4 Environment and Structures of the Spiral Arms and Disk

The radial distribution of the H I gas is approximately 7.2′ (23 kpc) in radius or twice that of the optical disk (21.7″ in blue magnitude, RC3). This is also the extent of the Hα emission. The main H I disk is larger than the optical disk by nearly 20% and its edge is relatively sharp. Two pure gas arms, originating from the eastern and western ends of the main disk, extend the H I disk out to the maximum radius. Owing to the limited extent of the gravitational potential extracted from the I band stellar image, these outer spiral entities could not be modeled. It would be very interesting to see whether a successful gas model created in the future requires an additional component and/or another pattern speed to produce the outermost gas arms.

Morphologically, the atomic hydrogen distribution has a grand design appearance and is less asymmetric than the ionized gas. The global symmetry of the H I gas is apparent in Figure 2-8. The southern part of the western arm contains more SF regions, thereby making the Hα field asymmetrical. The eastern Hα and stellar arm fragments into smaller individual arms in the northern half of the galaxy. This phenomenon led Elmegreen & Elmegreen (1982, 1985) to classify the galaxy as a multi-arm system. On the whole, the arms were modeled well by the SPH simulations that rotated with a spiral pattern speed within the range of 10.00 to 15.62 km s^{-1} kpc^{-1}.

The color difference maps of Chapter 3 show that the arms are also somewhat reddened owing to the presence of dust regions. These are readily observable in the R−I map and more so in Figure 10 of Rozas et al. (2000a). There is also an additional reddening factor caused by the diffuse component of the Hα emission that covers the entire optical disk (Rozas et al. 2000a); the wavelength of this emission overlaps the passband of the I-band filter.

Azimuthally averaged radial profiles of the H I and H II surface density maps show peaks just beyond the bar, where the pseudo-ring is located. At larger radii, the radial distribution of both elements exponentially fall off with scale lengths of 3.0 and 1.9 kpc (Rozas et al. 2000a) for H I and H II respectively.

The positions of the cold gas correspond well with the ionized gas. There is interest in whether the density peaks of the two gases should overlap. However, two partly

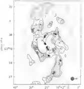

Figure 6 2 Density comparison between the ionized (grayscale) and atomic (contours) hydrogen gases in NGC 3359 The levels of the isodensity contour lines are as follow *dotted* = 6 5 and 9 0 *blue* = 11 0 and 13 0 *green* = 15 0 and 17 0 and *red* = 19 0 and 21 0 $M_\odot$ pc $^{-2}$ See Section 6 1 for explanation of the thick circle located SE of the galactic center The beam of the 21 cm data is given at the bottom right corner of the figure.

contradictory effects make the solution to the problem difficult to obtain On the one hand, ionization of the H I gas should reduce its column density near the H II regions But at the the same time UV photons from hot stars in the area will dissociate the H_2 molecules around the star forming zones thereby increasing the H I column density This second effect has been noticed by Zurita et al (2002) for NGC 157 A preliminary and cursory inspection of Figure 6-2 showed that the H I and H II peaks do not overlap. However the resolution difference between the two data is an order of a magnitude and thereby make the comparison very crude Clearly 21 cm data of greater detail (i e those obtained from the A or B configuration of the VLA) should be compared with the Hα data to produce a more meaningful and valid analysis

Overall the flow of gas within the outer disk of NGC 3359 is circular except near the spiral arms where large perturbations caused by spiral density waves instigate streaming motions Non-circular, beam-smoothed velocities as high as 60 km s $^{-1}$ are observed near the spiral arms Slowly rotating gas models produced similar effects near the simulated arms. Along the minor axis, both species of gas under study show strong radial inflow ($\sim$40 km s^{-1}) from the eastern arm.

6.5 Final Words

By far, the most important result of this research is that NGC 3359 has two pattern speeds. This single fact makes the galaxy extremely interesting for further study as it could open up an avenue for further discoveries of separate bar and spiral speed systems (not to mention new insights and concepts for the field of galactic astronomy). Indeed the galaxy cannot be unique in this distinguishing characteristic. But only a few galaxies have been conjectured to have two pattern speeds. Even fewer have as much evidence to support the claim as does NGC 3359.

CHAPTER 7
SUGGESTIONS FOR FUTURE RESEARCH

While many of the basic questions such as the mass, distribution and general kinematical and dynamical properties have been answered, there remain some issues that should be addressed. The following are some directions for possible future research that would make the study of NGC 3359 more complete.

7.0.1 Observations

Since the primary aspect of this research concerns the kinematics of the gases within the galaxy, the most important observation that is required for NGC 3359 currently is higher resolution and better sensitivity mapping of the H I gas. Obtaining the A and B-array VLA data would allow for greater detailed study of H I gas clouds near the H II regions. Such observations would also aid in determining whether there are similar signs of out-of plane motions near the intense SF zones for the atomic hydrogen gas. In addition, the strong non-circular velocity perturbation across both the bar and the spiral arms can be investigated more accurately.

It would also be quite beneficial to obtain stellar kinematics from the new generations of imaging instruments such as SAURON. Such data would provide the key comparison data for the study of stellar orbits as well as N-body models.

As it has been shown in previous observations, the galaxy produces only weak CO emission. Combined with the low H I density and a lack of H II region in the center, the nucleus of this galaxy is still largely a mystery. The color-difference maps have shown that the area is deeply veiled in dust. Deeper observations of the galactic center with the Hubble Space Telescope's NICMOS (Near Infrared Camera and Multi Object Spectrometer) camera is needed to study this region in subarcsecond resolution.

Finally, in order to obtain separate the radio continuum into its thermal and nonthermal components, (high resolution) observations at 2, 6 and 20 cm are needed.

This will allow for reliable estimates of the spectral index as well the rates of star formation and supernovae.

7.0.2 Numerical Simulations

As this galaxy contains two pattern speeds, the present SPH codes that are known to exist will not be adequate to perform the proper gas flow within the galaxy. Thus, the most pressing issue at hand is the construction of a new hydrodynamical algorithm that can account for multiple pattern speeds. Self-gravity as well as star formation should be included into the program as both will be important near highly compressed and dense gas regions. Furthermore, the models should be three-dimensional. Not only will this help to answer whether vertical gas motions can indeed be observed, but the tentative existence of "beards" seen in the P V plots could also be resolved. It should also be determined whether a halo component is needed and if so, how much. Certainly the various parameters inherent to hydrodynamical codes (such as viscosity coefficients and the bar growth rate) should be tested in future runs. To further increase the resolution of the models, more particles should also be included. Finally a similar statement can also be made for a new code that determines the orbits of stars in a model rotating at two different angular frequencies.

Further refinement of the models can also be made by improving the working potential. For instance, longer wavelength IR images of the galaxy could improve the approximation of the underlying gravitational field. In addition simulations with disk inclination, vertical scale height, and M/L ratios other than the ones used in this dissertation should be utilized.

APPENDIX A
21-CM ATOMIC HYDROGEN EMISSION

Atomic hydrogen in the ground state is the basic form of the most abundant substance in the Universe. Its spectral line detection was first made by Ewen & Purcell in May 1951 after van der Hulst (1945) predicted its existence six years earlier. In the ground state, the electron of the atom exists in hyperfine structure whereby its spin can be either parallel (total angular momentum $F = 1$) or antiparallel ($F = 0$) to the spin of the proton. This gives two possible electron energy configurations. Slightly more energy is required for the electron to be in the parallel state due to the repulsion between the proton and electron than the antiparallel state. The energy difference between the two states is approximately 6×10^{-6} eV (corresponding to a photon of frequency 1.4204 GHz or 21.105 cm in wavelength).

Collisional excitation and de-excitation between H I atoms is the main method in which the electrons acquire their hyperfine states (although absorption and emission of 21-cm photons also contribute). In a typical ISM environment with density $N = 1$ cm^{-3} and $T = 100K$, the hydrogen atoms have a mean free path (l) of 1×10^{15} cm while moving at speeds of $10 - 15$ km/s. The time between collisions is therefore $l/v \approx 10^{10}$ s. Thus, excited H I atoms undergo collisional de-excitation about every 300 years. This rate is much faster than the spontaneous emission of 21-cm photons by isolated atoms. The probability for such transition is given by the Einstein coefficient A_{21} whose value is 2.86888×10^{-15} s^{-1} or once every 10^7 years. Nonetheless, radio telescopes will observe photons produced by both processes as there are vast abundances of interstellar hydrogen along the line-of-sight. Additional 21-cm line emission can also originate from the warmer (above 1000 K) gas of near star forming regions.

One can apply the Boltzmann equation to obtain the expected atomic population numbers of the two energy levels

$$\frac{n_2}{n_1} = \frac{g_2}{g_1} exp(\frac{-h\nu}{kT_s})$$

where g is the statistical weight of the energy level and the ratio g_2/g_1 is equal to three. The spin (nearly identical to kinetic) temperature of the gas is given by T_s. At $T_s = 100$ K $\frac{-h\nu}{kT_s} = 7 \times 10^{-4}$, $e^{-h\nu/kT_s} = 0.9993$ and so $n_2 \simeq 3n_1$. Furthermore, the observed intensity of the gas as represented by the Planck function $B_\nu(T_s)$ approaches the Rayleigh Jeans limit for the case of $(h\nu/kT_s \ll 1)$ so that

$$B_\nu(T_s) = \frac{2kT_s\nu^2}{c^2}$$

The observed intensity can also be given by the equation of radiative transfer

$$\frac{dI_\nu}{d\tau} = S_\nu - I_\nu \tag{A.1}$$

where the source function S_ν, is related to the absorptivity χ_ν and emissivity η_ν of the gas by

$$S_\nu = \frac{\eta_\nu}{\chi_\nu}$$

In addition, the optical depth τ is defined as

$$\tau = -\int \chi_\nu ds$$

The formula for the absorption coefficient is

$$\chi_\nu = n_1 B_{12}(1 - e^{-h\nu/kT_s})(\frac{h\nu}{4\pi})\phi_\nu$$

The Einstein coefficient B_{12} denotes the probability of an upward stimulated transition by the lower level atoms through 21-cm photon absorption. ϕ_ν is the line profile of the gas and is normalized to unity over all frequency. The fact that the Einstein coefficients are related by

$$A_{21} = (\frac{2h\nu^3}{c^2})B_{21} \quad \text{and} \quad g_1 B_{12} = g_2 B_{21}$$

enables the optical depth to be represented by

$$\tau_\nu = \frac{g_2}{g_1}\frac{A_{21}}{8\pi}\frac{c^2 h}{\nu k T_s} N_1 \phi_\nu$$

in the limit of small $(h\nu/kT_s)$. N_1 is the integrated column density of the lower level hydrogen atoms ($N_1 = \int n_1(s)\,ds$). A_{21} and B_{21} are spontaneous and stimulated emission coefficients respectively. Since $n_2 \approx 3n_1$, it follows that $N_H = N_2 + N_1 = 4N_1$. Therefore

$$\tau_\nu = \frac{g_2}{g_1}\frac{A_{21}}{32\pi}\frac{c^2 h}{\nu k T_s} N_H \phi_\nu \qquad (A.2)$$

Inverting Equation (A.2) and integrating over all frequency enables us to obtain the column density value along the observed line-of-sight

$$N_H = 3.88 \times 10^{14} \int_0^{+\infty} T_s \tau_\nu d\nu$$

However, radio receivers typically measure the brightness temperature T_b of the emitting region. By definition

$$T_b \equiv (\frac{c^2}{2k\nu^2}) I_\nu$$

Assuming a uniform medium with no background source and constant S_ν, the transfer equation can be integrated to give the observed intensity I_ν in Equation A.1 as

$$I_\nu(0) = S_\nu(1 - e^{-\tau_\nu})$$

As the gas is typically in local thermodynamic equilibrium, $B_\nu(T_s) = S_\nu$ and so

$$I_\nu(0) = \frac{2kT_s\nu^2}{c^2}(1 - e^{-\tau_\nu})$$

Thus the brightness temperature is related to the spin temperature by

$$T_b = T_s(1 - e^{-\tau_\nu})$$

Since H I is assumed to be optically thin in most cases

$$T_b = T_s \tau_\nu$$

Conversely, $T_b = T_s$ for the optically thick case

Due to the large scale variation in velocities caused by differential Galactic rotation, the profile lines of the hydrogen atoms will be Doppler shifted. Consequently, the emission lines will change in frequency. The end result of this effect is to cause the optical depth of neutral hydrogen to be small. Mihalas and Binney (1981) demonstrated that by using typical Galactic values of $N_H = 10^{21}$ cm^{-2} and a Doppler shift of $\delta v = 10$ km/s, $\tau_\nu \approx 0.3$ at the line center. This is probably an overestimate as the line-of-sight will not contain hydrogen clouds along its entirety. Therefore it is reasonable to assume that the 21-cm line is optically thin in most cases. With this assumption, the total neutral hydrogen column density can be expressed in terms of the brightness temperature as

$$N_H = 3.88 \times 10^{14} \int_0^{+\infty} T_b d\nu$$

If the customary units of kilohertz and km s^{-1} are used, then

$$N_H = 1.82 \times 10^{18} \int_0^{+\infty} T_b dv \qquad \text{(A.3)}$$

after applying the factor $10^3 \times \nu/c$. The total H I content can be found by integrating N_H over the surface area of the emitting region encompassed by the solid angle Ω. The total H I mass of the system is therefore

$$M_H(M_\odot) = 2.36 \times 10^5 D^2 \int_0^{+\infty} S(v)dv \qquad (\tau \ll 1) \qquad \text{(A.4)}$$

where D is the distance to the source in unit of Mpc and the flux density is given by

$$S = \frac{2k\Omega\nu^2 T_b}{c^2}$$

The flux density is measured in the unit of Janskys where 1 Jy = 10^{-26} W Hz^{-1} m^{-2}. However, Equation A.3 becomes

$$N_H = 1.82 \times 10^{18} \int_0^{+\infty} T_b \left(\frac{\tau}{1 - e^{-\tau}}\right) dv$$

for regions where the optical thickness is considerable and cannot be neglected.

APPENDIX B
FUNDAMENTAL CONCEPTS OF THE RADIO INTERFEROMETER

The Westerbork Radio Synthesis Radio Telescope (WSRT) is operated by the the Stichting ASTRonomisch Onderzoek (ASTRON) or in English, the Netherlands Foundation for Research in Astronomy (NFRA). The telescope is an aperture synthesis interferometer consisting of 14 antennae in a linear array set on a 2.7 km East-West line. Each antenna is 25-m in diameter, equatorially mounted and has an f/D ratio of 0.35. Ten of the 14 antennas (labelled 0-9) are on fixed mounting and are separated by 144 meters apart from the next one. The remaining four, labelled A, B, C, and D and set in a 2 × 2 array, are movable along two railtracks. One track is adjacent to the fixed array and 300 m long. The other is 80 m long and 9 × 144 m eastwards. The movable dishes thereby give the telescope effective baselines that range from 36 m to 2.7 km. In the spectral line observing mode, the WSRT becomes an aperture synthesis array with 91 baselines and is 2.7 km in length.

The long wavelength nature of the atomic hydrogen forbidden lines, large telescopes are required for observing H I sources. The first 21 cm line measurements were made with single dish telescopes at (inherently) low angular resolution. The proliferate use of aperture synthesis telescopes during the 1970s produced radio data of greater detail such that images of less than one arcsecond resolution are now achieved. The antenna dishes of these telescopes are set in an array of predetermined configuration to artifically produce a single antenna dish of much larger size (up to kilometers in diameter). Thus, a single large aperture telescope is *synthesized* (aperture synthesis) by numerous smaller ones.

When the telescope observes distant radio sources, the signals from each pair of antennae are measured for mutual coherency. By measuring the spatial correlation of gnal of the received signals in terms of the spacings (baselines) between the pairs of antennae, the Fourier transform of positions and intensities of the source are imaged. This process of measuring the coherence function (visibility) between a pair of antennae forms the basis of interferometry. The operating pair of antennae is called an *interferometer*. The resolution of the telescope is inversely dependent upon the largest baseline (B) set by the array configuration. The greatest detail the telescope can image is defined by λ/B where λ is the wavelength of observation. However, the sensitivity of the whole array is less than an equivalent size single-dish antenna because the total combined area of the antennae in the array is appreciably less than that of the aperture synthesized.

In an array of N antennae, there can be up to N(N−1)/2 interferometers or baselines. The signal received from each interferometer baseline form an interference pattern similar to light passing through double slits. Multiplying the data from each pair of elements in the array together forms multiple interference patterns that reflect the spatial intensity distribution of the sources. Each baseline covers only one component of the complete Fourier series interference pattern made by the received signals of the whole array. Therefore numerous baselines are required to measure a large number of components that will yield an image of the radio emitting source. In an given instant, N(N−1)/2 components are measured. But aided by the rotation of the earth, the number of baselines available increases significantly and thereby allow the telescope to gather (hundreds of) thousands of visibility points during an observing run.

As mentioned above, there are up to 91 simultaneous interferometers available to observe the source when all fourteen antennae of the WSRT are operational and in use. Information about the intensity and position of the sources in the field of view is extracted by determining the spatial coherence function (complex visibility) from the source radio emission observed by antennae of the array.

Before the process of obtaining the visibilities and ultimately produce the image of the observed source is detailed, three assumptions should be made in what follows. First, the distance to the observed source (d) is assume to be far away such that $d \gg B^2/\lambda$. No third dimension of the source can be obtained and so the surface density (brightness) of the object is the only measurable quantity. Second, the antennae receive only the

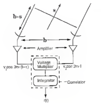

Figure B-1 Block diagram of a two-element interferometer $\tau = \mathbf{b} \cdot \mathbf{s}/c$ is the geometrical delay

source radiation and no other wavefronts The electric field produced by the radio source is the sum of Fourier series that is measured by the array when the individual Fourier components observed by interferometer are combined Lastly the measured field will be considered as scalars for simplicity

The block diagram in Figure B-1 will be used to describe how an ensemble of two-element interferometers produce images from the correlated signals from the antennae Consider the case of two antennae (separated by baseline length b) that are pointed toward the radio source (indicated by the unit vector s) One antenna will receive the incoming wavefront from the source at a time ($\tau = \mathbf{b} \cdot \mathbf{s}/c$) later than the other Each antenna will produce a response at the receiver when the signal from the electric field of the observed source is detected The responses from the antennae are passed on to be amplified combined and time averaged at the correlator The output of the correlator for the signals (in terms of the radio brightness integrated over the sky) can be expressed as

$$V_\nu = \int I_\nu(s) A_\nu(s) \exp(-2\pi i \nu \tau / c) d\Omega$$

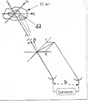

Figure B-2 The *(u v w)* and *(l m,n)* coordinate systems.

where

$I_\nu(\mathbf{s})$ is the radio brightness (or intensity) of the source at frequency ν

$A_\nu(\mathbf{s})$ is the normalized reception pattern of the interferometer dishes and

$d\Omega$ is the solid angle from that the signal is received

In terms of the baseline spacing **b** and source position vector **s**

$$V_\nu = \int I_\nu(s) A_\nu(s) \exp(-2\pi i \nu \mathbf{b} \cdot s/c) d\Omega$$

The output V_ν is a function that depends only on the baseline vector **b** and is called the spatial coherence function. It is more commonly known as the visibility and is all that can be measured by the telescope from which $I_\nu(s)$ must be extracted.

The coordinate system used to measure the visibilities is illustrated in Figure B-2 The u and v axes point east and north respectively while w point towards the phase reference position (i.e. center of the field of view) and is usually insignificant as most measurements are confined to the u-v plane The baseline vector (**b**) between two antennae is (u, v, 0) and is measured in dimensionless values of the wavelength of observation. The position which is pointing toward [illegible] is given by the direction cosine $(l, m, \sqrt{1-l^2-m^2})$. The visibility equation in [illegible] plane can be written as

$$V(u,v,w) = \int_{-\infty}^{+\infty}\int_{-\infty}^{+\infty} I_\nu(l,m)A_\nu(l,m)e^{-2\pi i(ul+vm+w)}\frac{dl\,dm}{(\sqrt{1-l^2-m^2})}$$

Usually the region of observation is small compared to the whole celestial sphere and the curvature of the sky plane is neglected. Thus, $A_\nu(l,m) \simeq 1$ and for each (i,j) antenna pair

$$V_{ij}(u,v,w) = \int_{-\infty}^{+\infty}\int_{-\infty}^{+\infty} I_\nu(l,m)e^{-2\pi i(u_{ij}l+v_{ij}m)}dl\,dm \tag{B.1}$$

and $V(u,v,w)$ is now referred to as the complex visibility since it is a complex variable whereas $I_\nu(l,m)$ is real. All the telescope has to measure is $V(u,v,w)$, the Fourier transform of I_ν.

For spectral line observations, visibilities at several frequencies $V(u,v,\nu)$ are observed to cover the complete radio emission from the source. By inserting a time delay (lag interval $\delta\tau$) in the data path, discrete frequencies are selected before the signals from the two antennae are correlated.

The observed visibility must be calibrated for its amplitude and phase in order to determine the true visibility because most of the data are corrupted before the signals from the antenna pair are correlated. This is performed by observing primary flux and secondary phase calibrators. The former is observed typically at the start and at the end of a run while the latter is observed more frequently to monitor the phase stability of the atmosphere and receiver. For the observations of NGC 4359, Dr. Broeils chose 3C286 and 3C147 as the calibrators used to determine the complex gain of each antenna. Formally, the observed visibility measured at time t is related to the true visibility by (Fomalont & Perley 1998)

$$\tilde{V}_{ij} = g_i g_j^* g_{ij} V_{ij} + \epsilon_{ij} + \eta_{ij}$$

where

$g_{i,j}$ is the antenna-based complex gains for antennae i and j and the asterisk denotes the complex conjugate

g_{ij} is the residual baseline-based [illegible]

V_{ij} is the true visibility that we want to [illegible]

ϵ_{ij} is a baseline-based complex offset and

η_{ij} is a stochastic complex noise and all terms are functions of time

Under normal circumstances ϵ and η_{ij} are negligible. The antenna-based complex gains are given by $g_{i,j} = a_{i,j}e^{i\phi_{i,j}}$ where $a_{i,j}$ and $\phi_{i,j}$ are the instrumental amplitude and phase of antennae i and j respectively. Likewise the residual amplitude and phase of the baseline gain, generally known as the *closure error*, is given by $a_{ij}e^{\phi_{ij}}$. Its value is near unity $[g_{ij} = (0.98 - 1.01)e^{i(\pm 1^{\circ})}]$. For a properly calibrated point source of known flux density (S) and position, the true visibility will be the flux density (S) of the calibrator. A point-like source is used for calibration so that the true visibility is constant for all baselines. Thus the amplitude (A_{ij}) and phase (Φ_{ij}) of the complex visibility is

$$A_{ij} = a_i a_j a_{ij} S$$

and

$$\Phi_{ij} = \phi_i - \phi_j + \phi_{ij}$$

A least-squares solution is used as the large number of baselines (N(N-1)/2) makes the pair of equations overdetermined at each calibration sequence (for $g_{ij} \sim 1$, that is the usual case). The amplitude and phase closure errors are readily solved as $a_{ij} = A_{ij}/a_i a_j S$ and $\phi_{ij} = \Phi_{ij} - \phi_i + \phi_j$. Typically, the errors should be less than 10%.

The data reduction software used to reduce the WSRT (u, v) data is AIPS. The actual calibration is performed on a continuum like channel (channel zero or CH0) rather than the line data. The channel covers the central 75% of the bandwidth of observation and therefore is much stronger in signal than the individual line channels. Once the proper calibration is performed on CH0, it is then applied to the narrow band channels. Due to finite bandwidth sampling and incomplete Fourier synthesis of all the incoming radiation, the Gibbs effect of ringing will be present owing to the truncation of the temporal (lag) cross-correlation spectrum (Laine 1996). To reduce the ringing, the Hanning smooth function is applied to the data on-line although at the cost of degrading the frequency resolution. Three consecutive channels are chosen such that the visibilities per channel are averaged with weights of 0.5 for the center channel and 0.25 for the adjacent ones. As mentioned, the frequency resolution is reduced in the new smoothed channels whose widths are now twice that of the original and so the total number of independent channels are reduced by a factor of two.

The initial stage of calibrating the data is editing. During this process, visibilities of the calibrators that render the complex gain of the antennae undeterminable are identified and, if uncorrectable, flagged (discarded). Factors that contribute to the useless visibility points include malfunctioning equipments, inclement weather, and data recording errors to name a few. Such corrupted data appear as noisy or discrepantly high or low values when the visibility points are plotted. After editing, antenna-based calibration of the calibrators is processed. The primary flux calibrator for CH0 is first solved for by using the Baars et al. (1977) coefficients of known and calibrated sources. Next, the amplitude and phase antenna gain solutions for the two calibrators are calculated. A list of amplitude and phase closure errors is also produced. Baselines with error values greater than the (user set) upper limits are investigated further and corrected or discarded. The process is repeated until the solutions are acceptable.

Using the antenna gain solutions table and the primary calibrator, the flux density of the secondary (phase) calibrator is subsequently determined. The gain solutions are then interpolated to create a calibration table that are applied to the sources. The spectral line data is calibrated by using the same calibration table that has been copied from the CH0 data to the line channels. The final calibration process is to compensate for the change in antenna gain with frequency that occurs in spectral-line data. This is performed by calibrating the bandpass with the primary (flux) calibrator whose spectrum is approximately constant over the frequency band. The calibrated (u, v) data are now ready to be Fourier transformed into the image plane.

The basis of creating images (or $I(l,m)$, the modified sky brightness) from the observed visibilities lies in the premise of the Fourier inversion of Equation B.1

$$I(l,m) = A(l,m)I(l,m) = \int_{-\infty}^{+\infty}\int_{-\infty}^{+\infty} V(u,v)e^{2\pi i(ul+vm)}du\,dv \tag{B.2}$$

The most practical method of transforming N visibility points (where N usually range in the tens of thousands) obtained from a radio telescope is to use the fast Fourier transform (FFT) technique. Direct Fourier transform (DFT) is also another viable method. However, the number of operations required for the FFT of N visibility points is of the order NlogN whereas DFT is over N^2. FFT requires the visibilities be mapped onto a rectangular grid of dimensions $x \times y$ "cells" where x and y must be in powers of two.

Because the sampling of the (u,v) plane by the array is limited and uneven, Equation B.2 can expressed as

$$I^D(l,m) = \int_{-\infty}^{+\infty}\int_{-\infty}^{+\infty} V(u,v)S(u,v)e^{2\pi i(ul+vm)}du\,dv$$

where $S(u,v)$ is the discrete sampling function of the source visibility at each (u,v) point. $I^D(l,m)$ is often referred to as the *dirty image* whose relationship to the desired source intensity is expressed by convolution equation $I^D(l,m) = I * B$. B is the synthesized "dirty" beam (the response of the array to a point source). Thus the beam determines how well I^D approximates I. The shape, as well as sidelobes of the beam made by the gaps in the finite (u,v) coverage, are controlled by weighting functions. Currently, the two in use are tapering and density weighting functions. They are applied to the calibrated data before the Fourier transformation. The tapering function is (u,v) radius-dependent as the values of the weights decreased from the center of the (u,v) field. Tapering the data effectively reduces the importance of the measurements at large spacings where there is a paucity of data points. A Gaussian taper is typically used in this weighting method.

To compensate for the clumping of data in the (u,v) plane, density weighting is used. The weights used are assigned values based on the local density of sample points within a grid cell. In natural weighting, each visibility point [illegible] a weight of unity (the cells are weighted by their "natural" distribution on the (u,v) plane.) The cells near the center of the (u,v) plane tend to be emphasized because the region is more populated in visibilities than the outer portions of the plane. Hence, the beam made by natural weighting tends to be broad. This effectively reduces the resolution of the produced image. However, the noise is markedly reduced due to the larger beam size and the image is more sensitive to low intensity emission.

In the second density weighting scheme, the weights assigned are inversely proportional to the number of data points within a block of grid cells (Briggs et al. 1999). The beam produced by this "uniform" weighting is largely controlled by the tapering function as it will specify the size of the cell block to be used in the weighting. This method emphasizes the outer, low density regions and so the beam will contain a small Gaussian core and thereby produce images of higher resolution. Similarly, the signal-to-noise ratio is reduced (as compared to natural weighting) due to the unequal weighting of each visibility as well as the smaller beam size.

A hybrid combination of the two density weighting schemes is also available. This robust weight scheme is controlled by the "robustness" parameter developed by Briggs (1995). Essentially, the value assigned to the parameter in IMAGR specifies how to combine the natural and uniform weighting functions. If the value is greater than four, the hybrid weighting is nearly natural. Nearly pure uniform weighting is used for values less than -4. Careful use of the robust parameter can produce a near uniform weighting beam with low sidelobes while mildly raising the noise added by the weighting.

The calibrated and weighted data obtained from the (u,v) spacings do not lie on a rectangular grid as demanded by the FFT process. A convolution function, C(u,v), is normally employed to interpolate and map the data out on to the desired grid. There are various convolution functions that are available for the purpose. They should have Fourier transforms that are constant across the image field and vanish sharply beyond the edges. This is to minimize the aliasing problems that arise from transforming the data to the image domain. The two most commonly used convolution functions are the *exponential ∗ times sinc* and *spheroidal*.

Gridding of the convolved data into the rectangular map is handled by Bracewell's Shah ("bed of nails") re-sampling function

$$R(u,v) = \mathrm{III}(u/\Delta u, v/\Delta v) = \sum_{j=-\infty}^{\infty} \sum_{k=-\infty}^{\infty} \delta(j - u/\Delta u, k - v/\Delta v)$$

where Δu and Δv are the (u,v) cellsizes. They are related to the image (map) plane cell sizes Δl and Δm by

$$\Delta u \Delta l = \frac{1}{j}$$

and

$$\Delta v \Delta m = \frac{1}{k}$$

where j and k are the number of cells between two grid points in the u and v directions respectively. The relationships arise from the inverse relationship between the (u,v) and (l,m) plane in the Fourier transform. The synthetic beamsize of a properly re-sampled image map will be approximately three to four times $(\Delta l, \Delta m)$ cell sizes.

In summary, the visibilities used to produce the dirty image can be expressed as

$$V^R = \mathrm{III}(C * V^W)$$

where V^R is the visibility to be inverse transformed and V^W is the weighted (calibrated) data.

All the necessary tools to perform the FFT process on the calibrated data at each frequency channel is packaged into IMAGR. An ensemble of all the channels unified into a single data structure called a *data cube*. The initial cube will contain strong contributions from the continuum and sidelobes of the dirty beam which need to be removed. Subtracting the continuum from the line data must first be applied before the removal of the sidelobes. The subtraction may be performed in the (u,v) or map plane. In the image plane, the average of all line-free channels is used to subtract the continuum contribution from all the channels containing line signal. Alternatively a baseline-fitting function for line-free channels can be used to subtract out the continuum from the (u,v) data with line emission.

The sidelobes of the dirty beam are (unwanted) manifestations of the limited extent of the spatial frequencies as well as the null value assignment to unsampled (u v) positions during the FFT application Its removal is performed by a deconvolution process generically called "cleaning" After this process the image map can then be re-convolved with a well-defined clean beam to obtain a stronger model representation of the true brightness distribution `IMAGR` uses Clark's (1980) revision of the cleaning algorithm (CLEAN) developed by Hogbom (1974) CLEAN assumes the dirty image to be composed of radio sources represented by individual point sources in a blank field The strengths and positions of the points are first determined usually in a sub-image area called the "Clean window" rather than the complete field of view The algorithm then subtracts from the dirty image the peaks of the point sources (scaled by the dirty beam and the damping factor called the *loop gain*) This factor is typically around 0 1 to 0 2 in value. The subtracted amplitudes and positions of the peaks of are recorded into a clean component list This iterative process is repeated until the residuals in the subtracted dirty image are less than the user-specified value (FLUX) or the number of iterations (from hundreds to thousands) has been reached To suppress any random features at high spatial frequencies the registered peaks are convolved with a Gaussian restoring clean beam (usually the core of the dirty beam) to produce a clean map

Unfortunately this original clean algorithm is time-consuming Approximately N^2 arithmetic operations are performed at *each* iteration for an N x N area. The Clark method makes use of the FFT applicability of the cleaning process to expedite the job by splitting the task into two cycles Only a "restricted" smaller area of the dirty image containing the strongest peak values is used in the "minor" cycle The dirty beam used to search for the peaks in the restricted (residual) map is assumed to be zero outside the beam patch (a small box between 21 × 41 and 64 × 127 elements centered about the origin) (Clark 1980) The cycle stops when the residuals are below FLUX The "major" cycle consists of using the FFT to transform the clean components back into visibilities to be subtracted from the un *gridded* (u v) data that is then re-gridded and transformed back to the image domain for the next cycle of clean Like CLEAN, the revised algorithm stops when the residual of the whole image is below FLUX or the number of iterations is [illegible] times faster than the original algorithm. The H I data cubes that have been presented in this dissertation are the cleaned cubes produced by the Clark algorithm.

APPENDIX C
FUNDAMENTAL CONCEPTS OF THE FABRY-PEROT INTERFEROMETER

Fabry Perot (FP) interferometery of the H II regions within NGC 3359 was performed by using the wide-field imaging TAURUS instrument at the Cassegrain focus of the 4.2 William Herschel Telescope (WHT) also located La Palma, Spain. The instrument is used primarily to measure the velocity fields of extended emission-line objects. The critical advantage that an FP instrument has over single-slit spectrographs is the ability to image and simultaneously gather spectral information of the full field of view. This section will briefly describe the basic principles FP interferometry and the data reduction of the data. The complete operating manual of TAURUS (Lewis & Unger 1991 hereafter LU91) may be obtained from the Isaac Newton Group of Telescopes at the IAC. The detailed description of the actual observation by the observers are given in Rozas et al. (2000b) and Zurita (2001).

The operation of TAURUS can be displayed schematically, as shown in Figure C-1. Light from the focal plane is first collimated and passed through two semi reflective plane parallel plates separated by air. This element of the FP interferometer, called the etalon, is used to tune the wavelengths of observation by adjusting the spacing between the two plates. The light rays undergo numerous reflections and transmissions in the etalon that produces modulated interference rings that are re-imaged onto the CCD detector of the camera. The order of interference is fixed by placing an order sorting filter whose central wavelength is equal to the redshifted Hα line of the galaxy in the path of the light beam. Thus, one full set of TAURUS data consists of multiple 2-D images of the galaxy that has been observed at different wavelengths across the emission line under study.

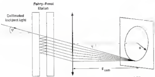

Figure C-1 The optical path and schematic arrangement of the TAURUS Fabry-Perot interferometer

The intensity of the transmitted signal is given by (Plana et al 2003)

$$I(\varpi) = \frac{\tau^2}{(1-\rho)^2} A(\varpi) \tag{C 1}$$

where ρ and τ are the reflection and transmission coefficients of the plates respectively The last term of the equation above is the Airy function (Gordon et al 2000 hereafter GKHJ)

$$A(\varpi) = \frac{1}{1 + F \sin^2(\varpi/2)} \tag{C 2}$$

Known as the finesse of the etalon $F = \rho/(1-\rho)^2$ refers to the width of the maxima of the interference pattern. Lastly, ϖ describes the phase difference between the interference fringes of wavelength λ and is given by

$$\varpi = \frac{4\pi\mu \, \mathrm{S} \cos\Psi}{\lambda} \tag{C 3}$$

where μ is the refractive index of air S is the spacing between the two etalon plates, and Ψ is the angle between the incident light ray and the etalon Each value of $\Psi = R/f_{cam}$ defines a particular point on the image (R is the radial distance of the image point to the optical axis on the detector and F_{cam} is the focal length of the camera)

The Airy function is 2π periodic by nature its maxima occurring when ω [illegible] [illegible] an integer) Thus combined with Equation 3 4 yields

$$n\lambda = 2\mu S \cos\Psi \qquad \text{[illegible]}$$

that when satisfied will produce constructive interference The transmission peaks in such patterns may be altered by varying either S or λ The wavelength range over which λ is allowed to vary is called the Free Spectral Range (FSR a measure of the separation between two successive transmission maxima) The order of interference n and the finesse determine the resolving power (RP) of the instrument

$$RP = \lambda/\Delta\lambda = \frac{2\mu S}{\lambda} F = n \quad F \tag{C 5}$$

for normal incident light rays The resolution can be improved by increasing μS but doing so could lead to interference order overlapping (Betzler 1999) To insure that this does not happen the etalon has a predefined limit for the FSR as given by

$$FSR = \lambda^2/2\mu S = \lambda/n \tag{C 6}$$

for $\Psi = 0$

As pointed out by Zurita (2001) and GKHJ the $\cos\Psi$ term implies that each plane of the data cube does not necessarily correspond to a single plate separation S Rather, a CCD image will contain data from a range of wavelengths (i e within the FSR) In other words, each transmitted wavelength is not only a function of S but also of position (x y) (Equations C 4 and C 5) Therefore the points on the detector will have differently transmitted wavelengths for a fixed value of S (Zurita 2001) The shape of each surface of constant wavelength in the data cube is not a plane but rather a paraboloid (Figure 1 of GKHJ) Unfortunately the combination of λ with (x y) makes the original spatial and spectral axes of the FP data cube unseparable To resolve this conflict phase calibration must be performed on the cube

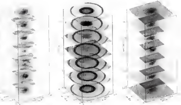

Figure C 2 A) Several planes of an unprocessed FP data cube B) Several planes of the arc lamp cube used for phase calibrat Several planes of a phase- and wavelength calibrated FP data cube. The $x-y$ dimension is the image plane (in pixels) and th represents the channels of the cube [illegible] the phase calibration of the FP data converts the z-axis of the raw (x, y, z) cube to either velocity or wavelength. First, the "phase" (Taylor & Atherton 1980) is established by shifting λ_0 for each pixel at (x, y). This phase shift is applied to each spectrum in such a way that all spectra will have the same wavelength calibration. As a result, a theoretical phase map showing the magnitude of the phase shift as a function of position is created. The phase map can be formulaically expressed as

$$\Phi(x, y) = \Phi_0 + \frac{\mu S(FSR)}{\lambda f_{cam}^2} R^2 \qquad \text{(C.7)}$$

where Φ_0 corresponds to the position along the spectral or S axis and λ is taken to be the central wavelength bandpass of the interference filter (Zurita 2001). In practice, a calibration cube is first made from scanning a monochromatic lamp (Figure C-2) with the etalon. Next, a ring pattern is fitted to each plane of cube to construct a Radius-versus-Frame (R^2 vs. S) plot that subsequently yields the value of the FSR (LU91). This derived value of FSR, along with other constants in Equation C.7 are used to obtain the nominal gap S for a value of λ.

However, due to the caprices of an observation run, effects such as field or detector distortion and/or temporal changes like plate flexure (5-6 μm per hour) and etalon gap drifts can produce an observed phase map that differs from the theoretical prediction. The difference between the two maps is called the residual phase map. For the first effect, the residual is obtained by subtracting the theoretical map (derived from the calibration cube) from the observed. Phase variations due to time (the second effect) are corrected by using 2-D images of the arc lamp that were taken with nominal etalon gap settings during the night. Each image is fitted with a ring pattern and any variation in the plate flexure will shift the center of the pattern while gap drifts will produce a change in the ring radius. The process of making such phase maps and rebinning the data defines the phase calibration stage.

The last step in processing the raw data is to establish the wavelength scale of the data. This process of wavelength calibration is performed by matching the observed FP data cube with the calibration cube whose parameters were derived during the phase calibration stage. The wavelength, interference order, and channel width of the observed data are obtained as functions of the known properties of the calibration cube (Zurita 2001). Both calibration processes were performed with the TAURUS package inside the FIGARO data reduction system

APPENDIX D
DERIVATION OF STABLE AND PERIODIC ORBITS

The location and stability of periodic orbits in a given potential Φ can be determined from their equations of motion. In Cartesian coordinates the Hamiltonian of the model is given by

$$H = \frac{1}{2}(p_x^2 + p_y^2) - (xp_y - yp_x)\Omega_b + \Phi(x,y) = E_J \qquad \text{(D 1)}$$

where p_x and p_y are the canonical conjugate moments of a particle in the reference frame corotating with the bar at angular frequency Ω_b (Patsis & Grosbøl 1996). The equations of motion are

$$x = p_x + \Omega_b y \qquad y = p_y - \Omega_b x$$
$$p_x = -\frac{\partial\Phi(x,y)}{\partial x} + \Omega_b p_y \qquad p_y = -\frac{\partial\Phi(x,y)}{\partial y} - \Omega_b p_x \qquad \text{(D 2)}$$

In terms of Cartesian coordinates and velocities

$$x = \Omega_b(2y + \Omega_b x) - \frac{\partial\Phi(x,y)}{\partial x} \qquad \text{(D 3)}$$

and

$$y = \Omega_b(2x + \Omega_b y) - \frac{\partial\Phi(x,y)}{\partial y} \qquad \text{(D 4)}$$

and the Hamiltonian can be written as

$$H = \frac{1}{2}(x^2 + y^2) + \Phi(x,y) - \frac{1}{2}\Omega_b^2(x^2 + y^2) = h. \qquad \text{(D 5)}$$

Barbanis (1968)

For a given value of the Hamiltonian and initial conditions $[x_0, x_0, y, y_0 = y_0(h)]$ successive upward ($y > 0$) intersections of periodic orbits with the plane $y = 0$ are represented by points in the two- dimensional phase space $(x\ x)$. In this way, a *Poincaré* [illegible]ructed The equations that describe such a map have the form

$$x_1 = f(x_0, \dot{x}_0) \qquad \dot{x}_1 = g(x_0, \dot{x}_0) \tag{D.6}$$

The position of a periodic orbit can be found by first noting that each such orbit will be an invariant point on the corresponding Poincaré surface of section The orbits of the main family of periodic orbits of interest (i e the x_1 family) are reduced to the circular orbits of the central family in the axisymmetric case (Contopoulos and Grosbøl 1986) For a certain value of the Jacobian the initial conditions of the circular orbits in the axisymmetric case is used as a starting guess for the initial conditions of the x_1 orbit in the non-axisymmetric potential A Newton's iteration method is used next and the values for the periodic orbit are found To find the representative of the family for a nearby value of the Jacobian, the value of the periodic orbit just found is used as the next initial guess A fourth-order Runge-Kutta integration method with variable step has been employed for the integration of the equations of motion

The method introduced by Hénon (1965) is used to determined the stability of periodic orbits For a given periodic orbit,

$$x_0 = f(x_0, \dot{x}_0) \qquad \dot{x}_0 = g(x_0, \dot{x}_0) \tag{D.7}$$

Next, a minor perturbation to the initial conditions of the periodic orbit $(x_0 + \Delta x_0, \dot{x}_0 + \Delta \dot{x}_0)$ is introduced and the orbit is again integrated until the next upward intersection with the Poincaré section This $R^2 \to R^2$ transformation connects the final and initial conditions and so

$$x_0 + \Delta x_1 = f(x_0 + \Delta x_0, \dot{x}_0 + \Delta \dot{x}_0) \tag{D.8}$$

$$\dot{x}_0 + \Delta \dot{x}_1 = g(x_0 + \Delta x_0, \dot{x}_0 + \Delta \dot{x}_0) \tag{D.9}$$

Applying the Taylor series expansion to Equations 4 12 and 4 13 about the periodic point $x_1 = x_0$, $\dot{x}_1 = \dot{x}_0$ and keeping only up to first order terms yields

$$\Delta x_1 = a\Delta x_0 + b\Delta \dot{x}_0 \qquad \Delta \dot{x}_1 = c\Delta x_0 + d\Delta \dot{x}_0 \tag{D.10}$$

where a, b, c and d are given by

$$a = \frac{\partial f}{\partial x} \qquad b = \frac{\partial f}{\partial \dot{x}} \qquad c = \frac{\partial g}{\partial x} \qquad d = \frac{\partial g}{\partial \dot{x}} \tag{D 11}$$

The Jacobian of the transformation is

$$\mathcal{A} = \begin{pmatrix} \frac{\partial f}{\partial x} & \frac{\partial f}{\partial \dot{x}} \\ \frac{\partial g}{\partial x} & \frac{\partial g}{\partial \dot{x}} \end{pmatrix} \tag{D 12}$$

and so Equation 4 20 can be rewritten as

$$\begin{pmatrix} \Delta x_1 \\ \Delta \dot{x}_1 \end{pmatrix} = \mathcal{A} \begin{pmatrix} \Delta x_0 \\ \Delta \dot{x}_0 \end{pmatrix} \tag{D 13}$$

Assigning the vectors $\vec{K_1} = (\Delta x_1\ \Delta \dot{x}_1)$ $\vec{K_0} = (\Delta x_0, \Delta \dot{x}_0)$, and noting that areas on Poincaré surfaces of section are conserved (Poincare 1899) (i e $ad - bc = 1$), Equations 4 20 and 4.23 can be written vectorially as $\vec{K_1} = \mathcal{A}\vec{K_0}$ If $\vec{e_1}$ $\vec{e_2}$ form an eigenvector basis of the (reduced) phase space, then we can write

$$\vec{K_0} = A_1\vec{e_1} + A_2\vec{e_2} \tag{D 14}$$

and

$$\vec{K_1} = A_1\lambda_2\vec{e_1} + A_2\lambda_2\vec{e_2} \tag{D 15}$$

where λ_1 and λ_2 are the eigenvalues of the Jacobian matrix The characteristic equation of $\mathcal{A}$ is represented by

$$\begin{vmatrix} a-\lambda & b \\ c & d-\lambda \end{vmatrix} = \lambda^2 - (a+d)\lambda + 1 = 0 \tag{D 16}$$

The roots to the equation are inverse. If $|a+d| < 2$, then the roots are complex conjugates ($|\lambda_1| = |\lambda_2| = 1$) and the orbit is stable. The orbit will be unstable when the roots are real or $|a+d| > 2$ (Hénon 1965) The equation

$$\alpha = 1/2\,(a+d) \tag{D 17}$$

is called Henon's stability index. A periodic orbit is stable when $|\alpha| < 1$. Conversely, it is unstable for $|\alpha| > 1$.

APPENDIX E
SMOOTH PARTICLE HYDRODYNAMICS

There are several computer programs that can satisfactorily simulate the gas flow within a disk galaxy numerically. Among the codes that have been used extensively in galactic research are the second order flux splitting method (FS2) (van Albada et al. 1982 and references therein) and the Beam scheme (Sanders & Prendergast 1974). In this research, Smoothed Particle Hydrodynamics (SPH) is used to model the large scale behavior of gas dynamics within NGC 3359. The code was first introduced by Lucy (1977) and Gingold & Monaghan (1977) and has been adopted by many other subsequent authors (Benz 1990, Monaghan 1985, 1988). The present SPH program is a revised version of the code used in Patsis & Athanassoula (2000).

The main advantage of SPH is that it is Lagrangian by nature and does not require a grid to calculate the spatial derivatives. Instead, the fluid is modeled as individual elements called particles that essentially forms a grid of moving points. This in turns avoids the need to regrid the fluid as it evolves and gives high resolution to high-density regions as the particles follow the density distribution of the fluid. The "particles" are allowed to move and interact hydrodynamically with each other if they are within the domain of interaction (specified by h, the smoothing length). A particle and its interacting neighbors therefore change throughout the simulation as the separation distances between them vary in time.

SPH is best viewed as an interpolation scheme used to solve the set of hydrodynamic equations governing a system of discrete points. The equations (of motion) are functions of various physical fields in the simulation. Values for a field are typically known only at a finite number of N points. An approximation to any point in the field requires an average over finite space (ξ). The average is calculated from the smoothed approximation

$$\langle f(\mathbf{r})\rangle = \int_{\xi} f(\mathbf{r}')\, W(\mathbf{r}-\mathbf{r}', h)\, d\mathbf{r}' \qquad \text{(E.1)}$$

where $f(\mathbf{r})$ is the interpolated field, W is the interpolating kernel, and h is the smoothing length that controls the width of W and the spatial resolution. The interpolation kernel normalizes to unity and is strongly peaked at $r = 0$ so that

$$\lim_{h \to 0} W(\mathbf{r}, h) = \delta(\mathbf{r})$$

and at the same time, $\langle f(\mathbf{r}) \rangle \to f(\mathbf{r})$ as $h \to 0$.

The integral of Equation E.1 is approximated by a summation of the N particles during numerical calculations. Hence,

$$\langle f(\mathbf{r}) \rangle = \sum_{j=1}^{N} \frac{f(\mathbf{r}_j)}{\langle n(\mathbf{r}') \rangle} W(\mathbf{r} - \mathbf{r}_j, h) \tag{E.2}$$

where $n(\mathbf{r}')$ is the number density. To simulate a fluid properly, each point is associated with a fluid element of mass m_j while the number density is defined as $\langle n(\mathbf{r}_j) \rangle = \rho(\mathbf{r}_j)/m_j$. This definition, combined with Equation E.2, gives

$$\langle f(\mathbf{r}) \rangle = \sum_{j=1}^{N} \frac{m_j}{\rho(\mathbf{r}_j)} f(\mathbf{r}_j)\, W(\mathbf{r} - \mathbf{r}_j, h) \tag{E.3}$$

This is the base SPH equation that can approximates any physical property of the fluid. For example, the density of the fluid may be found by setting $f(\mathbf{r}) = \rho(\mathbf{r})$ and so

$$\langle \rho(\mathbf{r}) \rangle = \sum_{j=1}^{N} m_j\, W(\mathbf{r} - \mathbf{r}_j, h)$$

Therefore, the fluid density at any point of the system can be obtained by simply knowing the location and mass of the particle. If the masses of the particles are constant and none are lost, the continuity equation is satisfied by the equation above.

Additionally, the gradient and divergence of $f(\mathbf{r})$ are expressed as

$$\langle \nabla f(\mathbf{r}) \rangle = \int_{\Omega} f(\mathbf{r}')\, \nabla W(\mathbf{r} - \mathbf{r}', h)\, d\mathbf{r}' \tag{E.4}$$

and

$$\langle \nabla \cdot f(\mathbf{r}) \rangle = \int_{\Omega} f(\mathbf{r}') \cdot \nabla W(\mathbf{r} - \mathbf{r}', h)\, d\mathbf{r}' \tag{E.5}$$

respectively. Equations E.3 and E.4 are the two primary equations that are used to solve for the various forces at any point in the fluid and allow for the movement of the gas particles (provided that ∇W exists).

E.1 Smoothing Length and Interpolating Kernel

The smoothing lengths of particles that determines the kernel is both temporally and spatially variable. Typically an optimum number of neighbors are required to be within the neighborhood of a particle, as specified by a given h. If there are not enough neighbors within the local region to satisfy the criteria, the value of h is doubled and the search is iterated until some tolerance of the optimum number is reached. Conversely, only the nearest neighbors within the particle's smoothing length are included in a search that results in a value greater than the optimum number. This is desirable as it allows for the fluid simulation to work. Since h defines the region where the forces and physical fluid properties are smoothed out, simulations with fixed smoothing lengths will fail at low-density regions where particles may be left isolated with no interacting neighbors nearby. Consequently, the spatial resolution of the SPH method is determined by h with regions of higher density being better resolved.

The errors associated with spatially varying smoothing lengths have been found to be on the same order as the inherent error in the SPH method, i.e., the errors are of second order, $\mathcal{O}(h^2)$ (Bate 1995, Hernquist & Katz 1989, Monaghan 1985). The more profound impact of introducing the variable smoothing length however lies in its effect on the mutual forces between the particles. During the calculation of the gradient of a physical field, the smoothing lengths of two particles must be the same (i.e., the force from particle j on particle i must be the same as the opposing force from particle i). The common method of achieving this is to replace h_i and h_j by their average. Doing so conserves momentum. Consequently, the kernel is required to be symmetric (Monaghan 1992).

One of the main advantages of the SPH method is its usage of the interpolating kernel as a subroutine in the source code. However, the kernels that were originally used proved to be inefficient as all N particles contributed to the summations that led to wasteful use of computation time. To avoid this shortcoming, the spline kernel of

Monahan and Lattanzio (1985) is used for the simulations. It is the most common SPH kernel today and considers only a selected number of points in a defined neighborhood to solve for the local physical quantities. The spline kernel has the form

$$W(r,h) = \frac{10}{7\pi h^2} \begin{cases} 1 - \frac{3}{2}v^2 + \frac{3}{4}v^3 & \text{if } 0 \leq v < 1, \\ \frac{1}{4}(2-v)^3 & \text{if } 1 \leq v < 2 \\ 0 & \text{otherwise.} \end{cases}$$

As stated above, the main advantage of the kernel is its compact support (i.e. particles with $r > 2h$ do not contribute to the kernel). In addition, the second derivative of the kernel is continuous. This allows for the assumption that the summation term can sufficiently approximate the integral of Equation E.1 (Monahan 1992).

E.2 Hydrodynamical Equations and Properties

Euler's equations are used to describe the phase space evolution of the fluid in SPH simulations. The equations are

$$\frac{d\mathbf{r}}{dt} = \mathbf{v}$$

and

$$\frac{d\mathbf{v}}{dt} = \mathbf{S}_{\text{visc}} - \nabla\phi - \frac{\nabla \mathbf{P}}{\rho}$$

where $\mathbf{S}_{\text{visc}}$ is the artificial viscosity term (Hernquist & Katz 1989). The density at each particle position (say, particle i) is

$$\rho_i = m_i W(0, h_i) + \sum_{j=1}^{N_n} m_j W(r_{ij}, h_{ij})$$

where N_n is the number of the particle's neighbors within the average smoothing length h_{ij}. Similarly, the total gravitational force felt by the particle is

$$\nabla\phi_i = G \sum_{j=1}^{N} \frac{M(r_{ij})}{r_{ij}^2} \frac{\mathbf{r}_{ij}}{r_{ij}}$$

while the pressure gradient is calculated from using the momentum equation such that

$$-\frac{\nabla \mathbf{P}}{\rho} = \sum_{j=1}^{N_n} m_j \left(\frac{P_i}{\rho_i^2} + \frac{P_j}{\rho_j^2} \right) \nabla_i W(r_{ij}, h_{ij})$$

Pressur[illegible] tropic equation of state

$$P = K\rho^{\gamma} \tag{E 6}$$

For this study the gas is assumed to be isothermal and so Equation E 6 becomes $P = c_s^2\rho$ where c_s is the sound speed

Artificial viscosity is required for the proper treatment of shocks by setting up the dissipation of heat where the phenomena occur Without $\mathbf{S}_{\rm visc}$, shocks cannot occur in the simulation as the kinetic energy of the moving particles is transformed into heat The artificial viscosity in the current SPH version has the form of

$$\mathbf{S}_{\rm visc} = -\sum_{j=1}^{N_n} m_j \Pi_{ij} \nabla_i W(r_{ij}, h_{ij})$$

with

$$\Pi_{ij} = \begin{cases} (-\alpha c_s \mu_{ij} + \beta\mu_{ij}^2)/\rho_{ij} & \mathbf{v}_{ij} \cdot \mathbf{r}_{ij} \leq 0, \\ 0 & \mathbf{v}_{ij} \cdot \mathbf{r}_{ij} > 0 \end{cases}$$

where

$$\mu_{ij} = \frac{h\,\mathbf{v}_{ij} \cdot \mathbf{r}_{ij}}{\mathbf{r}_{ij}^2 + \eta^2}$$

$\rho_{ij} = (\rho_i + \rho_j)/2$, and $\mathbf{v}_{ij} = \mathbf{v}_i - \mathbf{v}_j$ The term $\eta^2 = 0.01h^2$ is used to avoid singularity at small interparticle distances The bulk viscosity α is used to suppress after shock subsonic velocity oscillations and β is a (von Neumann-Richtmyer-type) viscosity used to eliminate particle interpenetration in strong shocks (Bate 1994)

Finally, the SPH energy equation of

$$\frac{du_i}{dt} = \frac{P_i}{\rho_i^2}\sum_{j=1}^{N_n} m_j \mathbf{v}_{ij} \cdot \nabla_i W(r_{ij}, h_{ij}) + \frac{1}{2}\sum_{j=1}^{N_n} m_j \Pi_{ij} \mathbf{v}_{ij} \cdot \nabla_i W(r_{ij}, h_{ij}) \tag{E 7}$$

is needed to close the systems of equations required to run the code. The last term on the right-hand side of the equation above has been added to include the change of the entropy of the gas (related to K of Equation E.6) owing to the use of artificial viscosity

REFERENCES

Aguerri, J. A. L. 1999, A&A, 351, 43

Aguerri, J. A. L., Beckman, J. E., & Prieto, M. 1998, AJ, 116, 2136

Aguerri, J. A. L., Debattista, V. P. & Corsini, E. M. 2003, 338, 465

Allen, R. J., Hamaker, J. P., & Wellington, K. J. 1974, A&A, 31, 71

Athanassoula, E. 1992a, MNRAS, 259, 328

Athanassoula, E. 1992b, MNRAS, 259, 345

Athanassoula, E. 2003, MNRAS, 341, 1179

Athanassoula, E., Bienaymé, O., Martinet, L., & Pfenniger, D. 1983, A&A, 127, 349

Athanassoula, E. & Bosma, A. 2003, Ap&SS, 284, 491

Baars, J. W. M., Genzel, R., Pauliny-Toth, I. I. K., Witzel, A. Baar Genzel Pauliny-Toth Witzel 1977, A&A, 61, 99

Bacon, R., Copin, Y., Monnet, G., Miller, B. W., Allington-Smith, J. R., Bureau, M., Carollo, C. M., Davies, R. L., Emsellem, E., Kuntschner, H., Peletier, R. F., Verolme, E. K., & de Zeeuw, P. T. 2001, MNRAS, 326, 23

Ball, R. 1986, ApJ, 307, 453

Ball, R. 1992, ApJ, 395, 418

Barbanis, B. 1968, AJ, 73, 784

Bate, M. R. 1995, Ph. D. thesis, Univ. Cambridge., Cambridge, U. K., 27

Begeman, K. G. 1989, A&A, 223, 47

Benz, W. 1990, in *The Numerical Modelling of Nonlinear Stellar Pulsations Problems and Prospects*, ed. J. R. Buchler (Dordrecht: Kluwer), 269

Benz, W., Hills, J. G., & Thielemann, F. K. 1989, ApJ, 342, 986

Bertin, G., Lin, C. C., Lowe, S. A., & Thurstans, R. P. 1989, ApJ, 338, 78

Bertin, G., Lin, C. C., Lowe, S. A., & Thurstans, R. P. 1989, ApJ, 338, 104

Berry, C. L. & De Smet, D. J. 1978, AJ, 83, 500

Betzler, K. 1997, in *Fabry Perot Inteferometer*, Univ. Osnabruck, Germany www.physik.uni-osnabrueck.de/kbetzler/sos/fabryperot.pdf 08/03

Binney, J. & Merrifield, M. 1998, in *Galactic Astronomy* (Princeton: Princeton University Press), 490

Binney, J. & Tremaine, S. 1987, in *Galactic Dynamics* (Princeton: Princeton University Press), 146

Bissantz, N., Englmaier, P. & Gerhard, O. 2003, MNRAS, 340, 949

Bosma, A. 1981a, AJ, 86, 1791

Bosma, A. 1981b, AJ, 86, 1825

Bosma, A. 1992, in *Morphological and Physical Classification of Galaxies*, eds. G. Longo, M. Capaccioli, & G. Busarello (Dordrecht: Kluwer), 207

Bosma, A. 1996, in *Barred Galaxies*, ASP Conference Series, Vol. 91, eds. R. Buta, D. A. Crocker & B. G. Elmegreen (San Francisco: PASP), 132

Bottinelli, L., Gouguenheim, L., Fouqué, P. & Paturel, G., 1990, A&AS, 82, 391

Braine, J. & Combes, F. 1992, A&A, 264, 433

Brandt, J. C. 1960, ApJ, 131, 293

Briggs, D. S. 1995, Ph.D. thesis, New Mexico Institute of Mining and Technology, Socorro, NM, 25

Briggs, D. S., Schwab, F. R. & Sramek, R. A. 1999, in *Synthesis Imaging in Radio Astronomy II*, ASP Conference Series, Vol. 180, eds. G. B. Taylor, C. L. Carilli & R. A. Perley (San Francisco: PASP), 133

Broeils, A. H. & Rhee, M.-H. 1997, A&A, 324, 877

Broeils, A. H. & van Woerden, H. 1994, A&AS, 107, 129

Buta, R. & Block, D. L. 2001, ApJ, 550, 243

Buta, R. & Combes, F. 1996, Fundam. Cosmic Phys., 17, 95

Buta, R., Crocker, D. A., & Byrd, G. G. 1999, AJ, 118, 2071

Buta, R. & Purcell, G. B. 1998, AJ, 115, 484

Buta, R., van Driel, W., Braine, J., Combes, F., Wakamatsu, K., Sofue, Y., & Tomita, A. 1995, ApJ, 450, 593

Canzian, B. 1993, ApJ, 414, 487

Clark, B. G. 1980, A&A, 89, 377

Clark, B. G. 1999, in *Synthesis Imaging in Radio Astronomy II*, ASP Conference Series, Vol. 180, eds. G. B. Taylor, C. L. Carilli, & R. A. Perley (San Francisco: PASP), 1

Cohen, J. G., Persson, S. E., Elias, J. H., & Frogel, J. A. 1981, ApJ, 249, 481

Combes, F. 1996, in *Barred Galaxies*, ASP Conference Series, Vol. 91, eds. R. Buta, D. A. Crocker & B. G. Elmegreen (San Francisco: PASP), 286

Combes, F., Boissé, P., Mazure, A. & Blanchard, A. 1995, in *Galaxies and Cosmology* (Berlin: Springer-Verlag), 41

Combes, F. & Elmegreen, B. G. 1993, A&A, 271, 391

Condon, J. J., Helou, G., Sanders, D. B. & Soifer, B. T. 1990, ApJS, 73, 359

Contopoulos, G. 1980, A&A, 81, 198

Contopoulos, G. 1981, A&A, 102, 265

Contopoulos, G. 1988, A&A, 201, 44

Contopoulos, G. 2002, in *Order and Chaos in Dynamical Astronomy* (Springer: Berlin), 473

Contopoulos, G. & Grosbøl, P. 1986, A&A, 155, 11

——— 1989, A&A Rev., 1, 261

Contopoulos, G. & Mertzanides, C. 1977, A&A, 61, 477

Contopoulos, G. & Papayannopoulos, T. 1980, A&A, 92, 33

Cox, A. L. & Puche, D. 2001, "A step-by-step guide to spectral-line data analysis in AIPS", NRAO, http://www.aoc.nrao.edu/aips/cook.html, 12/03

de Jong, R. S. 1996, A&AS, 118, 557

de Vaucouleurs, G. 1963, ApJS, 8, 31

de Vaucouleurs, G. 1979, AJ, 84, 1270

de Vaucouleurs, G., de Vaucouleurs, A., Corwin, H. G., Buta, R., Paturel, G., and Fouque, P. 1991, in Third Reference Catalogue of Bright Galaxies (New York: Springer), 606 (RC3)

Dreyer, J. L. E. 1888, MmRAS, 49, 1

Duval, M. F. & Monnet, G. 1985, A&AS, 61, 141

Elmegreen, D. M. 1981, ApJS, 47, 229

Elmegreen, D. M. 1996b, in *Barred Galaxies*, ASP Conference Series, Vol. 91, eds. R. Buta, D. A. Crocker & B. G. Elmegreen (San Francisco: PASP), 23

Elmegreen, D. M. 1998, in *Galaxies and Galactic Structure* (Prentice-Hall: New Jersey), 43

Elmegreen, D. M., Chromey, F. R. & Santos, M. 1998, AJ, 116, 1221

Elmegreen, D. M. & Elmegreen, B. G. 1982, MNRAS, 201, 102

Elmegreen, B. G. & Elmegreen, D. M. 1985, ApJ, 288, 438

Elmegreen D. M., Elmegreen B. G. 1995, ApJ, 445, 591

Elmegreen, D. M., Elmegreen, B. G., Chromey, F. R., Hasselbacher, D. A. & Bissell, B. A. 1996a, AJ, 111, 1880

Elmegreen, B. G., Elmegreen, D. M., Chromey, F. R., Hasselbacher, D. A. & Bissell, B. A. 1996c, AJ, 111, 2233

Elmegreen, B. G., Elmegreen, D. M. & Montenegro, L. 1992, ApJS, 79, 37

England, M. N. 1986, Ph. D. thesis, University of Florida

England, M. N. 1989, ApJ, 344, 669

England, Martin N., Gottesman, S. T., & Hunter, J. H., Jr. 1990, ApJ, 348, 459

England, M. N., Hunter, J. H., Jr. & Contopoulos, G. 2000, ApJ, 540, 154

Englmaier, P. & Gerhard, O. 1997, MNRAS, 287, 57

Erwin, P. & Sparke, L. S. 2002, AJ, 124, 65

Erwin, P. & Sparke, L. S. 2003, ApJS, 146, 299

Ewen, H. I. & Purcell, E. M. 1951, Nature, 168, 356

Falco, E. E., Kurtz, M. J., Geller, M. J., Huchra, J. P., Peters, J., Berlind, P., Mink, D. J., Tokarz, S. P., Elwell, B. 1999, PASP, 111, 438

Fisher, J. R. & Tully, R. B. 1981, ApJS, 47, 139

Fomalont, E. B. & Perley, R. A. 1999, in *Synthesis Imaging in Radio Astronomy II*, ASP Conference Series, Vol. 180, eds. G. B. Taylor, C. L. Carilli & R. A. Perley (San Francisco: PASP), 79

Fraternali, F., Oosterloo, T., Sancisi, R. & van Moorsel, G. 2001, ApJ, 562L, 47

Friedli, D. & Benz, W. 1993, A&A, 268, 65

Friedli, D., Benz, W. & Kennicutt, R. 1994, ApJ, 430, 105

Friedli, D. & Martinet, L. 1993, A&A, 277, 27

Gérin, M., Combes, F. & Athanassoula, E. 1990, A&A, 230, 37

Gerssen, J. 2002, in *Disks of Galaxies: Kinematics, Dynamics and Perturbations*, ASP Conference Series, Vol. 275, eds. E. Athanassoula, A. Bosma & R. Mujica (San Francisco: PASP), 201

Gingold, R. A. & Monaghan, J. J. 1977, MNRAS, 181, 375

Goldreich, P. & Tremaine, S. 1981, ApJ, 243, 1062

Gordon, S., Koribalski, B., Houghton, S., & Jones, K. 2000, MNRAS, 315, 248

Gottesman, S. T. 1982, AJ, 87, 751

Gottesman, S T Ball R Hunter J H Jr & Huntley J M 1984 ApJ 286 471

Gottesman, S T & Weliachew L 1975 ApJ 195, 23

Giovanelli R & Haynes M P 1988 in *Galactic and Extragalactic Radio Astronomy* eds G L Verschuur & K I Kellerman (New York Springer Verlag) 534

Graham, A W 2003 AJ 125 3398

Haynes, M. P van Zee L Hogg, D E Roberts M S & Maddalena, R. J 1998 AJ 115, 62

Hesschen, D S & Wade, G M 1964 AJ 69, 277

Heller, C H & Shlosman L 1994 ApJ 424 84

Hénon M 1965 AnAp, 28, 499

Hénon M & Heiles C 1964 AJ 69 73

Hernquist, L & Katz N 1989 ApJS, 70 419

Ho L C Filippenko, A V , & Sargent W L W 1997 ApJS 112, 315

Hockney, R. W & Hohl F 1969 AJ, 74 1102

Hodge P W 1969 ApJS 18 73

Hogbom, J A. 1974 A&AS 15 417

Hubble, E P 1926, ApJ 64, 321

Hubble, E P 1949 PASP 61, 121

Huchtmeier, W K & Richter O G 1989, A General Catalog of H I Observations of Galaxies (New York Springer Verlag) 117

Hunter J H , Jr 1990 in *Galactic Models*, eds. J R. Buchler S T Gottesman & J H Hunter Jr (New York New York Academy of Sciences), 174

Hunter, J H., Jr Ball R & Gottesman, S. T , 1984 MNRAS, 208 1

Hunter, J H. Jr England M N , Gottesman S T Ball R., & Huntley J M 1988, ApJ 324, 721

Hunter, J H , Jr & Gottesman, S T 1996 in *Barred Galaxies* ASP Conference Series Vol 91 eds. R Buta D A Crocker & B G Elmegreen (San Francisco: PASP), 398

Huntley J M Sanders, R H., & Roberts W W 1978, ApJ 221 521

Israel F P & van der Hulst J.M 1983, AJ, 88, 1736

Jarrett, T H., Chester T & Cutri, R 2003, AJ, 125, 525

Jedrzejewski, R. I 1987 MNRAS 226, 747

Jungwiert B Combes F & Axon D J 1997 A&AS 125 479

Kamphuis J Sancisi R & van der Hulst T 1991, A&A, 244 L29

Kent S M 1987, AJ 93 816

Knapen, J H 1997 MNRAS 286 403

Knapen J H Shlosman, L, & Peletier R F 2000 ApJ 529 93

Knapen J H 1999 astro-ph/9907290

Knapen, J H , Shlosman L & Peletier, R F 2000 ApJ, 529, 93

Kranz, T , Slyz, A & Rix H W 2001, ApJ 562 164

Kranz T , Slyz, A & Rix H W 2003 ApJ 586 143

Kristian J , Nemec, J C., & Staples S 1985 IAUC, 4050 1

Laine S 1996 Ph D thesis, Univ Florida, 154

Laine S Shlosman L & Heller C H 1998 MNRAS 297, 1052

Laurikainen, E & Salo H 2002 MNRAS 337 1118

Lewis, B M 1984 ApJ 285, 453

Lewis, J & Unger S. 1991 in *William Herschel Telescope Taurus Data and How to Reduce It* (La Palma Obs Roque de los Muchachos) 3

Lin, C C 1968, in *Galaxies and the Universe*, ed L Woltjer (New York Columbia University Press) 1

Lindblad B 1927 MNRAS 87, 553

Lindblad P A B 1999 Ph D Thesis Univ Stockholm, Stockholm, Sweden, 3

Lindblad P A B Lindblad P O , & Athanassoula, E 1996 A&A 313 65

Lucy L B 1977, ApJ 82, 1013

Lynden Bell, D 1979 MNRAS, 187 101

Martin, P 1995, AJ 109 2428

Martin P & Roy, J -R 1994 ApJ, 424 599

Martin P & Roy J R. 1995 ApJ 445 161

Masset, F & Tagger M 1997 A&A, 322 442

Mestel L 1963, MNRAS, 126 553

Mihalas D & Binney, J 1981 in *Galactic Astronomy* (San Francisco W H Freeman), 488

Miller, R H & Prendergast, K H 1968, ApJ, 151 699

Moiseev, A. V. 2002, Bull. SAO, 54, 2

Möllenhoff, C. & Heidt, J. 2001, A&A, 368, 16

Monaghan, J. J. 1988, Comput. Phys. Comm., 48, 89

Monaghan, J. J. 1992, ARA&A, 30, 543

Monaghan, J. J. & Lattanzio, J. C. 1985, A&A, 149, 135

Moore, E. M. & Gottesman, S. T. 1995, ApJ, 447, 169

Moore, E. M. & Gottesman, S. T. 1998, MNRAS, 294, 353

Nilson, P. 1973, in *Uppsala General Catalogue of Galaxies* (Uppsala: Royal Society of Sciences of Uppsala), 1

Noguchi, M. 1987, MNRAS, 228, 635

Ohta, K., Hamabe, M., & Wakamatsu, K.-I. 1990, ApJ, 357, 71

Patsis, P. A. 1991, Ph. D. thesis, Univ. Athens, Athens, Greece

Patsis, P. A. & Athanassoula, E. 2000, A&A, 358, 45

Patsis, P. A., Athanassoula, E. & Quillen, A. C. 1997, ApJ, 483, 731

Patsis, P. A. & Grosbol, P. 1996, A&A, 315, 371

Patsis, P. A., Grosbol, P. & Hiotelis, N. 1997, A&A, 323, 762

Patsis, P. A., Heraudeau, Ph., & Grosbol, P. 2001, A&A, 370, 875

Patsis, P. A., Hiotelis, N., Contopoulos, G. & Grosbol, P. 1994, A&A, 286, 46

Patsis, P. A. & Kaufmann, D. E. 1999, A&A, 352, 469

Patsis, P. A., Skokos, C., Athanassoula, E. 2003, MNRAS, in press

Phillips, A. C. 1996, in *Barred Galaxies*, ASP Conference Series, Vol. 91, eds. R. Buta, D. A. Crocker & B. G. Elmegreen (San Francisco: PASP), 48

Plana, H., Rosado, M., Gutierrez, L., Castaneda, H., Langarica, A. R., & Bernal, A. 2003, in *PUMA User's Manual, Version 2.0*, Instituto De Astronomía De La UNAM Ensenada, http://www.astrosen.unam.mx/Instruments/puma/puma.html 08/03

Poincaré, H. 1892, in *Les Méthodes Nouvelles de la Méchanique Céleste* (Paris: Gauthier Villars), 192

Prendergast, K. H. 1983, in *Internal Kinematics and Dynamics of Galaxies*, ed. Athanassoula, E. (Dordrecht: Reidel), 215

Quillen, A. C., Frogel, J. A. & Gonzalez, R. A. 1994, ApJ, 437, 162

Rautiainen, P. 2000, Ph. D. Thesis, University of Oulu, Oulu, Finland, 20

Rautiainen, P. & Salo, H. 1999, A&A, 348, 737

Regan, M W & Teuben, P 2003 ApJ 582, 723

Regan, M W Vogel, S N & Teuben, P 1997, ApJ 482 143

Relano M., Beckman, J E Rozas M & Dyson J E 2003 in *Winds, Bubbles and Explosions* RevMexAA Serie de Conferencias, Vol. 15 eds. J M R Espinosa, F G Lpez & V M Marta, 281

Relano M Beckman J E. Rozas, M & Zurita A 2003 in *Winds Bubbles and Explosions* RevMexAA Serie de Conferencias Vol 15, eds. J M R. Espinosa, F G Lpez, & V M Marta 205

Richter, O G & Sancisi, R. 1994 A&A 290 L9

Rix H -W & Rieke, M J 1993, ApJ 418 123

Roberts W W Huntley, J M & van Albada, G D 1979 ApJ, 233 67

Rogstad D H, Rougoor G W & Whiteoak, J B 1967, ApJ 150, 9

Rohlfs K 1977 in *Lectures on Density Wave Theory* (Springer Berlin) 94

Rots, A. H 1975, A&A 45 43

Rots A H 1980 A&AS, 41 189

Roy, J R 1996, in *Barred Galaxies* ASP Conference Series Vol 91 eds R. Buta, D A Crocker & B G Elmegreen (San Francisco: PASP) 63

Rozas M. Beckman, J E, & Knapen, J H. 1996, A&A 307 735

Rozas, M & Sempere M J 2002 in *Cosmic Evolution and Galaxy Formation Structure Interactions and Feedback*, ASP Conference Proceedings Vol 215, eds by J Franco L Terlevich O López-Cruz and I Aretxaga. (San Francisco PASP) 117

Rozas, M Zurita, A & Beckman J E 2000a, A&A 354, 823 (RZB)

Rozas, M., Zurita, A., Beckman J E & Pérez, D 2000b A&AS 142, 259 (RZB2)

Rubin, V C, Burstein D Ford, W K Jr., & Thonnard, N 1985 ApJ 289 81

Rupen, M P 1999 in *Synthesis Imaging in Radio Astronomy II* ASP Conference Series, Vol 180, eds G B Taylor C L Carilli, & R. A Perley (San Francisco PASP) 258

Ryder S D Buta, R. J Toledo, H, Shukla, H, Staveley-Smith L & Walsh, W 1996 ApJ 460 665

Sanders, R. H & Prendergast K H 1974 ApJ 188 489

Sandage, A R. & Tammann G A 1981, in *A Revised Shapley Ames Catalog of Bright Galaxies* (Washington DC Carnegie Institution of Washington) 32

Sanders, R. H. & Huntley, J M 1976 ApJ 209, 53

Sanders, R. H & Prendergast K H 1974, ApJ 188, 489

Sanders R. H & Tubbs A D 1980 ApJ 235 803

Seigar M S & James, P A 1998, MNRAS 299 672

Sellwood J A 1981 A&A, 99, 362

Sellwood J A 1996 in *Barred Galaxies* ASP Conference Series, Vol 91 eds R. Buta D A Crocker & B G Elmegreen (San Francisco PASP) 259

Sellwood J A & Sparke L S 1988 MNRAS 231, 25

Sellwood, J A. & Wilkinson A 1993 Rep Prog Phys 56 173

Sempere M 1999 Ap&SS 269, 685

Sheth K., Regan, M W Scoville, N Z & Strubbe, L E. 2003, ApJ 592 13

Shlosman I 2002 in *Disks of Galaxies Kinematics Dynamics and Perturbations* ASP Conference Series Vol 275 eds. E Athanassoula & A Bosma, (San Francisco PASP) 231

Skokos, Ch., Patsis P & Athanassoula E 2002 MNRAS 333 847

Skrutskie, M. F Reber T J Murphy N W & Weinberg M D 2001 AAS, 199 9104

Soifer, B T., Boehmer L Neugebauer G & Sanders D B 1988 AJ 98 766

Sorensen S-A Matsuda, T & Fujimoto M 1976 Ap&SS 43 491

Stark, A A Elmegreen, B G & Chance D 1987 322, 64

Staveley Smith L & Davies R D 1988 MNRAS, 231 833

Sygnet J F., Tagger M Athanassoula E. & Pellat R 1988 MNRAS 232 733

Tagger M., Sygnet J F Athanassoula E & Pellat R 1987 ApJL 318, L43

Taylor K & Atherton, P D 1980 MNRAS 191 675

Tenorio-Tagle G 1981, A&A, 94 338

Teuben P J 2002 in *Disks of Galaxies Kinematics Dynamics and Perturbations* ASP Conference Series Vol 275 eds E Athanassoula & A Bosma (San Francisco PASP) 220

Thompson A. R. 1999, in *Synthesis Imaging in Radio Astronomy II* ASP Conference Series Vol 180 eds G B Taylor, C L Carilli & R A Perley (San Francisco PASP) 20

Tifft, W G 1990, ApJS 73 603

Toomre, A 1981, in *The Structure and Evolution of Normal Galaxies*, eds S M Fall & D Lynden Bell (Cambridge: Cambridge Press) 111

Tremaine, S & Weinberg, M D 1984, ApJL 282 5

Tully R. B & Fouqué, P 1985, ApJS, 58 67 van Albada, G. D. & Roberts, W. W., Jr. 1981, ApJ, 246, 740

van Albada, T. S. & Sanders, R. H. 1982, MNRAS, 201, 303

van Albada, G. D., van Leer, B., & Roberts, W. W., Jr. 1982, A&A, 108, 76

van den Bergh, S., Abraham, R. G., Ellis, R. S., Tanvir, N. R., Santiago, B., & Glazebrook, K. G. 1996, AJ, 112, 359

van den Bergh, S., Cohen, J., Hogg, D. W., & Blandford, R. 2000, AJ, 120, 2190

van der Hulst, H. C. 1945, Ned. Tijd. Natuurkunde, 11, 210

van Driel, W. & Buta, R. J. 1991, A&A, 245, 7

van Gorkom, J. 1993, in *The Environment and Evolution of Galaxies*, eds. J. M. Shull & H. A. Thronson (Dordrecht: Kluwer), 345

Wada, K. 1994, PASJ, 46, 165

Warner, P. J., Wright, M. C. H., & Baldwin, J. E. 1973, MNRAS, 163, 163

Weiner, B. J., Sellwood, J. A., & Williams, T. B. 2001, ApJ, 546, 931

Weiner, B. J., Williams, T. B., van Gorkom, J. H., & Sellwood, J. A. 2001, ApJ, 546, 916

Wong, T. 2000, Ph.D. thesis, Univ. California, Berkeley, CA, 18

Wozniak, H., Friedli, D., Martinet, L., Martin, P., & Bratschi, P. 1995, A&AS, 111, 115

Young, J. S., Xie, S., Tacconi, L., Knezek, P., Viscuso, P., Tacconi-Garman, L., Scoville, N., Schneider, S., Schloerb, F. P., Lord, S., Lesser, A., Kenney, J., Huang, Y. L., Devereux, N., Claussen, M., Case, J., Carpenter, J., Berry, M., & Allen, L. 1995, ApJS, 98, 219

Zurita, A. 2001, Ph.D. thesis, Instituto de Astrofísica de Canarias (IAC), La Laguna, Tenerife, Spain, 43

Zurita, A., Beckman, J. E., Rozas, M., & Ryder, S. 2002, A&A, 386, 801

BIOGRAPHICAL SKETCH

I was born in the great country of Thailand and moved to Germany to live with my mother, step-father, and brother on a military base shortly after my tenth birthday. My step-father, whom I now proudly call "Dad," was an officer of the United States Air Force and so we were fortunate enough to have been stationed in Europe for 3 years. There I learned English and acclimated myself to the American lifestyle. Years later we were assigned to an Air Force base in the panhandle of Florida, where I graduated from high school and attended community college for 2 years. Afterwards I enrolled at the University of Florida and received my Bachelor of Science degree in astronomy in the summer of 1995. That fall I began my graduate career and began studying under Dr. Gottesman in 1997. It has been quite a journey, both literally (through Spain and Greece) and figuratively so far. The knowledge I have acquired is invaluable and certainly has satisfied my curiosity about this wonderful branch of science.

I certify that I have read this study and that in my opinion it conforms to acceptable standards of scholarly presentation and is fully adequate, in scope and quality, as a dissertation for the degree of Doctor of Philosophy.

Stephen T. Gottesman, Chair
Professor of Astronomy

I certify that I have read this study and that in my opinion it conforms to acceptable standards of scholarly presentation and is fully adequate, in scope and quality, as a dissertation for the degree of Doctor of Philosophy.

James H. Hunter, Jr.
James H. Hunter, Jr.
Professor of Astronomy

I certify that I have read this study and that in my opinion it conforms to acceptable standards of scholarly presentation and is fully adequate, in scope and quality, as a dissertation for the degree of Doctor of Philosophy.

James R. Ipser
Professor of Physics

I certify that I have read this study and that in my opinion it conforms to acceptable standards of scholarly presentation and is fully adequate, in scope and quality, as a dissertation for the degree of Doctor of Philosophy.

James W. Dufty
Professor of Physics

This dissertation was submitted to the Graduate Faculty of the College of Engineering and to the Graduate School and was accepted as partial fulfillment of the requirements for the degree of Doctor of Philosophy.

December 2003

Winfred M. Phillips
Dean, Graduate School

TITLE OF THE DISSERTATION

Veera Boonyasait
(352) 392-2052 x 210
Astronomy
Chair: Stephen T. Gottesman
Degree: Doctor of Philosophy
Graduation Date: December 2003

This dissertation is the culmination of analyzing observational data and combining the results with theoretical concepts. The object of research is the galaxy NGC 3359. The system is very much like our galaxy, the Milky Way. It has spiral arms and a bar structure in the middle of the galactic disk. Hence, any information that are obtained from studying NGC 3359 may be related to the Galaxy. Located approximately 36 million light years from the Sun, NGC 3359 is rich in neutral atomic hydrogen gas (H I). The H I disk is approximately 1.6×10^5 light years across—2 times the length of the disk seen by the eye. The galaxy also has many star formation regions that are detected by observing the ionized hydrogen (H II) gas. Most of these regions reside along the bar and spiral arms. Both H I and H II gases tend to flow circularly within the galactic disk, although large non-circular motions are conspicuous near the major structures of the galaxy. Through numerical simulations, it was found that the bar structure must be rotating at a faster speed than the spiral arms to produce models that reflect the actual galaxy. This very rare result makes NGC 3359 a very interesting galaxy to study.